
Structure and mechanical properties of metallic nanoglasses

Zur Erlangung des akademischen Grades Doktor-Ingenieur (Dr.-Ing.)
genehmigte Dissertation von MSc. Sree Harsha Nandam aus Hyderabad

Tag der Einreichung: 02.10.2018

Tag der Prüfung: 15.01.2019

Darmstadt 2019

1. Gutachten: Prof. Dr.-Ing. Horst Hahn
2. Gutachten: Prof. Dr.-Ing. Karsten Durst



TECHNISCHE
UNIVERSITÄT
DARMSTADT

Fachbereich Material- und
Geowissenschaften
Technische Universität Darmstadt

Institut für Nanotechnologie (INT)
Karlsruher Institut für Technologie (KIT)

Dieses Dokument wird bereitgestellt von tuprints,
E-Publishing Service der TU Darmstadt
<http://tuprints.ulb.tu-darmstadt.de>
tuprints@ulb.tu-darmstadt.de

Sree Harsha Nandam, Structure and mechanical properties of metallic nanoglasses
Darmstadt, Technische Universität Darmstadt,
Year thesis published in TUprints 2019
URN: <urn:nbn:de:tuda-tuprints-87026>
URL: <https://tuprints.ulb.tu-darmstadt.de/id/eprint/8702>
Published under
CC BY-NC-ND 4.0
International Attribution-Non Commercial - NoDerivatives 4.0 International
<https://creativecommons.org/licenses>

Erklärung zur Dissertation

Hiermit versichere ich, die vorliegende Dissertation ohne Hilfe Dritter nur mit den angegebenen Quellen und Hilfsmitteln angefertigt zu haben. Alle Stellen, die aus Quellen entnommen wurden, sind als solche kenntlich gemacht. Diese Arbeit hat in gleicher oder ähnlicher Form noch keiner Prüfungsbehörde vorgelegen.

Darmstadt, den

(Sree Harsha Nandam)



Abstract

Metallic nanoglasses are a new class of amorphous materials with interesting magnetic and mechanical properties. They are characterized by interfacial regions with enhanced free volume compared to the core of the nanoparticles. Till now, nanoglasses are primarily synthesized by using thermal evaporation in inert gas condensation (IGC). However, due to the different vapour pressure of constituent elements and reproducibility issues in thermal evaporation, it is difficult/impossible to synthesize different glassy compositions.

In this work, by using magnetron sputtering in IGC, $\text{Cu}_{50}\text{Zr}_{50}$, $\text{Cu}_{60}\text{Zr}_{40}$ and $\text{Pd}_{84}\text{Si}_{16}$ nanoglasses are produced with completely amorphous nature and good reproducibility. By varying several parameters, the yield of the sputtering process in IGC is optimized to make sufficient amount of material to obtain a nanoglass pellet. The influence of several processing parameters like inert gas pressure, sputtering power, the type of material etc., on the yield of the process are studied in the current work. The primary aim of the current work is to study the properties of the nanoglasses and compare them with conventional metallic glasses produced by melt-spinning and thus comment on the relation between the structure and properties of nanoglasses.

Structural characterization of the metallic nanoglasses showed that the samples are amorphous in nature. Elemental segregation in the samples was studied by atom probe tomography and significant segregation was found in Cu-Zr alloys while very little chemical inhomogeneity was observed in Pd-Si nanoglasses. Crystallization temperature was higher in Cu-Zr nanoglasses than that in melt-spun ribbons while Pd-Si nanoglasses showed lower glass transition and crystallization temperature compared to melt-spun ribbons. Mechanical properties of the nanoglasses and melt-spun ribbons were tested by indentation and micropillar compression tests. Hardness and elastic modulus were found to be higher in Cu-Zr and lower in Pd-Si nanoglasses compared to their corresponding melt-spun ribbons. Deformation mode was also found to be different in Cu-Zr and Pd-Si nanoglasses. While Cu-Zr nanoglasses deformed homogeneously without the formation of shear bands during indentation, Pd-Si alloys showed shear bands around the indents. Similar results were also observed in micropillar tests of Pd-Si and Cu-Zr nanoglasses. Cu-Zr nanoglasses showed less catastrophic deformation compared to the melt-spun ribbons while shear banding was observed in both Pd-Si nanoglasses and melt-spun ribbons. With the help of molecular dynamic simulations, the effect of topological structure at the interfacial regions was studied in Pd-Si metallic nanoglasses. Simulation results conveyed that the fraction of major Si polyhedra i.e. $\text{Si}[0,3,6,0]$ played an important role in determining the shear band formation and consequently the ductility of glassy Pd-Si alloys. With the increase in the fraction of $\text{Si}[0,3,6,0]$ in the interfacial regions of Pd-Si nanoglasses, the mode of deformation changed from homogenous to heterogeneous one. The importance of chemical inhomogeneity on the thermal and mechanical properties of nanoglasses was described in detail based on a segregation model.

Finally, $\text{Pd}_{80}\text{Si}_{20}$ thin film nanoglasses synthesized by conventional magnetron sputtering were also studied in the current work. No elemental segregation was observed in thin films. Annealing the nanoglassy thin films did not lead to any change in the globular nanostructure even after crystallization. The mode of deformation was practically the same as that in the rapidly quenched ribbon. The reasons for similar behaviour of the thin films and melt-spun ribbons are discussed.

Zusammenfassung

Metallische Nanogläser sind eine neue Klasse amorpher Materialien mit interessanten magnetischen und mechanischen Eigenschaften. Ihr charakteristisches Merkmal ist ein erhöhtes freies Volumen in den Zwischenräumen oder Grenzflächen zwischen den konstituierenden runden Partikeln, im Vergleich zum freien Volumen ihrer Kerne. Bis dato werden Nanogläser hauptsächlich mittels thermischer Verdampfung in einem Edelgas-Kondensations-Prozess (IGC, engl. inert gas condensation) hergestellt. Da die beteiligten Elemente unterschiedliche Dampfdrücke haben und thermische Verdampfungsprozesse daher schlecht reproduzierbar sind, ist es schwierig bis unmöglich, Gläser mit unterschiedlicher Zusammensetzung gezielt zu synthetisieren.

In dieser Arbeit wurden vollständig amorphe Nanogläser aus $\text{Cu}_{50}\text{Zr}_{50}$, $\text{Cu}_{60}\text{Zr}_{40}$ und $\text{Pd}_{84}\text{Si}_{16}$ mittels Magnetron-Sputtern-IGC-Prozess unter dem Aspekt guter Reproduzierbarkeit hergestellt. Die Prozessparameter wurden derart variiert, bis die Ausbeute durch den Prozess groß genug war um eine Tablette aus dem synthetisierten Material herzustellen. So wurde der Einfluss von Edelgasdruck, Sputterleistung, Materialzusammensetzung, etc. auf die Syntheserate in der vorliegenden Arbeit untersucht. Die Untersuchung der Eigenschaften der hergestellten Nanogläser, deren Vergleich mit herkömmlichen metallischen Gläsern, welche nach dem Schmelzspinnverfahren hergestellt wurden, und somit der Zusammenhang zwischen Struktur und Eigenschaften der Nanogläser bilden den Schwerpunkt dieser Arbeit.

Eine Strukturanalyse der metallischen Nanogläser ergab, dass die hergestellten Proben eine amorphe Struktur besitzen. Die Ausscheidung einzelner Elemente wurde mittels Atomsonden-Tomographie untersucht. In bedeutender Menge wurden solche Ausscheidungen nur in Cu-Zr-Legierungen gefunden, während nur eine geringe chemische Inhomogenität in Pd-Si-Nanogläsern festgestellt wurde. Die Kristallisationstemperatur lag für Cu-Zr-Nanogläser über der von mittels Schmelzspinn-Verfahren hergestellten Proben, während für das Pd-Si-System Glasübergangs- und Kristallisationstemperatur der Nanogläser jeweils unter der der Proben aus dem Schmelzspinn-Verfahren lagen. Die mechanischen Eigenschaften von Nanogläsern und schmelzgesponnenen Filmen wurde in Härteprüfungsuntersuchungen und mit Hilfe von Mikrosäulendruckversuchen bestimmt. Härte und Elastizitätsmodul waren in Cu-Zr-Nanogläsern und in Pd-Si-Nanogläsern erhöht im Vergleich zu den entsprechenden schmelzgesponnenen Bändern. Die Deformationsmechanismen von Cu-Zr- und Pd-Si-Nanogläsern unterschieden sich ebenfalls. Während sich Cu-Zr-Nanogläser im Härteprüftest homogen verformten und sich keine Scherbänder bildeten, traten bei Pd-Si-Nanogläsern Scherbänder um die Eindruckstelle auf. Ein ähnliches Ergebnis wurde auch in den Mikrosäulendruckversuchen festgestellt.

Cu-Zr-Nanogläser zeigen im Vergleich zu schmelzgesponnenen Bändern eine weniger katastrophale Verformung, während Scherbandbildung sowohl bei Pd-Si-Nanogläsern als auch bei den schmelzgesponnenen Bändern gefunden wurden.

Topologieeffekte in den Zwischenräumen der Nanoglaspartikeloberflächen wurden für metallische Pd-Si-Nanogläser mithilfe molekuldynamischer Simulationen untersucht. Die Simulationen ergaben, dass der Anteil, insbesondere der Si[0,3,6,0] Polyeder, eine wichtige Rolle bei der Bildung von Scherbändern spielt und sich damit auch auf die Duktilität von glasartigen Pd-Si-Legierungen auswirkt. Mit steigendem Si[0,3,6,0]-Anteil in den Grenzflächen der Pd-Si-Nanogläser änderte sich der Deformationsmechanismus von homogener zu heterogener Verformung. Der Einfluss der chemischen Inhomogenität auf die thermischen und mechanischen Eigenschaften von Nanogläsern wird anhand eines Auscheidungsmodells detailliert erklärt. Ebenso wurden in dieser Arbeit auch Pd₈₀Si₂₀-Dünnschichten, die mittels konventionellem Magnetron-Sputtern hergestellt wurden, untersucht. In Dünnschichten konnten aber keine Ausscheidungen festgestellt werden. Eine Temperaturbehandlung der dünnen Nanoglasfilme führte zu keiner Veränderung der Nanostruktur, selbst nach der Kristallisation der Filme. Der Deformationsmechanismus war gewissermaßen derselbe wie bei den schnell abgeschreckten Bändern. Die möglichen Gründe dafür werden ebenfalls diskutiert.

Table of contents

Abstract.....	iii
Zusammenfassung.....	iv
Table of contents	vi
List of figures.....	viii
List of tables.....	xi
Definition of abbreviations and symbols.....	xii
1. Introduction.....	1
1.1 Motivation	1
1.2 Objective, Scope and Outline of thesis	2
2. Scientific background.....	5
2.1 Metallic glasses	5
2.2 Thermodynamics and kinetics of metallic glasses	7
2.3 Structure of metallic glasses.....	9
2.4 Deformation behaviour in metallic glasses	12
2.5 Metallic nanoglasses	16
2.6 Deformation of metallic nanoglasses	18
3. Materials and Methods.....	20
3.1 Synthesis Techniques	20
3.1.1 Inert gas condensation (IGC)	20
3.1.2 Magnetron sputtering	22
3.1.2 Melt spinning	23
3.2 Characterization techniques	23
3.2.1 X-ray diffraction	23
3.2.2 Scanning electron microscopy	23
3.2.3 Transmission electron microscopy.....	24
3.2.4 Atom probe tomography	24
3.2.5 Differential Scanning Calorimetry	25
3.2.6 Density measurements	26
3.2.7 Focused Ion Beam Milling.....	27
3.2.8 Oxygen analysis	28
3.3 Mechanical testing.....	28
3.3.1 Indentation measurements.....	28
3.3.2 Microcompression testing	31
3.4 MD simulations	33
3.5 Materials.....	34
4. Optimization of process variables in inert gas condensation.....	36
4.1 Influence of gas pressure.....	36
4.2 Influence of sputtering power.....	37
4.3 Influence of gas flow.....	37
4.4 Influence of type of inert gas and He/Ar ratio.....	37
4.5 Influence of alloy materials.....	38

5. Atomic structure and properties of Cu-Zr nanoglasses synthesized by IGC.....	40
5.1 Experimental details	40
5.2 Structural characterization of nanoglasses	41
5.3 Thermal stability	46
5.4 Micro- and Nanoindentation	50
5.5 Volume of STZ.....	52
5.6 Microcompression testing	54
5.7 Studies on Cu ₆₀ Zr ₄₀ nanoglasses.....	54
5.8 Discussion on the structure of nanoglass	57
5.9 Thermal behaviour and its relation to the structure of nanoglass.....	59
5.8.1 Increase in T _g and T _x	59
5.8.2 Enthalpy of crystallization reaction	59
5.8.3 Young's modulus, plasticity, STZ volume and its relation to the structure	60
5.10 Summary	61
6. Effect of topological structure on mechanical properties of Pd-Si nanoglasses synthesized by IGC	62
6.1 Experimental details.....	62
6.2 Simulation details	63
6.3 Structural characterization.....	63
6.4 Indentation tests.....	69
6.5 Microcompression tests	71
6.6 Comparison with MD simulations	72
6.7 Summary	77
7. Mechanical properties and crystallization of Pd-Si nanoglass films synthesized by magnetron sputtering	78
7.1 Structural characterization of thin films	78
7.2 Thermal stability of thin film nanoglasses	80
7.3 Mechanical behaviour of sputtered nanoglasses	82
7.4 Summary	84
8. Conclusions and Outlook	86
8.1 Conclusions	86
8.2 Outlook.....	87
References.....	90
Curriculum Vitae	101
List of Publications	102
Acknowledgements	104

List of figures

Fig. 2.1 Metallic glasses made from Vitalloy (Zr based glass) from (Reprinted with permission from [14])	7
Fig. 2.2 Rapid cooling the liquid melt forms a solid glass. The glass transition temperature increases with increasing cooling rate	8
Fig. 2.3 (a) Schematic showing the principle of Angstrom beam electron diffraction, (b) Calculated 3-D profile of 0.36 nm electron beam (c) Electron diffraction patterns obtained by increasing the diameter of the beam. It can be clearly observed that by decreasing the size of the electron beam, diffraction patterns, which resemble those of crystalline regions can be obtained. (Reprinted with permission from Hirata <i>et al.</i> [67])	11
Fig. 2.4 (a) Schematic of a STZ after Argon and Kuo [62], (b) Schematic of a typical compressive stress-strain curve of a ductile and brittle metallic glass. Arrows indicate elastic and plastic deformation regions (c) Homogeneous deformation in Pd ₄₀ Ni ₄₀ P ₂₀ metallic glass [73] and (d) Shear band in a Zr-based metallic glass [74] (Figures (c) and (d) are reprinted with permission from their respective publishers)	15
Fig. 2.5 Schematic of (a) consolidation of amorphous nanoparticles and (b) metallic nanoglass.	16
Fig. 2.6 (a) Compressive stress strain curves of a nanoglass and metallic glass with a diameter of 300 nm, tested micropillar of (b) nanoglass and (c) metallic glass. Reprinted with permission from ref.[34].	18
Fig. 3.1 (a) Inert gas condensation set-up used to synthesize the nanoparticles, (b) Top view of the inside of the chamber showing the sputter gun and (c) Schematic showing the IGC process	21
Fig. 3.2 (a) Schematic explaining the principle of magnetron sputtering, (b) Magnetron sputtering unit used to deposit thin films	22
Fig. 3.3 (a) Cu ₅₀ Zr ₅₀ APT tip prepared by FIB, (b) Reconstructed tip with Cu atoms in red and Zr in blue.....	25
Fig. 3.4 Plot of mass vs. volume of a Cu ₅₀ Zr ₅₀ nanoglass sample. The slope gives the density of the material in g/cm ³	27
Fig. 3.5 Micropillars of (a) Pd ₈₀ Si ₂₀ nanoglass (b) HPT-processed Pd ₈₀ Si ₂₀ nanoglass	28
Fig. 3.6 A Vicker's indent of a Cu ₅₀ Zr ₅₀ sample. The average of diagonals d ₁ and d ₂ is used to calculate the area of the indent.....	29
Fig. 3.7 Load-displacement curve for a HPT-processed Pd ₈₄ Si ₁₆ nanoglass. S is the stiffness of the contact calculated from the slope of the unloading portion	30
Fig. 3.8 The atomic configurations of the 36 nm diameter metallic glass and nanoglass pillars used in the simulations: (a) Metallic glass and (b) Nanoglass. Glassy grains and interfaces are shown in different colors to highlight the microstructure of nanoglass. All pillars have an aspect ratio of 2.	34
Fig. 4.1 (a) Ni ₅₀ Ti ₄₅ Cu ₅ and (b) Cu targets after sputtering. Re-deposited zones are indicated by arrows	37

Fig. 5.1 XRD of the $\text{Cu}_{50}\text{Zr}_{50}$ and $\text{Cu}_{60}\text{Zr}_{40}$ melt-spun ribbons and nanoglass samples. XRD patterns of $\text{Cu}_{50}\text{Zr}_{50}$ annealed nanoglass samples are also shown.	41
Fig. 5.2 TEM images of (a) $\text{Cu}_{50}\text{Zr}_{50}$ amorphous powder scraped from the cold finger, inset showing the SAED confirming the amorphous nature of the sample (b) bright-field image of nanoglass showing amorphous nature, which was confirmed by the diffraction pattern (inset). (c) HRTEM image of the nanoglass showing the amorphous contrast with no crystalline patterns	42
Fig. 5.3 (a) Secondary electron image of a $\text{Cu}_{50}\text{Zr}_{50}$ nanoglass and (b) EDS spectrum taken from the fig. (a). Composition of the sample obtained from the EDS spectrum is also mentioned in the fig. (b)	43
Fig. 5.4 (a) 3DAP tomography image of a tip prepared from a nanoglass sample (Zr atoms in blue and Cu atoms in red) (b) Heat map of Zr showing the segregation of Zr in the range of 5-6 nm (c) Heat map of Zr at a magnified scale (d) Composition map of Cu and Zr along the arrow shown in the (c), (e) Proxigram on a 65 at.% Zr iso-surface showing the compositional variation and (f) composition profile along a cylinder of 3DAP in $\text{Cu}_{50}\text{Zr}_{50}$ melt-spun ribbon	44
Fig. 5.5 DSC of $\text{Cu}_{50}\text{Zr}_{50}$ melt-spun ribbon, nanoglass and the annealed nanoglass for different times showing the glass transition and crystallization temperature. Crystallization temperature of the nanoglass is higher than that of the melt-spun ribbon. Curves are shifted along the Y-axis (heat flow) for clarity. Arrow indicates T_g of melt-spun ribbons.....	47
Fig. 5.6 (a) XRD of completely crystallized nanoglass and melt-spun ribbon sample, (b) TEM of nanoglass sample heated upto 460 °C in a DSC. Fine crystals in the size range of 5-10 nm can be seen. (c) SAED pattern of the region showing faint crystalline rings.....	48
Fig. 5.7 DSC plots showing the crystallization reaction at four heating rates in $\text{Cu}_{50}\text{Zr}_{50}$ (a) melt-spun ribbon, (b) nanoglass and (c) Activation energy plot using Kissinger equation	49
Fig. 5.8 Scanning electron micrographs of indents in (a) $\text{Cu}_{50}\text{Zr}_{50}$ as-prepared nanoglass, (b) $\text{Cu}_{50}\text{Zr}_{50}$ annealed nanoglass, neither of them showing shear bands around the indent (c) $\text{Cu}_{50}\text{Zr}_{50}$ melt-spun ribbon with clear shear bands around the indent, (d) STEM image showing no crystallization below the indent. Pt deposited during FIB is the dark region on the right hand side of the image. The line indicates the partition between Pt and the nanoglass and (e) HRTEM of the nanoglass region confirming the amorphous nature.	51
Fig. 5.9 Representative nano indentation curves of melt-spun ribbon, as-prepared nanoglass and annealed nanoglass at an indentation strain rate of 0.05 s^{-1} . No pop-ins were observed in the nanoglass samples while they were observed in melt-spun ribbons (indicated by arrows).....	52
Fig. 5.10 Nanoindentation curves of (a) nanoglass and (b) melt-spun ribbons at three different strain rates. For better clarity, the starting points of the curves were shifted by 50 nm (c) log-log plots of hardness and strain rate for nanoglass and melt-spun ribbons.....	53
Fig. 5.11 Engineering stress-strain curves of Cu-Zr nanoglass and melt-spun ribbons at a displacement rate of (a) 10 nms^{-1} , (b) 20 nms^{-1} , corresponding deformed pillar images of (c) nanoglass at 10 nms^{-1} , (d) melt-spun ribbon at 10 nms^{-1} , (e) nanoglass at 20 nms^{-1} and (f) melt-spun ribbon at 20 nms^{-1}	54
Fig. 5.12 (a) XRD of $\text{Cu}_{60}\text{Zr}_{40}$ melt-spun ribbons, nanoglass and annealed nanoglass, (b) Secondary electron image in SEM, (c) EDS spectrum obtained from the fig. (b). Composition obtained from the spectrum is also given in the figure.....	55
Fig. 5.13 (a) APT profile of $\text{Cu}_{60}\text{Zr}_{40}$ nanoglass and (b) composition profile along a cylinder in APT tomograph showing the composition segregation. Compositional fluctuation is much more in $\text{Cu}_{60}\text{Zr}_{40}$ compared to $\text{Cu}_{50}\text{Zr}_{50}$ nanoglass alloy.....	56
Fig. 5.14 DSC of $\text{Cu}_{60}\text{Zr}_{40}$ melt-spun ribbons and nanoglass samples. A shoulder is observed in the nanoglass sample which is marked by arrow in the figure.	56
Fig. 5.15 Vickers indent of a $\text{Cu}_{60}\text{Zr}_{40}$ nanoglass under a load of 1000 gf	57

Fig. 5.16 Schematic indicating (a) segregated amorphous nanoparticle; (b) Compaction of amorphous nanoparticles and (c) nanoglass with segregated interfaces.....	58
Fig. 6.1 (a) XRD showing the amorphous nature of all the samples, (b) TEM image of Pd-Si particles (c) SE image of Pd-Si nanoglass and (d) EDS spectrum obtained from the red rectangle in (c). The composition of the spectrum is shown in the figure.	64
Fig. 6.2 (a) APT tip of the nanoglass showing the Pd and Si atoms (Pd is denoted by purple and Si is denoted by cyan), (b) average composition profile along a cylinder shown in (a), indicating Pd, Si and O atomic percentages, (c) proxigram showing the average composition profile across a 15% Si iso-surface in a nanoglass and (d) average composition map along a cylinder in (a) from Pd-Si melt-spun ribbons	65
Fig. 6.3 (a) DSC showing the T_g , T_x of the nanoglass, HPT-processed nanoglass and melt-spun ribbons, black arrow in the figure indicates second crystallization step, (b) magnified image of the glass transition regions in all the three samples. Black arrows indicate glass transition while the red arrow indicates the exothermic peaks in HPT-processed nanoglass around glass transition	67
Fig. 6.4 DSC at different heating rates of (a) melt-spun ribbons, (b) HPT-processed nanoglass and (c) activation energy plots based on Kissinger equation of the nanoglass and melt-spun ribbon and (d) Energy diagram for the nanoglass and conventional metallic glass. Predominantly nanoglasses show higher activation energy and lower enthalpy than the conventional melt-spun ribbons.....	68
Fig. 6.5 Load-displacement curves of all the samples obtained using nanoindentation	70
Fig. 6.6 Engineering stress-strain curves obtained from micropillar tests	71
Fig. 6.7 SEM images of tested micropillars at two different displacement rates. Pd ₈₀ Si ₂₀ melt-spun ribbon at (a) 10 nms ⁻¹ , (b) 20 nms ⁻¹ , Pd ₈₄ Si ₁₆ nanoglass at (c) 10 nms ⁻¹ , (d) 20 nms ⁻¹ and Pd ₈₄ Si ₁₆ HPT-processed nanoglass at (e) 10 nms ⁻¹ , (f) 20 nms ⁻¹	72
Fig. 6.8 Molecular dynamics results of the annealing of a Pd ₈₀ Si ₂₀ nanoglass at a temperature of about 600 K ($\approx 0.8T_g$). (a) Variation of the most prominent Voronoi polyhedra, Si[0,3,6,0]. (b) Number density. Bulk glass with the same chemical composition as the nanoglass is added for comparison.....	73
Fig. 6.9 Mechanical response of as-prepared and annealed Pd ₈₀ Si ₂₀ metallic glass and nanoglass pillars obtained by molecular dynamics simulations. (a) Engineering stress-strain curves and (b) the degree of strain localization parameter, Ψ , during uniaxial compressive deformation	74
Fig. 6.10 Local atomic von Mises shear strain at 20% total compression strain for the as-prepared and annealed Pd ₈₀ Si ₂₀ metallic glass and nanoglass pillars for different times (a) & (e) as-prepared, (b) & (f) annealed for 30 ns, (c) & (g)	76
Fig. 7.1 (a) XRD of (top) 60 W Pd + 60 W Si sputtered thin film (middle) 30 W Pd + 60 W Si sputtered thin film and (bottom) Si substrate, (b) SEM image of the top surface of the thin film and (c) cross-section of the thin film showing columnar morphology.....	79
Fig. 7.2 (a) TEM image of thin film white regions are gaps between the island regions (b) HRTEM image confirming the amorphous nature and inset showing the diffraction pattern, (c) TEM image where the elemental maps were obtained, (d) Pd map and (e) Si map showing uniform distribution with no obvious elemental segregation.	80
Fig. 7.3 (a) XRD of as-sputtered film and the annealed samples at 200, 300 and 400 °C at 2 and 24 h and (b) XRD of melt-spun ribbons annealed at different temperatures	81
Fig. 7.4 SEM images of (a) as sputtered thin film, annealed thin film at (b) 200 °C for 2 h, (c) 300°C for 2 h, (d) 400 °C for 2 h and (e) 300 °C for 24 h	82

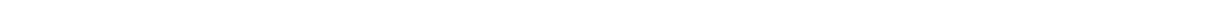
Fig. 7.5 (a) Nanoindentation load-displacement curves at different indentation strain rates for a depth of 50 nm, SEM images of nanoindent at an (b) indentation strain rate of 0.05 s^{-1} for a depth of 50 nm and (c) indentation strain rate of 0.05 s^{-1} for a depth of 800 nm.....	83
Fig. 7.6 (a) Load-displacement curve of Pd-Si sputtered nanoglass and melt-spun ribbon and (b) SEM image of a compressed micropillar showing shear bands	84

List of tables

Table 4.1 Effect of the process parameters on the yield of the powder	38
Table 4.2 Alloy targets and the final composition of powder	39
Table 5.1 Glass transition (T_g), onset of crystallization (T_x) and peak (T_p) temperature, Hardness by Vickers and nanoindentation (strain rate of 0.05 s^{-1}), Young's modulus of as-prepared nanoglass, annealed nanoglass and melt-spun ribbons	45
Table 6. 1 Onset of crystallization, hardness and modulus obtained by nanoindentation of all samples	67

Definition of abbreviations and symbols

3DAP	3-Dimensional Atom Probe
APT	Atom probe tomography
BMG	Bulk Metallic Glass
CSM	Continuous Stiffness Measurement
DC	Direct Current
DSC	Differential Scanning Calorimetry
EDS	Energy Dispersive Spectroscopy
EXAFS	Extended X-ray Absorption Fine Structure
FCC	Face Centred Cubic
FIB	Focused Ion Beam
HCP	Hexagonal Close Packing
HPT	High Pressure Torsion
HRTEM	High Resolution Transmission Electron Microscopy
IAM	Institut für Angewandte Materialien
IFW	Institut für Festkörper- und Werkstoffforschung
IGC	Inert Gas Condensation
INT	Institute for Nanotechnology
KIT	Karlsruhe Institute of Technology
LAMMPS	Large-scale Atomic/Molecular Massively Parallel Simulator
MEMS	Micro Electro-Mechanical Systems
MD	Molecular Dynamics
OVITO	Open Visualization Tool
SI	Supporting Information
SRO	Short Range Order
MRO	Medium Range Order
PAS	Positron Annihilation Spectroscopy
SEM	Scanning Electron Microscopy
STZ	Shear Transformation Zone
TU	Technischen Universität
UHV	Ultra-High Vacuum
XRD	X-ray Diffraction
ρ	Density
E	Young's Modulus
μ	Shear Modulus
B	Bulk Modulus
T_g	Glass transition temperature
T_x	Onset of crystallization temperature
ΔH_x	Enthalpy of crystallization
η	Von-Mises strain
ψ	Strain localization parameter
k	Boltzmann constant
V	Volume
w	Weight
θ	Bragg angle



1. Introduction

1.1 Motivation

Metallic glasses are amorphous materials, which were discovered in 1960 by Klement and Duwez [1]. Since their discovery, a great amount of scientific literature has been published on metallic glasses regarding their glass forming ability, atomic structure and properties [2–14]. Metallic glasses are typically produced by rapid quenching techniques like splat quenching [1], melt-spinning [15], suction casting [16–18] etc. Although several applications are attempted with metallic glasses [19,20], lack of ductility, poor fatigue tolerance and also complexity in synthesis due to the required high cooling rates for the production, severely restricts them in making large scale impact in the materials community.

With respect to the mechanical properties, one of the most important disadvantages of metallic glasses is their lack of ductility, which leads to catastrophic failure during loading. Several strategies have already been explored in the area of metallic glasses to improve their ductility. Bulk metallic glass composites [21], severe plastic deformation of metallic glasses [22,23], composition specific metallic glasses [24], phase separated metallic glasses [25] are some of the strategies, which are successfully implemented to improve the plasticity in metallic glasses. The fundamental idea in all the above strategies is to introduce secondary phases or introduce shear band like defects in metallic glasses and thus improve their ductility. One such new and interesting strategy is the concept of metallic nanoglasses where sites with enhanced free volume are introduced in the order of a few nanometers.

The structure of nanoglasses is analogous to that of nanocrystalline materials, exhibiting interfacial regions of 1-2 nanometers, characterized by a lower density (high free volume) compared to the core of the nanoparticles [26–28]. The primary synthesis techniques to produce nanoglasses are IGC and conventional magnetron sputtering. In IGC, the synthesis involves production of amorphous nanoparticles, which are subsequently compacted to make nanoglasses. Some of the nanoglasses, which are successfully synthesized by using thermal evaporation in IGC are Pd-Fe-Si [28], $\text{Sc}_{75}\text{Fe}_{25}$ [29] and $\text{Fe}_{90}\text{Sc}_{10}$ [30]. An alternative synthesis route is the conventional magnetron sputtering, which is employed to produce thin films with a nano-grained amorphous structure, termed as “nanoglasses” in literature. $\text{Au}_{52}\text{Ag}_5\text{Pd}_2\text{Cu}_{25}\text{Si}_{10}\text{Al}_6$ [31] and $\text{Ni}_{50}\text{Ti}_{45}\text{Cu}_5$ [32] nanoglass thin films are deposited by using this technique. Enhanced ductility is reported in $\text{Sc}_{75}\text{Fe}_{25}$ nanoglass compared to the melt-spun ribbons of the same composition [33,34]. Since there is a large volume fraction of the interfacial regions, i.e. almost 30 % in nanoglasses, it is possible to accommodate bulk strain into the interfacial regions during mechanical deformation. There is also no clear trend in the hardness and elastic modulus values of nanoglasses when compared to the corresponding melt-spun ribbons. Higher hardness and modulus values are reported for $\text{Sc}_{75}\text{Fe}_{25}$ nanoglasses

while lower values are reported for Fe₉₀Sc₁₀ nanoglasses compared to their respective melt-spun ribbons [35]. Au-based nanoglass thin films synthesized by magnetron sputtering showed high hardness values compared to the corresponding bulk metallic glass composition [31]. Moreover, the thermal stability is very poorly understood in metallic nanoglasses. T_g and T_x are observed to be higher in Au-based nanoglass thin films [36] while no systematic study is reported on the nanoglasses synthesized by IGC.

Despite the number of publications on mechanical properties of nanoglasses, the physical understanding of the deformation mechanism is still very limited because of the small size of the interfacial regions. It is still not clear whether the chemical or structural (or both) disorder at the interfaces is the reason for the observed changes in the nanoglass properties. Recent MD simulations by Adjaoud *et al.* [37] predicted segregation of Cu and Pd to the surfaces of Cu₆₄Zr₃₆ and Pd₈₀Si₂₀ amorphous nanoparticles respectively. Wang *et al.* [38] showed segregation of Fe to the surface of Fe₉₀Sc₁₀ nanoparticles by using high resolution analytical TEM. Although there are a number of simulation and experimental studies on nanoglasses, a direct comparison is difficult to make since the simulations are primarily carried out on Cu-Zr and Ge nanoglasses [39–42], while the experiments are performed on Fe-Sc nanoglasses [30,33,34,43]. In this regard, it is better if one can perform experiments and simulations on the same alloy to gain a clear understanding of the structure and properties of nanoglasses.

1.2 Objective, Scope and Outline of thesis

Objective:

The primary objective of this work is to study structural features (like chemical segregation) and deformation behaviour of Cu-Zr and Pd-Si nanoglasses and compare them with conventional melt-spun metallic glasses of a similar composition. By combining experiments and MD simulations, the correlation between structure of the metallic nanoglasses and their properties will be studied in detail.

Scope:

Cu-Zr and Pd-Si nanoglasses were synthesized by IGC technique using magnetron sputtering and their amorphous nature was studied by x-ray diffraction and HRTEM. Compositional segregation in Cu-Zr and Pd-Si nanoglasses was determined by atom probe tomography. Differential scanning calorimetry was performed on both the nanoglasses and melt-spun ribbons to observe for any change in glass transition and crystallization temperatures. Deformation behaviour of melt-spun ribbons and nanoglasses is studied by using indentation and micropillar tests. MD simulations are used in Pd-Si glassy alloys to study the effect of topological structure in nanoglasses and metallic glasses. The possible reason for the observed properties and its correlation to the structure is explained based on a segregation

model. Finally, Pd-Si thin film nanoglasses were also studied for their deformation behavior and the results were compared with the conventional metallic glasses.

Outline of thesis:

Chapter 2 gives an overview of the basics of metallic glasses, nanoglasses and the effect of atomic structure on their deformation behaviour. Current unsolved problems in the deformation behaviour of nanoglasses are highlighted in this section.

Chapter 3 deals with the synthesis of nanoglasses, experimental details about the characterization and mechanical testing methods. In this chapter, the advantages of magnetron sputtering compared to thermal evaporation in IGC are also explained.

Chapter 4 describes the experimental parameters that need to be optimized in IGC and the effect of these parameters on the yield and quality of the material.

Chapter 5 primarily explains the experimental results obtained on the $\text{Cu}_{50}\text{Zr}_{50}$ alloys along with some results obtained from $\text{Cu}_{60}\text{Zr}_{40}$ nanoglasses. In particular, the elemental segregation and deformation behaviour of $\text{Cu}_{50}\text{Zr}_{50}$ are described in this section. In order to explain the effect of elemental segregation on the thermal and deformation behavior, a model is proposed.

Chapter 6 presents the deformation behaviour of Pd-Si nanoglasses where the effect of chemical inhomogeneity is not as significant as for Cu-Zr nanoglasses. By using MD simulations, the effect of topological structure at the interfacial regions on the deformation behaviour is described in detail in this section.

Chapter 7 details about the structure and deformation behaviour in Pd-Si thin film nanoglasses. The similarity in the deformation behaviour of Pd-Si melt-spun ribbons and sputtered films are described here.

Finally, conclusions based on the present work and the prospective research areas in this field will be highlighted in Chapter 8.



2. Scientific background

In this chapter, an introduction to metallic glasses, their atomic structure, the deformation behavior and the influence of atomic structure on deformation behavior will be discussed. The advantages of metallic nanoglasses and the unsolved puzzles in the nanoglass literature will also be described in detail.

2.1 Metallic glasses

Rapid quenching of liquid alloy melts to room temperature leads to the formation of metallic glasses. The first metallic glass was discovered in 1960 by Klement *et al.* [1] when a Au-Si alloy was successfully quenched to an amorphous phase using “splat quenching” technique. Since then, several other glass forming compositions were discovered by using various techniques like melt-spinning, suction casting, splat quenching, magnetron sputtering etc. [16,17,44,45]. The requirement of high cooling rates in the order of $10^5 - 10^6$ K/s acted as a major obstacle to synthesize metallic glasses in bulk form and as a consequence, metallic glasses could only be obtained as ribbons or flakes [46]. So, the major aim of metallic glass research in the early stages was to find glass forming compositions, which can be obtained at low critical cooling rates so that glasses with large critical diameter, so-called bulk metallic glasses (BMGs), can be manufactured. BMGs are defined as glasses, which have a diameter greater than 1 mm. In the early stages of BMG research, compositions based on noble metal based systems like Pd-Ni-P and Pd-Cu-Si were discovered by few groups [47,48]. The cooling rate required for the formation of an amorphous phase in such systems is around 10 K s^{-1} , and BMGs were successfully synthesized to a thickness of about 10 mm. Peker and Johnson [49] successfully synthesized a Zr-based glass with a composition $Zr_{41.2}Ti_{13.8}Cu_{12.5}Ni_{10}Be_{22.5}$, of about 14 mm in diameter, which has excellent glass forming ability. The critical cooling rate for this alloy is less than 10 K/s. Because of the high costs of the raw materials and the limited number of glass forming compositions, progress in BMG research was slow. This situation changed when Inoue and co-workers found that BMG formation is favoured by mixing more than three constituent elements.

Based on the existing BMG compositions till then, Inoue proposed the following empirical rules for improved glass forming ability [2,3]:

1. Compositions must contain more than three elements
2. Atomic size difference between the three main elements must be about 12 %.
3. Heats of mixing between the three main constituent elements must be negative.

Following these empirical rules, several glass forming compositions were synthesized till today. Inoue *et al.* [50] were successful in synthesizing glassy metallic rods with a diameter

of 72 mm in a Pd based system. The reason for such a high glass forming ability in multi component alloys is thought to be the increase in the degree of dense random packing of atoms (both topological and chemical). Because of many constituent elements, there is an increase in the viscosity of the liquid melt, which makes it difficult for atomic rearrangement during solidification and also decreases the possibility of nucleation of crystalline phases, which requires long range diffusion [14]. The reasons for high glass forming ability of such multi component systems will be discussed in detail in section 2.2.

Due to their lack of periodic structure, metallic glasses have several interesting properties. Generally, metallic glasses have lower density, low elastic modulus, high elastic limit and high strength compared to their crystalline counterparts [13]. Their lack of crystalline structure roughly translates to high interatomic spacing between atoms leading to reduced bond strength and subsequently low elastic modulus. Unlike in crystalline materials, metallic glasses have no defects like dislocations, grain boundaries etc., giving them their high strengths almost approaching theoretical limit [13]. Their high strength and elastic limit in combination with low elastic modulus makes them excellent candidates for applications like golf clubs, tennis racquets etc. [19]. High hardness of metallic glasses also makes them good materials for wear resistance applications. Some of the Fe- and Co- based metallic glasses have very good soft magnetic properties [8], which found applications in magnetic transformer cores and magnetic shields. There were also successful efforts to use them in MEMS devices [19,46,51] and pressure sensors [52]. Another promising feature of metallic glasses is the absence of volume shrinkage at the glass transition temperature (T_g), which is a very attractive prospect in making near net shaped parts like gears as shown in fig. 2.1. The absence of volume shrinkage will be discussed in the subsequent section 2.2.

Although several applications were attempted till now, there are still some practical limitations for full fledged use of metallic glasses in everyday life. As mentioned earlier in the introduction, one of the major limitations is their brittleness, which makes them suffer catastrophic failure during mechanical loading. So, improving the plasticity has been one of the major research areas in metallic glasses for a long time. In this regard, a new class of amorphous materials called metallic nanoglasses was found to have improved plasticity compared to conventional metallic glasses. The main focus of the present work will be to unravel the atomic structure in such metallic nanoglasses and the reason for the increase in their plasticity.

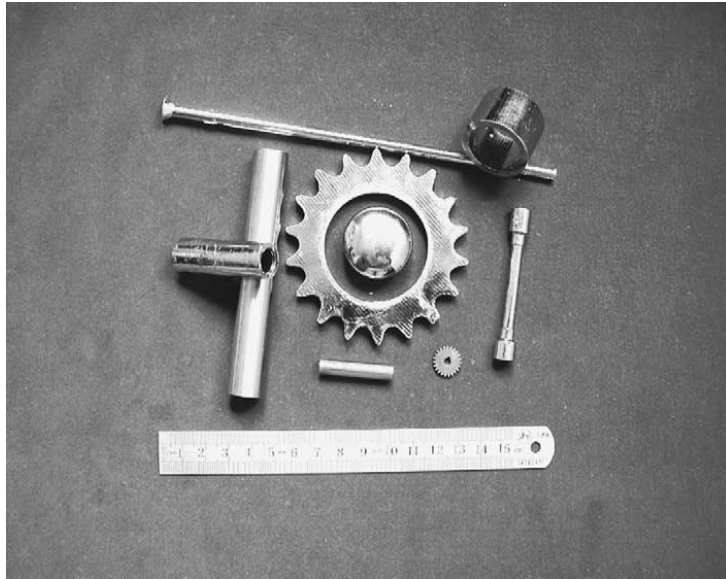


Fig. 2.1 Metallic glasses made from Vitallloy (Zr based glass) from (Reprinted with permission from [14])

2.2 Thermodynamics and kinetics of metallic glasses

Understanding the basics of glass formation is essential to know the different kinds of metastable states that can form in a metallic glass and also to predict the glass forming ability. When a liquid is cooled at a certain cooling rate below the melting point as shown in fig. 2.2, it becomes a glass at a temperature, which is called the glass transition temperature (T_g). This temperature depends on the cooling rate employed during the formation of metallic glass. As shown in fig. 2.2, T_g decreases with a decrease in cooling rate. Kauzmann was one of the first to explain the phenomenon of glass transition [53]. When the entropy of a liquid is extrapolated to low temperatures below the melting point, at a certain temperature, the entropy of the liquid becomes equal to the entropy of the solid, which is physically impossible. So, the liquid can no longer remain in such a metastable state and it freezes to form a glass at that temperature and such a temperature would be the ideal glass transition temperature, also known as Kauzmann temperature (T_k). However, in practical circumstances, crystallization initiates in the liquid before one can reach the ideal T_g which makes it nearly impossible to reach the ideal glass transition temperature. The phenomenon of glass transition has important consequences in applications. Since there is no change in volume at the glass transition temperature as shown in fig. 2.2, which means there is no volume shrinkage during solidification, near net shape forming is possible in metallic glasses (see fig. 2.1). Another important feature to observe in fig. 2.2 is that the final glassy state depends on the cooling rate. The slower the cooling rate during solidification, the more stable glass can be obtained. Having said that, cooling the liquid slowly implies there is a higher chance of crystallization to happen during the solidification because of the large driving force for crystal nucleation in undercooled melts. So, a liquid melt, which is stable against crystallization, can be undercooled at a slow cooling rate. So, in practice freezing the liquid at

ideal T_g or Kauzmann temperature is quite difficult. But recent reports have claimed that such ultra-stable glasses are possible in organic and metallic glasses by keeping the substrate temperature close to T_g during magnetron sputtering of thin films [54–56].

After discussing the various metastable states that can be formed in a glass, the next step is to find a criterion to predict the compositions, which can be quenched to a glass. We will discuss briefly on one of the first criterion proposed by Turnbull to predict the glass forming ability in an alloy. Turnbull proposed the concept of reduced glass transition temperature (T_{rg}), which is defined as $T_{rg} = T_g/T_m$, [57]. He pointed out that deep eutectic compositions can be good glass formers in a given system. It was proposed that homogeneous nucleation of crystal phases can be avoided if T_{rg} is about 0.67, then liquid metal can be quenched to a glass more easily [14,57]. Although several other criteria were proposed later on, Turnbull's criterion remains one of the best rules for finding glass formers in binary metallic systems. $Fe_{80}B_{20}$, $Pd_{80}Si_{20}$ etc., were some of the glass forming compositions, which was found at near eutectic compositions based on this criterion.

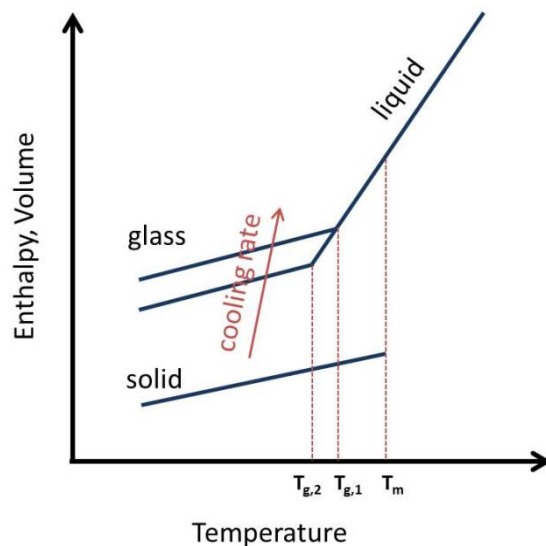


Fig. 2.2 Rapid cooling the liquid melt forms a solid glass. The glass transition temperature increases with increasing cooling rate

Although Turnbull's criterion was successful in predicting glass forming compositions, it was primarily limited to binary metallic alloys. Only after the advent of multi-component glasses (BMGs), several new alloy compositions were discovered. Next, the improvement in glass forming ability of bulk metallic glasses will be briefly discussed. The reason for the high glass forming ability of BMGs can be understood based on classical nucleation theory. By assuming steady state homogeneous nucleation in an undercooled liquid, the nucleation rate can be determined by

$$I = AD \exp\left(\frac{-\Delta G^*}{KT}\right) \quad (2.1)$$

where A is a constant, D is the effective diffusivity and ΔG^* is the activation energy for the formation of stable crystal nuclei, which can be calculated according to the equation,

$$\Delta G^* = \frac{16\pi\sigma^3}{3\Delta G_{l-s}^2},$$

in which σ is the interfacial energy between crystal nuclei and the liquid phase, ΔG_{l-s} is the free energy difference between liquid and solid crystal phase [14]. It is clear from eq. 2.1 that a low crystal nucleation rate is possible when the activation barrier for nucleation (ΔG^*) is high, which implies ΔG_{l-s} is low and also, if effective diffusivity, D is low.

The driving force for crystallization (ΔG_{l-s}) can be calculated by the following equation:

$$\Delta G_{l-s}(T) = \Delta H_f - T\Delta S_f - \int_T^{T_0} \Delta C_p^{l-s}(T)dT + \int_T^{T_0} \frac{\Delta C_p^{l-s}(T)}{T}dT \quad (2.2)$$

where ΔH_f , ΔS_f is the enthalpy and entropy of fusion respectively at temperature T_0 , the temperature at which crystal and liquid are in equilibrium [14]. From eq. 2.2, we can deduce that to have a small ΔG_{l-s} , a small enthalpy of fusion and large entropy of fusion is necessary. High entropy of fusion can be facilitated by increasing the entropy of mixing which can be increased by the addition of many elements into a single system [14]. This is one of the primary reasons why multiple components are necessary to synthesize bulk metallic glasses.

As evident from eq. 2.1, another important parameter to avoid crystal nucleation is to reduce the effective diffusivity in the undercooled melt. According to classical nucleation theory of homogeneous nucleation, the diffusivities of elements in an alloy melt are a function of Stokes-Einstein equation [14]. Angell [58] plotted the viscosities of various glass forming organic and inorganic liquids and found that SiO_2 , which is one of the best glass formers, classified as a strong liquid, has a high melt viscosity while O-terphenyl, one of the weakest glass former which is classified as a fragile liquid, has a very low melt viscosity. Busch *et al.* [59] plotted the viscosity of undercooled Zr based BMG melts and found that it is high and close to that of SiO_2 . Based on the fragility plots, it was assumed that the high viscosity of BMG alloy melts slows down the diffusion of the constituent elements to form crystalline phases significantly and thus resulting in a stable undercooled liquid.

2.3 Structure of metallic glasses

Since metallic glasses are produced by supercooling the liquid metal into amorphous solid, it is assumed that the atomic order in metallic glasses is the same as frozen liquid state. The atomic order in metallic glasses is generally defined by short range order (SRO) and medium range order (MRO). Short range order is the arrangement of atoms in the first nearest neighbouring shell. Medium range order is defined by the structural feature beyond the first coordination shell up to ~1-2 nm [60].

Metallic glasses can form into different metastable states depending on the cooling rates, which mean that various atomic structures are possible. However, due to the absence of long-range order in metallic glasses, studying atomic structure experimentally at nanoscale requires sophisticated characterization techniques like EXAFS by synchrotron radiation, neutron diffraction etc. Such characterization tools would still give us an average picture of the amorphous structure. So, most often experimental results are supported by Monte-Carlo or MD simulations [46]. In spite of the difficulty in studying the structure of metallic glasses, there are a few proposed models, which can give us a preliminary understanding of their atomic structure.

One of the first structural models on metallic glasses has been proposed by Bernal based on dense random packing of atoms [61]. Although the model was successful in explaining the structure of monoatomic metallic glasses, it failed to explain the metal-metalloid glasses with pronounced short range order. Later, Gaskell [62] proposed a model based on the assumption that the nearest neighbour local units in metal-metalloid glasses have the same atomic structure as that of their corresponding crystalline phases with similar chemical composition. Gaskell's model explained the short range order in some metal-metalloid glass forming compositions but failed to fully elucidate the high stability of supercooled liquid state of some of the metal-metalloid glass forming compositions. The model also failed to explain the metal-metal based metallic glasses [46]. It is generally understood that good glass forming liquids have densities close to their corresponding crystalline phases (<0.5% of the density of the corresponding crystalline phase). So, dense packed icosahedral clusters are generally considered to be one of the fundamental structural units in metallic glasses [46]. Almost all the earlier models to explain the structure in metallic glasses are limited to understand the short range order in metallic glasses. This knowledge is not sufficient to explain the overall atomic structure in metallic glasses on a microscopic scale. Miracle [63] proposed the efficient cluster packing (ECP) model to explain the medium range order in metallic glasses based on FCC/HCP kind of packing. The model is fundamentally based on efficient packing of clusters. An extended structure is produced by assuming each solute centred cluster as a sphere and then packing these spheres in a FCC/HCP lattice type. Since this construction cannot extend beyond a few cluster diameters because of internal strains and topological frustration, the disordered nature of the metallic glasses is still retained. By using ECP model, Miracle was able to predict the bulk densities of several binary metallic glasses over a wide range of chemistry and composition [64]. Similar attempt was also made by Sheng *et al.* [65] to explain the medium range order in metallic glasses. They proposed that clusters can be packed in icosahedral ordering for better packing and the model was able to explain the structural features in some binary metal-metalloid systems.

As mentioned earlier, most experimental techniques give us an averaged picture of the real atomic structure. The first direct proof of visualizing the clusters was provided by Hirata *et al.* [66,67] by using spherical aberration corrected transmission electron microscopy. In this method, by making the TEM foils extremely thin in the order of 3-5 nm and using a ~ 0.36 nm coherent electron beam which is comparable to the size of single atomic cluster in

metallic glasses, they were able to see diffraction spots similar to that of a single crystal. Therefore, individual clusters could be determined based on the diffraction pattern and they were further confirmed by comparing them with structural predictions by MD simulations (see fig. 2.3).

Although several models were proposed till now to explain the structure of metallic glasses, there is not a single universal model, which could explain the structural features of amorphous alloys, particularly in multi-component alloys. However, it is important to understand the structure as it governs the physical properties of a metallic glass [60]. To illustrate the importance of atomic structure for mechanical properties like ductility or elastic modulus, the example of Cu-Zr metallic glasses can be considered. MD simulations have shown that close packed icosahedral clusters (Cu [0,0,12,0]) play an important role in determining the mechanical properties on Cu-Zr binary metallic glasses. As the atomic fraction of Cu is increased from 30 to 70 at.% in Cu-Zr binary alloys, the fraction of Cu-centred icosahedral clusters ([0,0,12,0]) increases, consequently, the ductility decreases and elastic modulus increases. This indicates that, properties like plasticity and elastic modulus depends on the packing of clusters in metallic glasses.

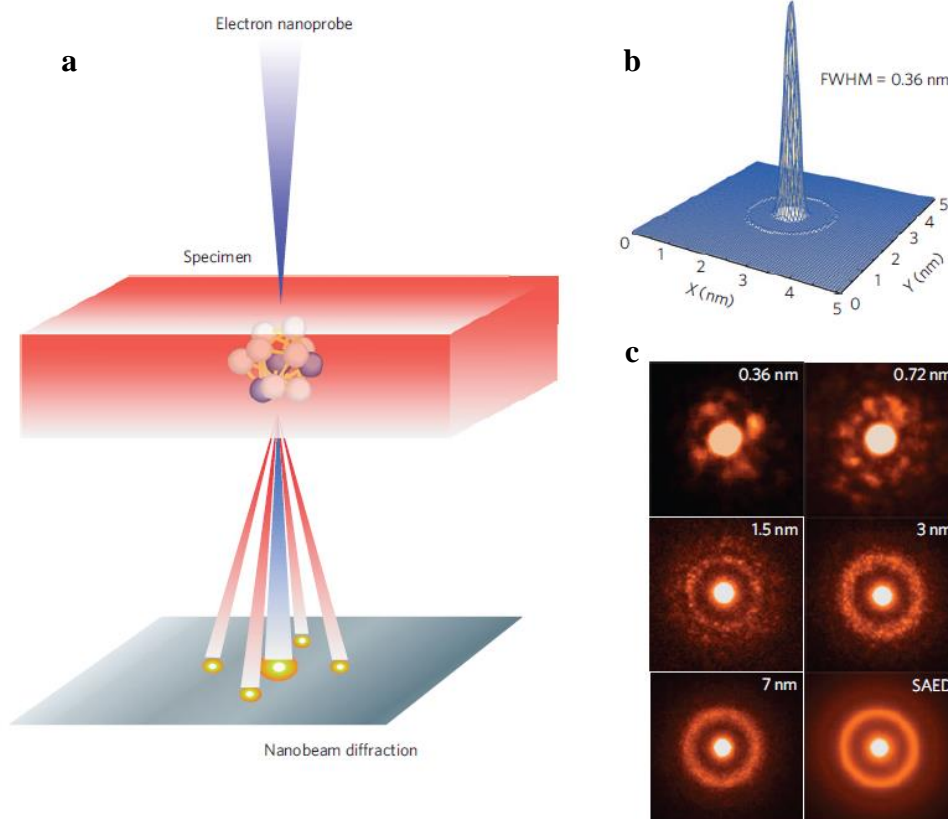


Fig. 2.3 (a) Schematic showing the principle of Angstrom beam electron diffraction, (b) Calculated 3-D profile of 0.36 nm electron beam (c) Electron diffraction patterns obtained by increasing the diameter of the beam. It can be clearly observed that by decreasing the size of the electron beam, diffraction patterns, which resemble those of crystalline regions can be obtained. (Reprinted with permission from Hirata *et al.* [67])

2.4 Deformation behaviour in metallic glasses

Metallic glasses have interesting mechanical properties like low elastic moduli and high strength compared to their corresponding crystalline phases as discussed in section 2.1. However, the major limitation of metallic glasses is their catastrophic failure during mechanical deformation. So, one of the major challenges in regard to mechanical properties of metallic glasses is improving their ductility. Before we discuss on how we can improve the plasticity in metallic glasses, it is important to understand the deformation behaviour at the atomic scale.

Unlike crystalline materials where the deformation mechanisms are easier to comprehend, lack of periodic structure makes it difficult to understand the deformation behaviour in metallic glasses. Initial research on mechanical properties was mostly confined to ribbons and flakes, which made it difficult to give a comprehensive picture on the deformation mechanism. However, the advent of BMGs made it possible to test the bulk properties and gain more understanding on their deformation behaviour [13]. When a load is applied to a metallic glass, strain can be readily accommodated by local rearrangement of atoms because of the metallic bonding even in the elastic regime. The generally accepted model is that the fundamental deformation unit in amorphous alloys is called a shear transformation zone (STZ). STZ is defined as a local inelastic rearrangement of a few atoms from one relatively low energy configuration to another configuration as shown in fig. 2.4(a) [13]. It was first proposed by Argon and Kuo [68]. MD simulations have shown that STZs are comprised of typically a few to ~100 atoms depending on the glass composition, local structure etc. [13]. It is widely accepted that sites with high free volume, which is dependent on the local chemical and topological structure, tend to form STZs easily since they can readily accommodate shear strain [5,13,69].

During the application of a load, like any other material, deformation in a metallic glass proceeds first by elastic deformation followed by a plastic regime. Brittle metallic glasses fail after elastic regime with very little or no plastic strain while ductile metallic glasses show some plastic strain (depending on the alloy composition) after elastic regime as shown in fig. 2.4(b). It must be pointed out here that although metallic glasses show compressive ductility, they show almost no ductility in tension [13,70]. Another important point to be observed in the typical stress-strain curve of ductile metallic glass is that there is no strain hardening mechanism in the plastic regime. However, there are a few reports claiming that strain hardening was observed in metallic glasses [23,71]. The main reason for such strain hardening is related to microstructural inhomogeneities like nanocrystals or confinement of shear band formation by geometric means.

First we discuss about the salient features in elastic deformation of metallic glasses. Elastic deformation in metallic glasses is quite interesting since they have high elastic strain limit, almost 2%. The bulk modulus of metallic glasses is ~ 6% less than that of the crystalline phase of the same composition (although several crystal phases are possible) [13,72]. This

can be explained by the less dense atomic packing in metallic glasses, which means that the interatomic spacing is larger compared to crystalline phases. However, the reduction in elastic and shear modulus of metallic glasses compared to corresponding crystalline phases is around 30%, which cannot be simply explained by a reduction in interatomic spacing [13,72]. It can be explained by the strain accommodation in regions of low density in a metallic glass. In a glass, there are regions of varying local density. During elastic deformation in an unrelaxed glass, such regions of low density deform more than the macroscopic strain. Although such deformed regions are few in number, the cumulative strain of all of them contribute to the massive reduction in the elastic and shear modulus [13].

After elastic deformation, permanent (plastic) deformation can occur in a metallic glass. Plastic deformation in metallic glasses can be sub-divided into two categories, homogeneous and inhomogeneous (heterogeneous) deformation. Homogeneous deformation can be subdivided into steady state and non-steady state flow. A steady state homogeneous deformation is defined where free volume creation and annihilation are balancing each other out whereas in a non-steady state, a gain or loss of free volume will occur during deformation [13]. Homogeneous deformation is typically observed at high temperatures normally above T_g (see fig. 2.4 (c)) [73]. It has direct relevance in shape forming operations. Inhomogeneous deformation by shear localization and eventual shear banding is a common mechanism at room temperature in metallic glasses as shown in fig. 2.4(d) [74]. Shear bands are formed by cooperative movement of several STZ's in a unified manner [13,70,75]. Shear localization in a metallic glass is a direct reason for the strain softening, which is caused by the local increase in free volume due to flow dilation. Because of this softening in the shear bands, metallic glasses show almost no ductility in tension [7,13,70].

Several factors like homologous temperature (T/T_g), strain rate, stress etc., determine the deformation behaviour in metallic glasses. Spaepen [76] constructed a deformation mechanism map for metallic glasses using the deformation theory based on free volume. One of the important highlights of the deformation map is the identification of the boundary between homogeneous deformation at low stress and high temperature from heterogeneous deformation at high stress and low temperature. At high stress, serrated flow or heterogeneous deformation is observed at temperature less than T_g . In this regime, deformation is localized in the form of a few shear bands (in most cases, only one) leading to heterogeneous deformation and causing failure in a prominent shear band. At temperature above T_g , deformation proceeds by viscous flow, where every volume element is sheared leading to a homogeneous deformation. From the deformation maps, one can also observe that the strength of the metallic glass is typically strain rate insensitive at low temperature. However, at extremely high strain rates, of the order of 10^3 s^{-1} , softening of the glass is observed due to the adiabatic shear localization. Similar deformation maps are also constructed based on strain rate and temperature. At low strain rate and low temperature, heterogeneous deformation is observed while homogeneous deformation can be observed at high temperature [13].

In the recent years, the effect of topological structure on the mechanical properties has been discussed quite extensively in the literature [5,77,78]. Topological structure is simply the arrangement of atoms in the glassy alloy. Ma [5] recently observed that the topological short range order (TSRO) in the glassy alloys plays a significant role in determining the mechanical properties like elastic modulus and plasticity of the alloy. Several variations of perfectly packed polyhedra (for example: [0,4,4,0], [0,3,6,0], [0,2,8,0], [0,2,8,1], [0,0,12,0], [0,1,10,2], [0,0,12,2], [0,0,12,3], [0,0,12,4] and [0,0,12,5]) with different coordination numbers (from 8 to 17) are possible in a metallic glass. By increasing the number of defects in the perfectly packed polyhedra, in other words, decreasing the number of five-fold bonds, several other polyhedra (for example: [0,5,2,1], [0,4,4,1], [0,3,6,1], [0,3,6,2], [0,2,8,2], [0,3,6,3] etc..) are possible in the glassy alloy. Although such defective SRO clusters are small in number individually, cumulatively they are observed in a significant number in the glassy alloy. These defective SRO clusters will determine the extent of plasticity in a metallic glass. However, it is also mentioned that such kind of correlation between defective short range order and plasticity can be made more easily for simple binary systems like Cu-Zr etc. In multi-component alloys, the chemical topological order is so much, it will be difficult to make predictions about such correlation [5]. Recently, it was also observed that such chemical and topological inhomogeneity in the structure leads to difficult cavitation and higher toughness values in Pd-Si alloys compared to Cu-Zr glasses [77].

Plasticity at room temperature is primarily controlled by the generation and arrest of shear bands. Strategies like introducing crystalline precipitates in the amorphous matrix [21,79], phase separated amorphous microstructures [25], severe plastic deformation of metallic glasses [23], intrinsic approaches like choosing elements with high μ/B values [80,81], geometrical constraints by testing nano-sized samples [82] have shown that plasticity in metallic glasses can be improved. All the strategies employed are based on free volume generation, which promotes shear band formation or by obstructing shear band propagation with the addition of secondary phases. The introduction of metallic nanoglasses is one such novel strategy which will be discussed in the subsequent sections. Interfacial regions in nanoglasses, which are characterized by free volume, can promote shear band formation improving their plasticity.

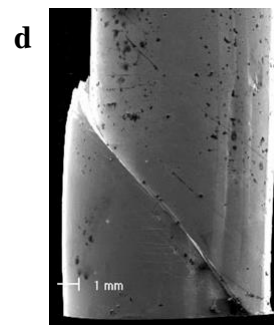
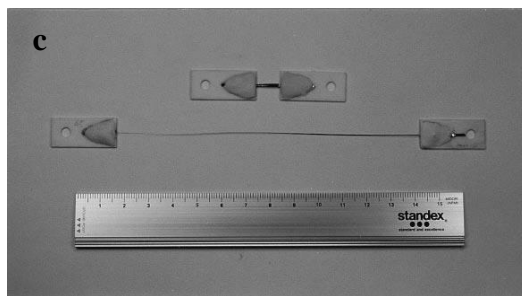
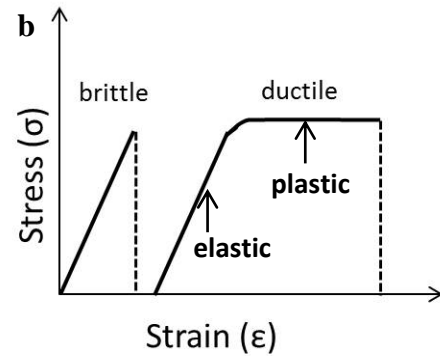
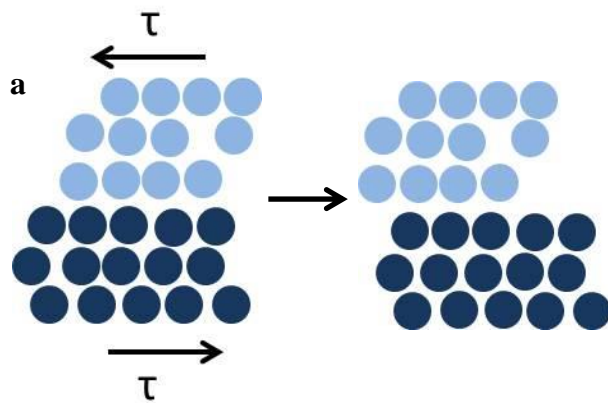


Fig. 2.4 (a) Schematic of a STZ after Argon and Kuo [62], (b) Schematic of a typical compressive stress-strain curve of a ductile and brittle metallic glass. Arrows indicate elastic and plastic deformation regions (c) Homogeneous deformation in $\text{Pd}_{40}\text{Ni}_{40}\text{P}_{20}$ metallic glass [73] and (d) Shear band in a Zr-based metallic glass [74] (Figures (c) and (d) are reprinted with permission from their respective publishers)

2.5 Metallic nanoglasses

In this chapter, the relevant literature on the nanoglasses published till now will be introduced. Metallic nanoglasses were proposed analogous to nano-crystalline materials synthesized by compacting amorphous nanoparticles [83,84] as shown in fig. 2.5. By varying the free volume in a metallic glass or changing the density of a glass, one would expect a significant change in physical properties of the material [84]. Interfaces, which form between the nanoparticles as shown in fig. 2.5(b) are characterized by increase in free volume [29]. This concept was first verified in the Pd-Fe-Si nanoglass composition synthesized by thermal evaporation in inert gas condensation [28]. Mössbauer spectroscopy of the nanoglass showed a shoulder in the quadrupole splitting (proportional to isomer shift), which is predicted to arise from the interfacial regions in nanoglasses. To verify this further, particle size is increased by increasing the gas pressure in the inert gas condensation and as expected, the interfacial component in the Mössbauer spectrum is reduced because of the increase in particle size. Several other metallic alloy systems like Au-Si, Au-La, Fe-Si, La-Si, Pd-Si, Ni-Ti, Ni-Zr, Ti-P were also synthesized later using IGC. However, no physical properties of these nanoglasses were studied in literature [85]. All the nanoglasses till now were synthesized by using thermal evaporation in inert gas condensation. This specific route has reproducibility issues in metal alloys which will be discussed in detail in experimental section 3.1.

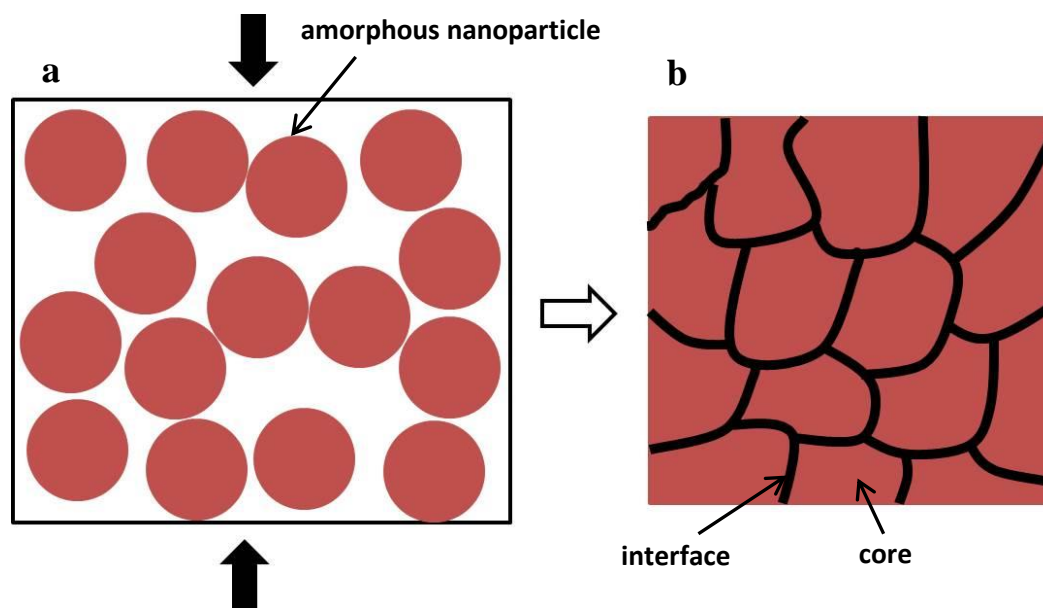


Fig. 2.5 Schematic of (a) consolidation of amorphous nanoparticles and (b) metallic nanoglass.

The real breakthrough in the research on nanoglasses came when the $\text{Sc}_{75}\text{Fe}_{25}$ nanoglass was synthesized by using thermal evaporation in IGC. As Sc and Fe have similar vapour pressures, Fe-Sc nanoglasses could be synthesized with much more reproducibility and their physical properties can be tested with a better reliability [29]. Exhaustive structural studies were conducted on this system by using positron annihilation spectroscopy (PAS), small

angle X ray scattering (SAXS) and transmission electron microscopy (TEM) to confirm the existence and analyze the interfacial regions in the nanoglass. Two positron life times i.e. 169 and 285 ps were detected, which were identified as the core and interfacial components, respectively, in PAS. This confirmed the presence of free volume in the interfacial regions. Sc segregation was observed on the surface of glassy nanospheres in TEM. The second composition, which was successfully made amorphous in IGC is $\text{Fe}_{90}\text{Sc}_{10}$ [30], which was found to exhibit ferromagnetic properties at room temperature. The reason for the ferromagnetic order was found to arise from the interfacial regions with enhanced free volume. However, recently Wang *et al.* [86] observed using analytical TEM that Fe segregates to the surface of $\text{Fe}_{90}\text{Sc}_{10}$ glassy spheres. Elemental segregation of one of the elemental constituents is observed in both the Fe-Sc nanoglass compositions. It is evident that chemical segregation to the interfacial regions will have influence on the physical properties of nanoglasses in addition to the effects of free volume. MD simulations have contributed significantly to our understanding of the interfacial structure in nanoglasses. Ritter *et al.* [42] found that the interfaces in $\text{Cu}_{64}\text{Zr}_{36}$ nanoglasses are characterized by defective short range order with a free volume of about 1-2%. Interfaces also remained stable on MD time scales even after annealing close to T_g . However, it was assumed that the core and the surface of the amorphous nanoparticles are chemically homogeneous. Later, Adjaoud and Albe [37] found surface segregation of Cu and Pd on $\text{Cu}_{64}\text{Zr}_{36}$ and $\text{Pd}_{80}\text{Si}_{20}$ amorphous nanoparticles, respectively. It was also found that compaction of such segregated nanoparticles does not only influence the interfaces but also the structure in the cores of the nanoparticles [87]. Danilov *et al.* [88] also found that segregation of one of the elements is possible in a $\text{A}_{80}\text{B}_{20}$ Lennard Jones potential system. Although, segregation is found both in experiments and simulations, they are performed on different material systems (Fe-Sc in experiments and Cu-Zr in simulations), which makes a direct comparison slightly difficult. In this regard, experiments and simulations were performed on Cu-Zr and Pd-Si glassy alloys in the present thesis so that a direct comparison can be made.

Recently, Au based thin film metallic nanoglasses have been synthesized by using traditional magnetron sputtering [28]. Since the films are amorphous in nature and have a nanogranular structure, they are also termed as nanoglasses. These Au based films are found to be ultrastable in a flash DSC measurement, which is attributed to the vapour deposition technique as well as the nanoglobular structure [36]. Similarly, NiTiCu nanoglass has also been synthesized using magnetron sputtering by Śniadecki *et al.* [32]. No segregation is reported for Au based nanoglass but an enrichment of Ti is found at the interfaces of NiTiCu nanoglass. Oxygen is also found in the Ti enriched regions [32]. It must be pointed out here that such a nanoglobular deposition is not entirely new in sputtering literature since such a film growth was earlier observed in amorphous thin films [89].

Properties like biocompatibility, enhanced ferromagnetism and improved plasticity have already been reported in metallic nanoglasses. Biocompatibility was found to be enhanced in a TiZrCuPd nanoglassy thin film compared to the melt-spun ribbons of a similar composition [90]. As mentioned earlier, $\text{Fe}_{90}\text{Sc}_{10}$ metallic nanoglasses synthesized by IGC are

ferromagnetic while the melt-spun ribbons are paramagnetic at room temperature. Interestingly, as-prepared $\text{Fe}_{90}\text{Sc}_{10}$ glassy nanoparticles were also found to be paramagnetic while the compacted nanoglass was found to be ferromagnetic at room temperature [30]. By using Mössbauer spectroscopy, it was observed that the interfaces have a different Fe environment (nearest neighbor atoms) compared to the core of the nanoglass giving rise to ferromagnetism in $\text{Fe}_{90}\text{Sc}_{10}$ nanoglass. Enhanced plasticity of Fe-Sc nanoglasses was also reported, which will be discussed in the subsequent section.

2.6 Deformation of metallic nanoglasses

As pointed out earlier, metallic nanoglasses were found to have enhanced plasticity compared to melt-spun ribbons of a similar composition. $\text{Sc}_{75}\text{Fe}_{25}$ nanoglasses showed plastic strain of around 3% while the melt-spun ribbons suffered catastrophic failure [33]. Multiple shear bands were observed in nanoglasses while the melt-spun ribbons showed only few shear bands as seen in fig. 2.6. Nanoindentation was carried out on $\text{Fe}_{90}\text{Sc}_{10}$ nanoglasses and it was found that homogeneous deformation is observed while inhomogeneous deformation is observed in melt-spun ribbons of the same composition [35]. Lower Young's modulus for $\text{Sc}_{75}\text{Fe}_{25}$ and higher Young's modulus for $\text{Fe}_{90}\text{Sc}_{10}$ nanoglasses compared to melt-spun ribbons of a similar composition were observed. Although segregation was observed in Fe-Sc metallic nanoglasses, it was not discussed in detail with regard to mechanical properties.

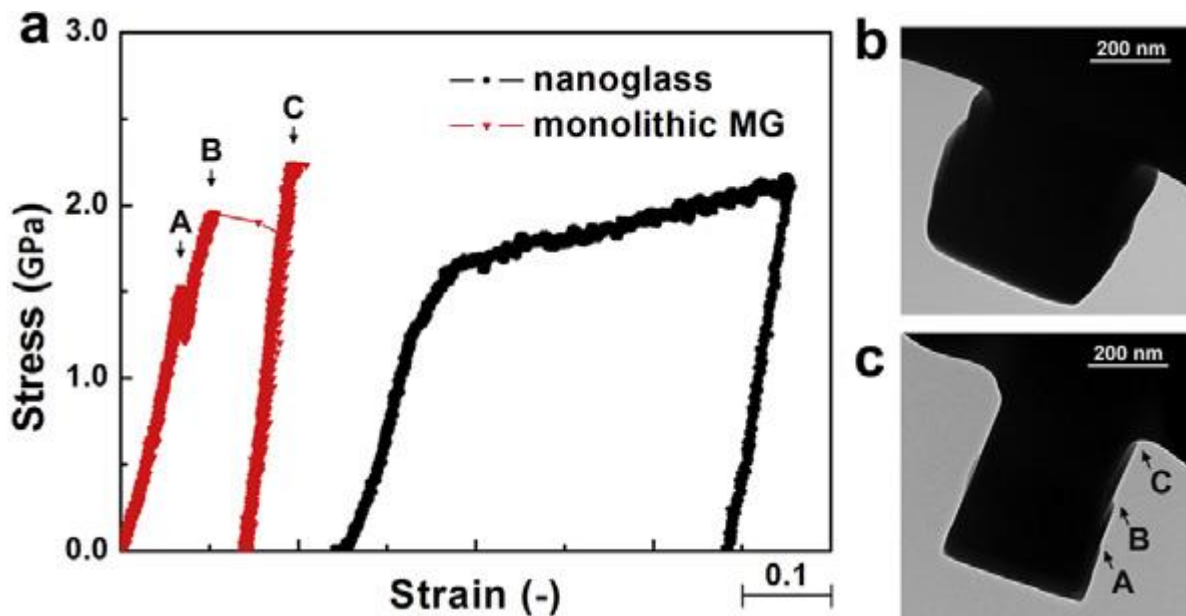


Fig. 2.6 (a) Compressive stress strain curves of a nanoglass and metallic glass with a diameter of 300 nm, tested micropillar of (b) nanoglass and (c) metallic glass. Reprinted with permission from ref.[34].

Additional evidence for the ductility improvement in metallic nanoglasses over conventional metallic glasses is provided by MD simulations in Cu-Zr alloys [39,41,91–94]. Homogeneous deformation is observed in Cu₆₄Zr₃₆ metallic nanoglasses while localized deformation in the form of shear banding is observed in metallic glasses. Sopy *et al.* [39] have observed that the interfaces in metallic nanoglasses are characterized by an enhanced free volume, lower SRO and an increased potential energy. This defective SRO at the interfaces makes them soft regions, which will shear first during mechanical deformation and since there are many nucleation sites for such shear events in a nanoglass, deformation proceeds more homogeneously compared to a conventional metallic glass. It was also observed that the homogeneous and inhomogeneous (segregated) metallic nanoglasses behave very similar to each other under mechanical load. Albe *et al.* [41] observed that the grain size of nanoparticles also plays a role in determining the mechanical properties of metallic nanoglasses. For smaller grain sizes (4 nm), deformation proceeded homogeneously while for large grain sizes (16 nm), it was more heterogeneous. It was found that the strength and elastic modulus of metallic nanoglasses is almost the same as that of metallic glasses if the grain size is increased to 16 nm while it is lower for small grain size of 4 nm. It must be mentioned here that most of the above mentioned simulations did not consider the effect of segregation on the interfacial structure and mechanical properties.

The topological structure at the interfaces is affected significantly by the change in chemistry, which in turn affects the free volume at the interfaces. This can affect the mechanical properties of the material such as shear band formation, plasticity of metallic nanoglasses and elastic modulus of the material. The effect of such segregation is not discussed in detail till now, which will be attempted in the present thesis.

3. Materials and Methods

3.1 Synthesis Techniques

3.1.1 Inert gas condensation (IGC)

Inert gas condensation is a bottom-up approach to synthesize metallic and ceramic nanoparticles from the gas phase [95]. Several metals and alloys like Al, Cu, Pd, Au, Ge, Ag-Al, Cu-Sn, Ni-Cu etc., were synthesized using IGC with particle sizes less than 100 nm. The fundamental principle of IGC involves evaporation of atoms, which collide with inert gas atoms in the chamber, lose their energy and nucleate as small powder particles close to the evaporation crucible. These nanoparticles subsequently grow in the chamber and are carried to the cold finger by convection current of the inert gas. There are several ways to evaporate the material in IGC like thermal evaporation, laser ablation, sputtering, plasma heating and electric arc discharge [95]. Among these, thermal evaporation is the most popular one because of its flexibility to prepare nanoparticles.

The primary problem to make metallic amorphous nanoparticles in thermal evaporation technique is the different vapor pressure of the constituent elements. Since metallic glasses form only in specific composition ranges, it is of utmost importance to have elements, which have similar vapor pressures. This limits the number of glass forming systems that can be made by in IGC. Fe-Sc nanoglass is one system that was successfully synthesized by IGC using thermal evaporation. So, to overcome this difficulty for other material systems, magnetron sputtering is employed instead of thermal evaporation in IGC in the current experiments. In this way alloys having different vapor pressures of the constituent elements can be synthesized with little compositional deviation from the starting material. In order to promote the cluster formation, sputtering is performed at relatively high pressure of $\sim 10^{-1}$ mbar (if compared to the growth of thin films at sputtering, where pressures in the range of 10^{-3} - 10^{-2} mbar are used), as under these conditions, the mean free path of sputtered atoms is sufficiently small to result in many collisions [96]. A disadvantage of sputtering at such high pressures is the re-deposition of sputtered atoms or formed clusters back onto the centre and on the edge of the race track of the target. To reduce these effects and increase the efficiency and rate of nanoparticle production, a continuous gas flow from the side of the target is adopted to drive away the metal atoms and ions from the target. Preliminary experiments with pure Cu suggested that the flow of either pure argon or helium resulted in low yield of material due to high amount of re-deposited material onto the target and less sputtering efficiency, respectively. Therefore, a mixture of Ar and He gas was used to improve the sputter yield and efficiency of nanoparticle production.

Experimental set-up of inert gas condensation:

$\text{Cu}_{50}\text{Zr}_{50}$, $\text{Cu}_{60}\text{Zr}_{40}$ and $\text{Pd}_{84}\text{Si}_{16}$ metallic nanoglasses were prepared by using direct current magnetron sputtering in an inert gas condensation (IGC) system shown in fig. 3.1. The composition of the metal target used for sputtering is $\text{Cu}_{50}\text{Zr}_{50}$, $\text{Cu}_{60}\text{Zr}_{40}$ and $\text{Pd}_{80}\text{Si}_{20}$. In the first step, the chamber was evacuated to a pressure of $\sim 10^{-7}$ mbar, subsequently, a flow of 100 sccm of argon and 20 sccm of helium gas was continuously led into the chamber while reduced pumping maintained the desired gas pressure of 0.3 mbar throughout the sputtering process. The sputtering power was set at 420 W and the resulting condensed clusters were collected on a liquid nitrogen-cooled cylinder (referred to as cold finger), from which the collected powder was scraped off and collected in a small cup. After finishing the sputtering and collection of a sufficient amount of powder, the chamber was evacuated again to a pressure of $\sim 10^{-7}$ mbar. After transferring the collection cup to a compaction unit attached to the synthesis chamber, the compaction was performed at a pressure of 1 GPa. Subsequently, the pellet was transferred in a sealed glass tube without exposure to air to a glove box where subsequent compaction at 3 GPa was done with a hydraulic press. Further compaction was done using Bridgeman-type anvils made of tungsten carbide at a high quasi-hydrostatic pressure of 6 GPa in air. The yield of the condensation process is roughly 50 mg in 1 h. The optimization of process parameters will be described in detail in chapter 4.

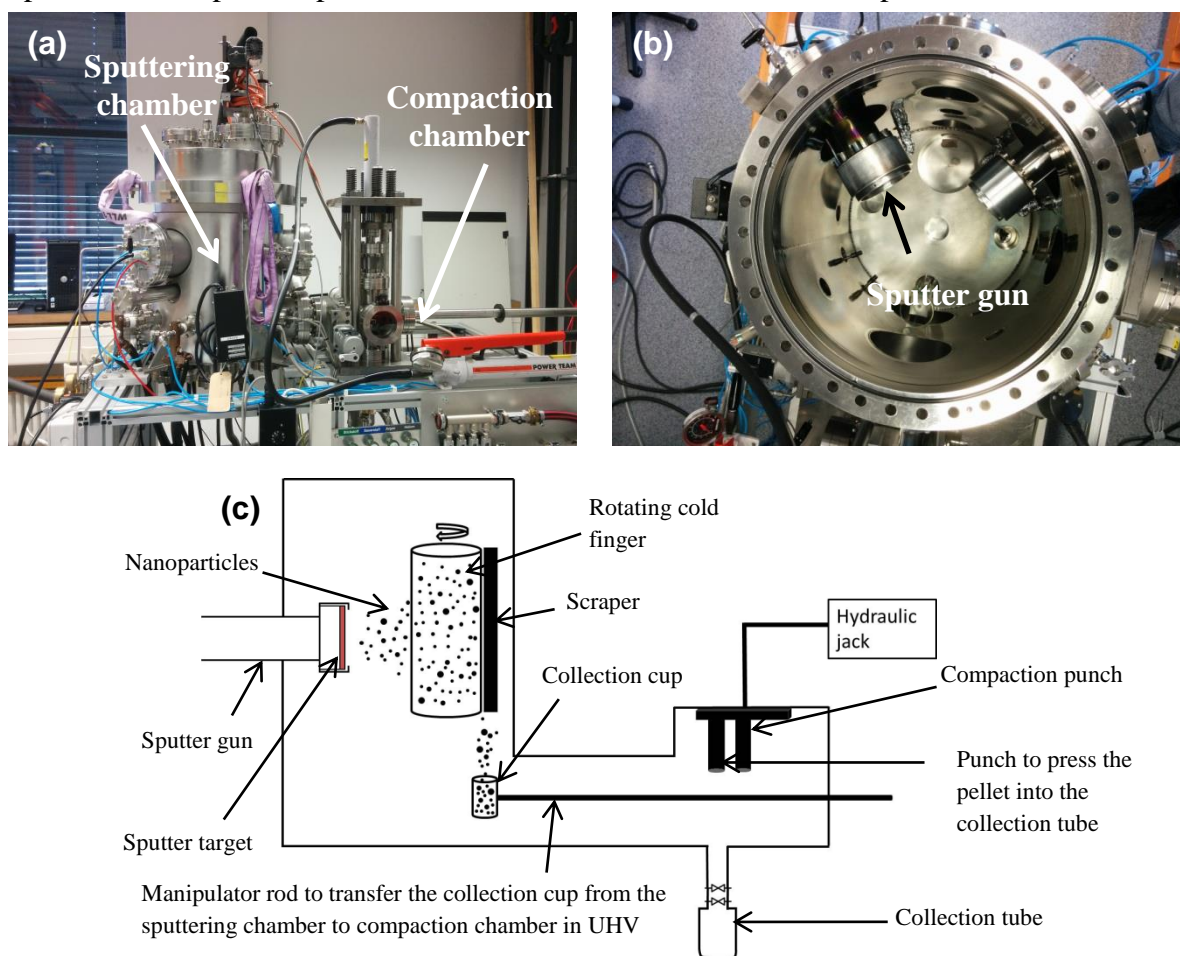


Fig. 3.1 (a) Inert gas condensation set-up used to synthesize the nanoparticles, (b) Top view of the inside of the chamber showing the sputter gun and (c) Schematic showing the IGC process

3.1.2 Magnetron sputtering

Magnetron sputtering is a common technique to synthesize thin films of different kinds of materials. Good composition control is a major advantage of the magnetron sputtering technique. In the basic sputtering process, a cathode (target material) plate is bombarded by energetic inert gas ions generated in a glow discharge plasma causing the removal (sputtering) of atoms, which then condense on a substrate as a thin film as shown in fig. 3.2(a). During the process of sputtering, secondary electrons are generated, which keeps the plasma stable. Magnetrons confine the secondary electrons in the vicinity of the target, which helps to increase the ionization efficiency of the whole process. The increased ionization efficiency of the process also helped in reducing the operating pressures from 10^{-2} to 10^{-3} mbar and operating voltages from a 2-3 kV to ~ 500 V [97].

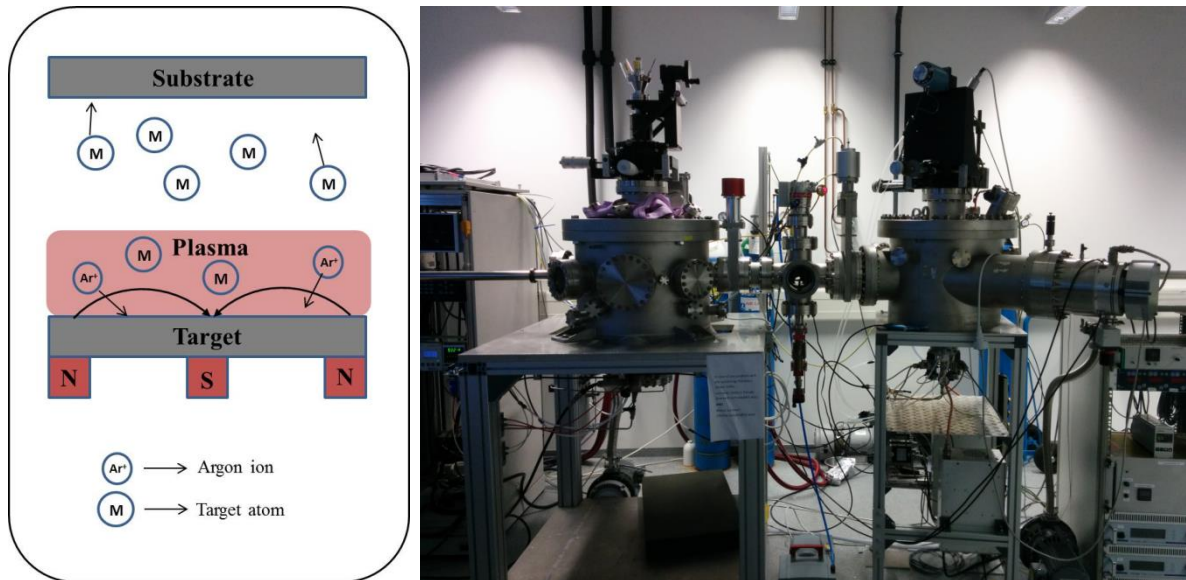


Fig. 3.2 (a) Schematic explaining the principle of magnetron sputtering, (b) Magnetron sputtering unit used to deposit thin films

$\text{Pd}_{80}\text{Si}_{20}$ thin films were synthesized by co-sputtering elementally pure Pd and Si targets using direct current magnetron sputtering shown in fig. 3.2(b). The angle of deposition between the target and the substrate is 32° . The base pressure of the sputtering chamber is in the order of 10^{-8} mbar. Sputtering was carried out at a pressure of 9×10^{-3} mbar at an argon gas flow of 100 sccm. The power used for sputtering Pd and Si targets is 30 and 60 W, respectively. Si substrates were used for depositing thin films. The thickness of the film is measured by profilometry. The films were sputtered for 150 and 300 min to obtain a thickness of 850 nm and 2000 nm for nano indentation and micropillar testing, respectively.

3.1.2 Melt spinning

Melt-spinning is done by standard commercially available melt-spinning technique in a Edmund Buhler machine. A large Cu wheel is rotated at a certain speed onto which the molten metal alloy is poured, which condenses the liquid metal in the form of ribbons. The whole chamber is evacuated and refilled with Ar gas at least three times in order to minimize the contamination with oxygen during the synthesis. Melt-spinning is performed at Ar pressures of a few mbar. Cu-Zr melt spun ribbons were prepared by Dr. Z. Sniadecki at the Institute for Molecular Physics in Poznan and Pd-Si ribbons were prepared in the group of Prof. J.Eckert at IFW Dresden.

3.2 Characterization techniques

3.2.1 X-ray diffraction

When a beam of X-rays (electromagnetic radiation) is incident on a periodic array of atoms such as a crystal, X-rays interact with the electrons in the atoms and are scattered. When the X-rays interact with electrons, they produce secondary spherical waves emanating from the electrons. This phenomenon of X-ray scattering is called elastic scattering. The constructive interference of such elastically scattered X-rays proceeds according to Bragg's law as stated below

$$n\lambda = 2d\sin\theta \quad (3.1)$$

Where n is the order of diffraction, λ is the wavelength of X-rays, d is the inter-atomic spacing and θ is the incident angle.

X-ray diffraction (XRD) was carried out using Philips XPERT-MP diffractometer and Mo $K\alpha$ X-ray source in a Bragg –Brentano geometry for the melt-spun ribbons and nanoglass samples synthesized by IGC. Thin films were characterized by grazing incident X-ray diffraction with an incident angle of 0.5° in a Bruker D8 DISCOVER diffractometer with Mo $K\alpha$ X-ray source. The thin film samples were placed on specially designed substrate adjusted to the correct plane of diffraction.

3.2.2 Scanning electron microscopy

Scanning electron microscopy was performed on all the samples using a Leo 1530 Field Emission Scanning Electron Microscope (FE SEM) with a EDS attachment to check the chemical composition. All the measurements were performed at least three times to confirm the compositional homogeneity. All the composition values presented in this thesis are within 2 at.% error. Sample polishing was not performed before the EDS measurements on the IGC samples.

3.2.3 Transmission electron microscopy

Transmission electron microscopy (TEM) was carried out using an aberration (image) corrected FEI Titan 80-300 electron microscope operated at 300 kV. The powder sample used for TEM analysis was collected directly from the cold finger. Some of the samples were also characterized using a FEI Tecnai electron microscope. TEM lamellae of the nanoglass and indented samples were prepared using focused ion beam (FIB) (FEI Strata 400 STEM) and further thinned by low-voltage argon ion milling (Fischione Nanomill 1040) to make them electron transparent. Pd-Si thin film samples were deposited directly on a carbon coated copper grid and observed in a TEM.

All TEM measurements were performed in collaboration with Dr. Di Wang and Dr. Xiaoke Mu from Institute of Nanotechnology, KIT.

3.2.4 Atom probe tomography

Atom probe tomography (APT) is a combination of a field-ion microscope with a time of flight mass spectrometry. The basic principle involves successive removal of atoms from a sharp tip and then coupling this with time of flight mass spectrometry, individual atoms can be identified. The removed atoms can be reconstructed in 3D using computer software. In a normal working mode, the atoms are evaporated in a controlled manner onto a position sensitive detector positioned 10-100 cm away. The first step in APT measurement is to produce a sharp tip with a radius of about 100 nm using electrolytic polishing or by FIB. Then the tip is placed in a UHV chamber, where the tip is cooled down to cryogenic temperatures, typically to 20-100 K. The atoms are evaporated from the tip by either using a laser source or by applying an electric field in a pulse mode. Normally, the pulse amplitude and voltage on the specimen are controlled for the evaporation of one atom to ionize at a time but multiple ionizations are possible. The delay between the application of the pulse and the detection of ion at the detector allows the determination of the mass to charge ratio. If the material contains elements (with different valence states) with close mass to charge ratio, then the identification of the elements can be slightly difficult. Apriori knowledge of the sample composition helps in identifying the possible elements in APT. Once, a sufficiently large number of atoms are collected on the detector, typically a few million, then the reconstruction of the atoms is performed to a tip shape using a geometric algorithm. When working in voltage pulse mode, choosing appropriate voltage is important since preferential evaporation of one of the atoms may occur leading to biased compositions. Also, in voltage pulse mode, the full potential energy was not transferred to the ions as they were field evaporated from the surface of the specimen, which are termed as „energy deficits“. Such problems can be avoided by using laser pulsing mode, which has become very popular in the recent times since the pulse duration, irradiated volume magnitude and absorbed energy are orders of magnitude smaller, much better controlled and well understood [98,99].

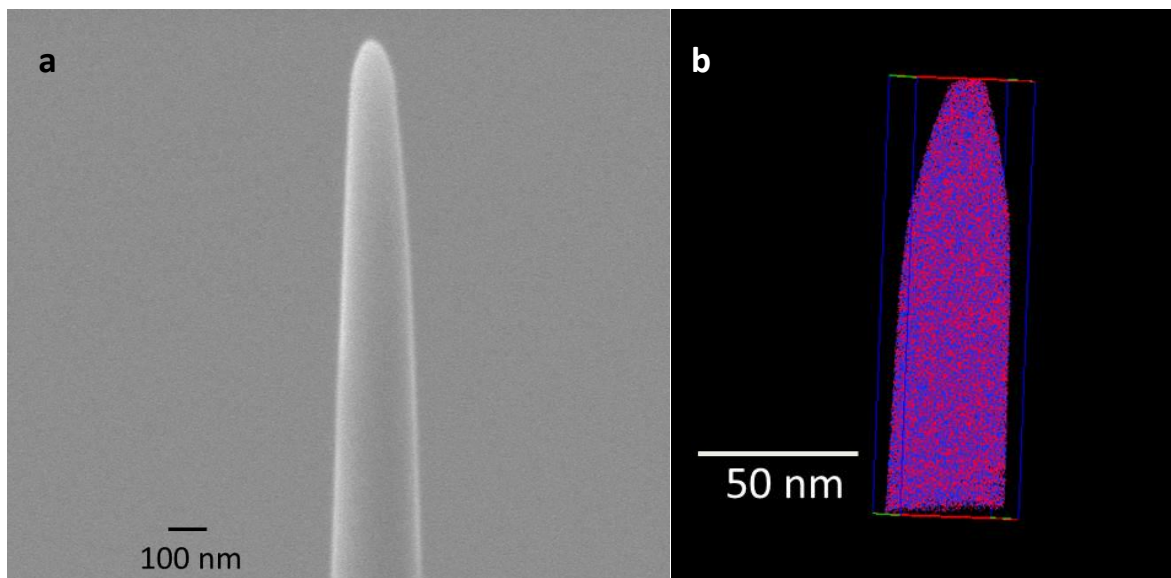


Fig. 3.3 (a) $\text{Cu}_{50}\text{Zr}_{50}$ APT tip prepared by FIB, (b) Reconstructed tip with Cu atoms in red and Zr in blue

The samples for atom probe tomography analysis were prepared by a standard lift-out method using a FEI Strata 400 STEM and a Zeiss Auriga 60 FIB. Annular milling was used to obtain needle-shaped APT samples with a typical radius of curvature of about 100 nm. The final FIB “clean-up” procedure was carried out at low voltages (5, 3.5 and 1 kV) towards the end to ensure the minimum content of uncontrolled impurities (Ga impurities, if any). Important steps of the FIB milling process can be found in Ref. [99,100]. The APT measurements were carried out using a Cameca-LEAP 4000X HR instrument in laser pulsing mode (wavelength 355 nm, pulse frequency 100 kHz, sample temperature 60 K, pulse energy 60 pJ, evaporation rate 1%). The reconstruction of the APT data was performed with IVAS 3.6.14. A sample of APT tip used for measurement and reconstructed tip are shown in fig. 3.3

All APT measurements were performed in collaboration with Dr. Torben Boll at IAM-Werkstoffkunde, KIT and Dr. M.R. Chellali from INT, KIT

3.2.5 Differential Scanning Calorimetry

Differential scanning calorimetry is a technique in which the heat flow to a sample is measured maintaining the same temperature in both the reference and sample crucibles. Whenever a phase transition occurs, depending on whether it is endothermic or exothermic, the additional heat added to or removed from the sample is measured as a function of temperature. DSC is a widely used technique to determine thermodynamics and kinetics of several phase transitions like melting, crystallization reactions, oxidation reactions etc. Glass transition is a phenomenon, which is of scientific interest and can be detected as there is a change in the heat capacity of the sample and it is recorded as a step in DSC scan.

Differential scanning calorimetry was carried out using a Netzsch DSC (at the Institute of Molecular Physics, Polish Academy of Sciences, Poznan) under high purity argon atmosphere at a flow rate of 100 sccm. The samples were tested at a heating rate of 20 °C/min in Al₂O₃ crucibles. To verify that the curves are reproducible, all the samples were also re-tested in a Netzsch High pressure DSC (at the Institute of Nanotechnology, Karlsruhe Institute of Technology, Karlsruhe) in high purity He atmosphere. The difference between the onset and peak crystallization temperatures measured by both DSCs was less than 2 °C.

3.2.6 Density measurements

Density measurements are based on Archimedes principle. Archimedes principle states that the upward buoyant force that is exerted on a body immersed in a fluid, whether fully or partially immersed is equal to the weight of the fluid that the body displaces and acts upwards at the center of the mass of the displaced fluid. Based on this principle, density of a material can be calculated by using the formula below:

$$\rho_m = \left(\frac{W}{W-W_l} \right) \times \rho_l \quad (3.2)$$

where ρ_m is the density of the material, w is the weight of the material in air, w_1 is the weight of the material in the liquid and ρ_l is the density of the liquid. Bulk density of Pd-Si samples was measured using this formula using dimethyl phthalate as the liquid medium (density of dimethyl phthalate = 1.19 g/cm³).

Pd-Si samples were tested using standard Archimedes method while Cu-Zr samples were tested using a modification of this method developed by Kilmametov *et al.* [101]. The principle of the technique is to find out the volume of the material by observing the amount of liquid displaced using a laser confocal microscope. Small holes were drilled in a plate, which was coated with a hydrophobic surface while the interior of holes were coated with hydrophilic layer, which were then filled with dimethyl pthalate. Since the edges of holes are hydrophobic, the liquid forms a concave meniscus with a height, h , which can be measured by a laser confocal microscope with an accuracy of $\pm 0.5 \mu\text{m}$. The volume of the material can be calculated according to the formula, $V = V_h - V_m$, where V is the volume of the material, V_h is the volume of the hole and V_m is the volume of the meniscus, which is $V_m = \frac{\pi h (3r^2 + h^2)}{6}$, where h is the height of the meniscus obtained from the laser confocal measurement and r is the radius of the hole. For more details on the measurement technique, the reader is referred to ref. [101].

Now, by adding small pieces of known weight of the material sequentially, the meniscus rises and its height is monitored for each piece added. By plotting the volume of each piece, the slope of the straight line fit gives the density of the material as shown in fig. 3.4.

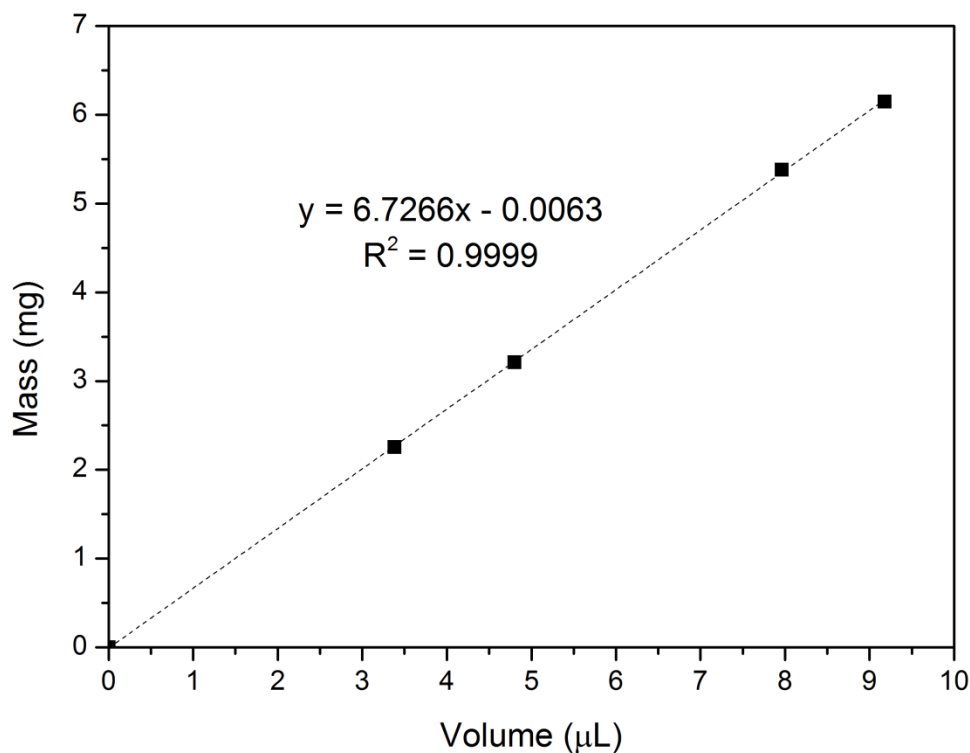


Fig. 3.4 Plot of mass vs. volume of a $\text{Cu}_{50}\text{Zr}_{50}$ nanoglass sample. The slope gives the density of the material in g/cm^3 .

Density measurements by laser confocal microscopy were performed by Dr. Askar Kilmametov of INT, KIT.

3.2.7 Focused Ion Beam Milling

Focused ion beam was used for the preparation of TEM and APT samples and micropillars for *in situ* in SEM compression tests. FIB milling uses a finely focused beam of Ga^+ ions that can be operated at low beam currents for imaging and high beam currents for milling. The sample is irradiated with Ga ions, which sputter the sample from the surface leaving it as either neutral atoms or charged ions [102]. Because of the high energy of Ga ions, implantation of Ga into the specimen surface is possible. Most of the APT tips have a few nm of Ga implantation layer only on the top surface of the tip, which was removed during analysis. Very low currents were used during the preparation of TEM lamella for imaging to minimize the damage caused by Ga implantation. Pt is deposited by *in-situ* electron beam deposition on the samples during the preparation of micropillars, APT tips and TEM lamella to minimize the Ga ion implantation.

Milling pillars of micron size out of melt-spun ribbon and IGC samples was done by FEI Strata 400 STEM using Ga ions. Micropillars of thin film samples were milled using Nova 200 Nanolab (FEI, Inc) machine. All the pillars were milled in four steps. To minimize the damage caused by Ga ions, very low currents of 260 and 90 pA were used in the final two steps of milling process. The milling parameters were optimized such that the taper of the

pillars is less than 3 degrees. A sample image of the micro machined pillars using FIB is shown in fig. 3.5.

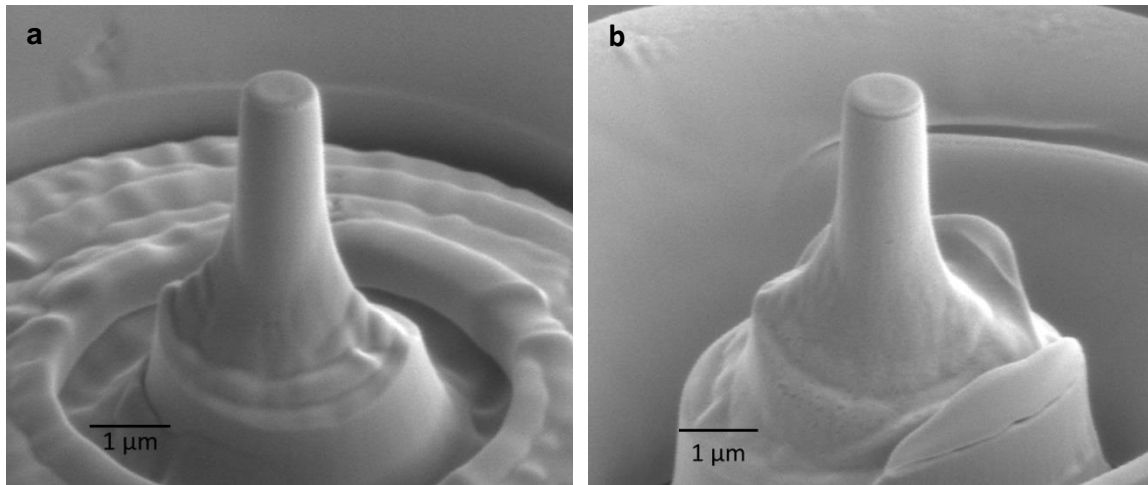


Fig. 3.5 Micropillars of (a) Pd₈₀Si₂₀ nanoglass (b) HPT-processed Pd₈₀Si₂₀ nanoglass

3.2.8 Oxygen analysis

Carrier gas hot extraction method is a technique used to determine the amount of oxygen in samples, predominantly for metals, alloys etc. The procedure involves selective reduction of oxygen in the sample by carbon and its quantitative detection. The amount of oxygen is directly correlated with the amount of CO_x formed, which can be detected quantitatively. For more details on the experimental procedure, the reader is referred to ref. [103]. Since the amorphous powder is nanometric in size, each sample is prone to oxidation. So, the oxygen content of the as-prepared nanoglasses was determined using one or two arbitrary samples of each composition by carrier gas hot extraction method using TC600, LECO machine. It was found that the average oxygen content in all the samples is less than 2 at.%. We believe that the oxides mostly cover the specimen surfaces and the open porosity.

Oxygen analysis of the nanoglass samples was performed by Dr. Thomas Bergfeldt of IAM-Applied Materials Physics, KIT.

3.3 Mechanical testing

3.3.1 Indentation measurements

Indentation is one of the common mechanical testing methods and is used to determine the hardness of a material. Hardness is the quantification of a material's resistance for plastic deformation. Several indentation techniques are possible depending on the type of geometry of the indenter. Different types of indenter materials are used based on the indentation technique, for example tungsten carbide or hardened steel ball indenter for Brinell hardness test, diamond indenter for Vickers and Knoop hardness testing methods. Vickers hardness is

one such technique where the indenter is in the shape of square-base pyramid. The included angle between the opposite faces of the pyramid is 136° [104]. Vickers hardness number (HV) is defined to be the ratio of force (F) and area (A) where F is the force applied in kg-f and A is the surface area of the indent in mm^2 . The surface area (A) of the indent in a Vickers indent can be determined by the formula

$$A = \frac{d^2}{2 \sin 68^\circ} \approx \frac{d^2}{1.8544} \quad (3.3)$$

where $d = (d_1 + d_2)/2$, the average of the diagonals of an indent as shown in fig. 3.6

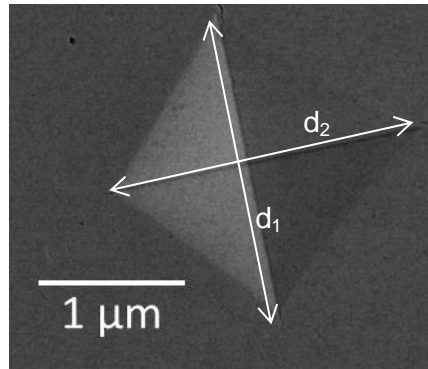


Fig. 3.6 A Vicker's indent of a $\text{Cu}_{50}\text{Zr}_{50}$ sample. The average of diagonals d_1 and d_2 is used to calculate the area of the indent

Vicker's hardness is calculated according to the formula [104],

$$HV = \frac{F}{A} \approx \frac{1.854F}{d^2} \left(\text{in } \frac{\text{kg-f}}{\text{mm}^2} \right) = 0.1892 \frac{F}{d^2} \left(\text{in } \frac{\text{N}}{\text{mm}^2} \right) \quad (3.4)$$

Hardness measurements were carried out using a Buehler Micromet-5104 machine after polishing the samples with standard metallographic techniques. All the loads were applied for a constant time of 15 s. The distance between neighbouring indents was at least three diagonal lengths.

Nanoindentation is another form of indentation technique to test small volumes. The fundamental principle is similar to any other indentation technique, where the hardness is calculated as the ratio of force and area. The benefit of nanoindentation technique is that the penetration depth into the material is known at any point, which can enable us to calculate the contact area of the indenter at any instant. Since the load and penetration depth are known, they can be plotted as shown in fig. 3.7. An additional advantage of nanoindentation is the possibility to calculate the Young's modulus of the material. The stiffness of the contact can be calculated from the unloading slope of the load-displacement curve. The stiffness of the contact can be used to calculate the reduced Young's modulus (E_r) based on the formula

$$E_r = \frac{1}{\beta} \frac{\sqrt{\pi}}{2} \frac{S}{\sqrt{A_p(h_c)}} \quad (3.5)$$

Where $A_p(h_c)$ is the projected contact area at the depth h_c , β is the geometrical constant of the order unity and S is the stiffness of the contact.

The reduced Young's modulus is related to the Young's modulus by the following relationship:

$$\frac{1}{E_r} = \frac{1-\nu_i^2}{E_i} + \frac{1-\nu_s^2}{E_s} \rightarrow (3.6)$$

Where E_r is the reduced Young's modulus, E_i and E_s are the Young's moduli of the indenter (in this case, diamond) and sample respectively and ν_i and ν_s are the Poisson's ratio of the indenter and sample, respectively [105,106].

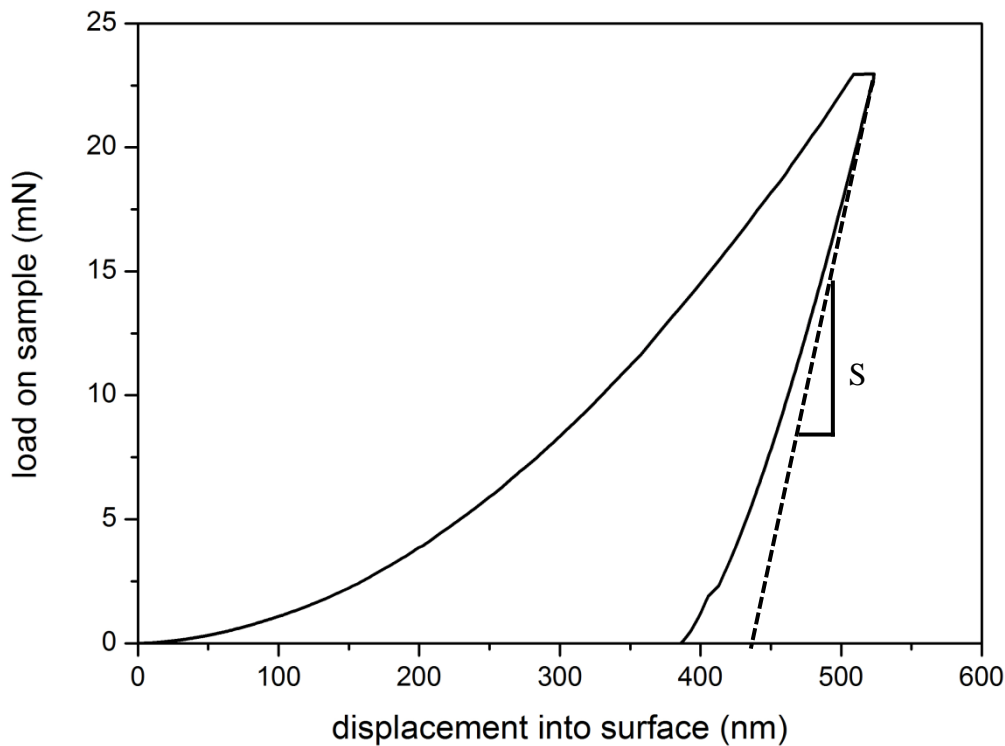


Fig. 3.7 Load-displacement curve for a HPT-processed $\text{Pd}_{84}\text{Si}_{16}$ nanoglass. S is the stiffness of the contact calculated from the slope of the unloading portion

By using constant loading rate, equivalent indentation strain rate can be obtained [107]. Hardness obtained by a Berkovich indenter is equal to

$$H = \frac{P}{A} = \frac{P}{ch^2} \rightarrow (3.7)$$

$$P = cHh^2$$

where H is the hardness, P is the applied load, A is the projected contact area, h is the depth of indentation and $c = 24.56$ for Berkovich geometry. Differentiating the eq. 3.8 with respect

to time, one can obtain the following formula (eq. 3.8) for indentation strain rate by assuming that the hardness is independent of the indentation depth.

$$\begin{aligned}\frac{dP}{dt} &= ch^2 \frac{dH}{dt} + 2cHh \frac{dh}{dt} \\ \dot{P} &= \left(\frac{P}{H}\right)\dot{H} + \left(\frac{2P}{h}\right)\dot{h} \\ \frac{\dot{P}}{P} &= \left(\frac{\dot{H}}{H}\right) + \left(\frac{2\dot{h}}{h}\right) \\ \dot{\varepsilon}_i &= \frac{\dot{h}}{h} = \frac{1}{2} \left(\frac{\dot{P}}{P} - \frac{\dot{H}}{H} \right) \rightarrow (3.8)\end{aligned}$$

When hardness does not change over time, one can assume eq. 3.8 as

$$\dot{\varepsilon}_i = \frac{\dot{h}}{h} \approx \frac{\dot{P}}{2P} \rightarrow (3.9)$$

The nanoindentation measurements can be performed in a quasi static and continuous stiffness measurement (CSM) mode. In quasi-static mode, the stiffness is measured by analyzing the force vs displacement curve after the unloading. In CSM mode, the stiffness is measured continuously throughout the measurement by superimposing a small force several orders of magnitude smaller than the nominal load.

For the nanoindentation experiments, a Nanoindenter G200 DCM II (Agilent Technologies, now: Keysight Technologies, USA) equipped with a diamond Berkovich (a three sided pyramid geometry) tip was used. The CSM frequency and amplitude were set to 75 Hz and 1 nm, respectively. Multiple indents were performed on the samples and the average values were presented. All the samples for micro and nano indentation measurements were glued to a metal holder.

Nanoindentation measurements were performed in collaboration with Dr. Ruth Schwaiger of IAM-Werkstoff- und Biomechanik, KIT

3.3.2 Microcompression testing

Although indentation is a simple and widely used technique, the triaxial stress field beneath the indenter makes it difficult to analyze the deformation behaviour. Uniaxial compression testing can solve such a problem. Since the advent of nanotechnology, micro mechanical testing has become very popular because one can test small specimens.

Although it is a powerful technique to determine the mechanical properties, one has to be careful of some of the limitations of this testing method. Factors like taper of the pillars,

effect of substrate etc. should be taken into account while determining properties like Young's modulus, Yield stress of the material etc. It is recommended that the taper of the pillar should be as little as possible, typically less than 3°. The effect of the substrate must also be considered when performing the analysis. For a compliant substrate, the pillar will sink upon compression, which will lead to inaccurate measurement of the pillar deformation. Typically, the sink in of the pillar into the substrate can be considered by using Sneddon's solution [108]. Based on this, a perfectly rigid circular flat punch indenting into an elastic half space would have the contact compliance as defined by the equation:

$$C_{Sneddon} = \frac{\sqrt{\pi}(1-\nu^2)}{2E\sqrt{A}} \quad (3.7)$$

where ν is the Poisson's ratio of the substrate, E is the Young's modulus of the substrate and A is the instantaneous cross-sectional area of the pillar.

The actual displacement is then $\Delta x_{actual} = \Delta x_{total} - \Delta x_{substrate}$

where Δx_{total} and $\Delta x_{substrate}$ are the total displacement and the displacement of the substrate respectively. Δx_{total} is the measured value from the experiment and

$$\Delta x_{substrate} = \frac{(1-\nu_{sub}^2) \cdot f}{2E_{sub} \cdot r_{base}}$$

where ν_{sub} is the Poisson's ratio of the substrate, r_{base} is the radius of the base of the pillar, E_{sub} is the Young's modulus of the substrate and f is the force applied on the pillar [109].

It is already well known that metallic glasses show plasticity on a nanometer scale [82]. The ability to restrict shear band generation and propagation by restricting the size of the sample makes metallic glasses more ductile. Several reports exist on the size dependent deformation of metallic glasses, which were reviewed by Greer and De Hosson [110]. Keeping this in mind, the diameter of the pillars is chosen to be $\sim 1 \mu\text{m}$ so that such effects do not play a role in the current work.

Microcompression testing was carried out using Insem (Nanomechanics Inc.) machine with a flat indenter of $5 \mu\text{m}$ in diameter. Although they were tested in different conditions, each sample was tested only once. So, a good statistical input is required to make a conclusion about the modulus or strength values. We will mainly focus on the deformation behavior of different samples synthesized by different techniques and compare them with deformation behavior of melt-spun samples. For engineering stress calculations, full width half maximum diameter of the initial pillar is considered. To calculate the engineering strain, only the portion of the initial pillar which is uniform in diameter is considered. The compliance of the material under the pillar is calculated by using eq. 3.7 and subtracted from the total displacement to calculate the final engineering strain.

Micropillar tests were performed in collaboration with Dr. Ruth Schwaiger of IAM-Werkstoff- und Biomechanik, KIT.

3.4 MD simulations

To investigate the origin of shear band formation in Pd₈₄Si₁₆ nanoglass pillars during the uniaxial compression tests, we performed molecular dynamics simulations on Pd₈₀Si₂₀ metallic glass and nanoglass pillars by using the LAMMPS simulation package [111] with an embedded atom method (EAM) potential for Pd-Si [112]. This potential has been optimized to predict accurately the structure of the liquid and amorphous Pd-Si alloys around the eutectic composition Pd_{100-x}Si_x (x=17.5) and successfully applied to Pd-Si glasses [77,113,114]. The equations of motion were numerically integrated with a time step of 2 fs. Periodic boundary conditions were applied in all three directions in metallic glass and nanoglass samples. Temperature and pressure were controlled by a Nosé-Hoover thermostat and barostat, as implemented in the LAMMPS code [111]. We first prepared metallic glass and nanoglass samples. To this end, we obtained the Pd₈₀Si₂₀ metallic glass by cooling a melt equilibrated at 2000 K for 2 ns, to 50 K with a cooling rate of 0.01 K/ps. The Pd₈₀Si₂₀ nanoglass is prepared by consolidating several glassy spheres, with diameter ranging from 6 nm to 8 nm, which were roughly the size of the nanoparticles prepared by inert-gas condensation [37,87].

All nanopillars have a diameter of about 36 nm and an aspect ratio (length/diameter) of 2, with the composition Pd₈₀Si₂₀ (fig. 3.8). The metallic glass and nanoglass nanopillars were produced by cutting a cylinder from the metallic glass and nanoglass replicated samples, respectively. Before deformation, each nanopillar was relaxed for 200 ps under zero pressure, in order to reach mechanical equilibrium, using an isothermal-isobaric (constant number of particles N, constant pressure P, constant temperature T) ensemble with a Nosé-Hoover thermostat at 50 K. Uniaxial compressive deformation was then simulated by applying a constant strain rate of $4 \times 10^7 \text{ s}^{-1}$ in the axial direction of the nanopillar at the same temperature. Periodic boundary conditions were applied along the axial direction of the nanopillar while the other two perpendicular directions were kept free to mimic free surfaces.

*All MD simulations are performed in collaboration with Dr. Omar Adjaoud in the group of Prof. Karsten Albe in TU Darmstadt.

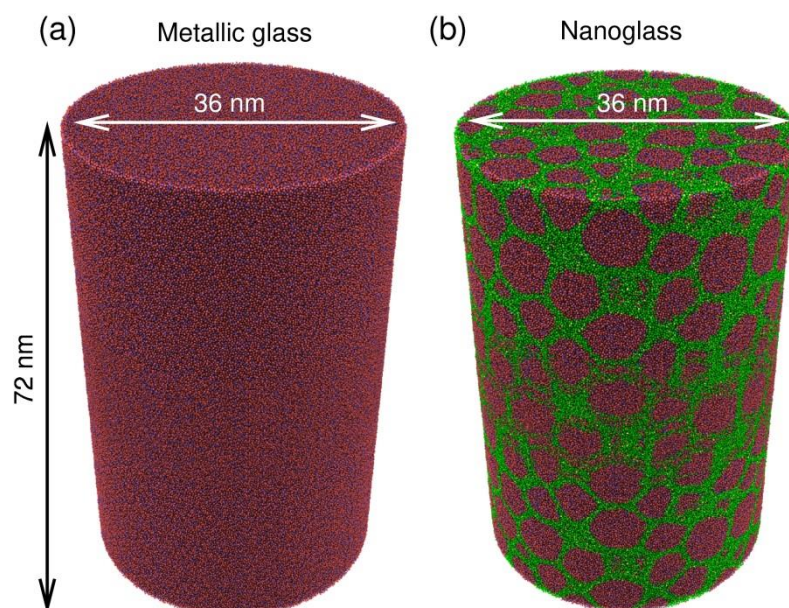


Fig. 3.8 The atomic configurations of the 36 nm diameter metallic glass and nanoglass pillars used in the simulations: (a) Metallic glass and (b) Nanoglass. Glassy grains and interfaces are shown in different colors to highlight the microstructure of nanoglass. All pillars have an aspect ratio of 2.

3.5 Materials

Till now, only few systems like Fe-Sc were successfully synthesized as nanoglasses by IGC using thermal evaporation. Since Fe and Sc are both highly oxygen sensitive, one has to take extreme precautions while synthesizing and transferring the sample. Although systems like Pd-Fe-Si, Au-Si, Au-La, Fe-Si, La-Si, Ni-Ti, Ni-Zr and Ti-P had been synthesized previously, it is difficult to reproduce the synthesis because of the difference in vapour pressure of elements and nanocrystalline phases, which can form during synthesis. So, magnetron sputtering is adopted in the current experiments to avoid the problem of difference in vapour pressures among elements. Due to the complexity of the synthesis procedure and the analysis, only binary systems are studied in the present work. $\text{Cu}_{50}\text{Zr}_{50}$, $\text{Cu}_{60}\text{Zr}_{40}$ and $\text{Pd}_{80}\text{Si}_{20}$ were chosen for the present study. Among the binary metallic glasses, Cu-Zr and Pd-Si have very good glass forming ability since few groups were successful in making them in the bulk form [15,115–121]. Also, Cu-Zr has a wide glass forming range (Cu, 35-70 at.%) and Pd-Si has a glass forming range from $\text{Pd}_{79}\text{Si}_{21}$ to $\text{Pd}_{85}\text{Si}_{15}$ which makes it possible to test different compositions in the glass forming range [122,123].

The second reason for choosing them is because it is possible to perform MD simulations on Cu-Zr and Pd-Si alloys since inter-atomic potentials for these two systems are available. Combining experimental results and MD simulations, one can study the influence of atomic structure of the interfaces on the mechanical properties. Also, the effect of oxygen on the physical properties cannot be underestimated in such nanoparticle systems. The problem of oxidation can also be largely avoided by studying Cu-Zr and Pd-Si alloys since they are not as sensitive to oxygen as Fe-Sc alloys.



4. Optimization of process variables in inert gas condensation

There are several variables in the inert gas condensation process like power of the sputtering source, type of inert gas, working pressure in the chamber, flow of inert gas in the chamber, composition of sputtering material, which can influence the yield of the process as well as the possible phases. Some preliminary experiments were carried out on Cu, Ni₅₀Ti₄₅Cu₅ and Cu₅₀Zr₅₀ alloy targets to optimize the processing conditions. The processing conditions were optimized during the initial stages with Cu and Ni₅₀Ti₄₅Cu₅ to obtain a high yield of the material.

4.1 Influence of gas pressure

Thin film deposition by conventional magnetron sputtering is performed at a pressure of 10^{-2} - 10^{-3} mbar. At such a low pressure, sputtered atoms have a large mean free path in the order of centimeters, which can deposit on the substrate with relatively less number of collisions and form films. Here, in IGC, sputtering process is performed at a pressure in the order of 10^{-1} mbar. The mean free path of a sputtered atom would be in the order of a few microns or less at such high pressures, resulting in several collisions between metal and gas atoms leading to formation of clusters/nanoparticles. The downside of so many collisions is that atoms lose their energy quickly and re-deposit back onto the target as shown in fig. 4.1 [96]. This re-deposition is mostly on the centre of the target and on the edge of the race track. Such a re-deposition drastically reduces the yield of the sputtering process. Even in the order of 10^{-1} mbar, when the inert gas pressure in the chamber is increased from 0.2 to 0.95 mbar, the yield of the condensation process decreased from a few tens of milligrams to almost no powder after 30 minutes of deposition. At a pressure of 0.95 mbar, which is almost an order of magnitude higher, re-deposition on the metal target dominates the whole sputtering process and very little yield is obtained. Sputtering plasma is also not very stable at a pressure of 0.95 mbar. Therefore, we used low pressure close to 0.3 mbar where the plasma is stable, powder can be obtained and the yield of the condensation process is sufficient enough to make a dense pellet. The size of the particle also depends on the pressure in the IGC chamber [95]. Unlike the thermal evaporation, where the pressure can be varied between 0.2-20 mbar to change the particle size, one cannot vary the pressure in sputtering process significantly as the plasma is not stable for pressures greater than 1 mbar and the yield of the sputtering process drops rapidly with increase in gas pressure.

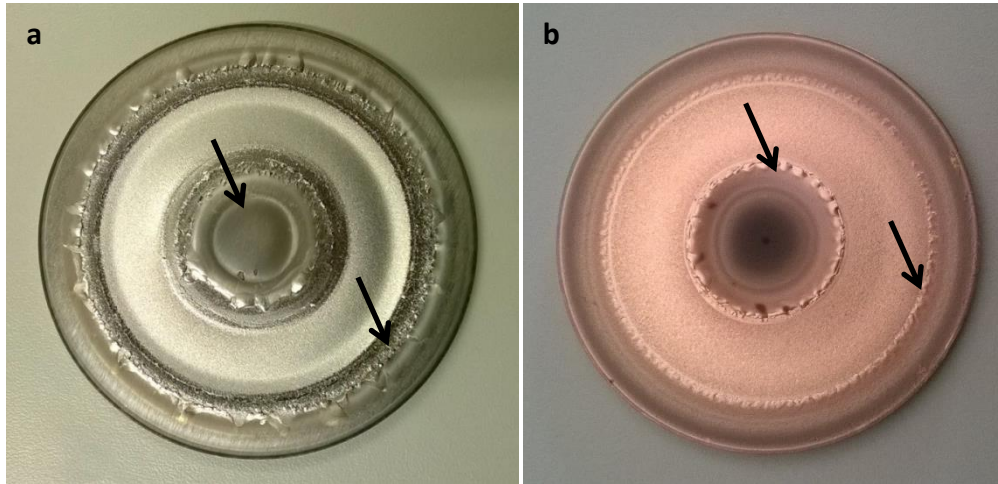


Fig. 4.1 (a) $\text{Ni}_{50}\text{Ti}_{45}\text{Cu}_5$ and (b) Cu targets after sputtering. Re-deposited zones are indicated by arrows

4.2 Influence of sputtering power

The power that can be employed during the sputtering process depends on the gas and metal ions produced in the sputtering process because it depends on the current generated by the plasma. Experiments were conducted with powers of 100, 300 and 420 W using a $\text{Cu}_{50}\text{Zr}_{50}$ metal target. Almost no powder is obtained at 100 and 300 W of sputtering power while at 420 W, 15-20 mg of powder is obtained after 15 minutes. The maximum power that can be employed with the power supply (Advanced Energy supplies, MDX 1.5K, 750V, 2A) is 420 W, which is limited by the current generated in the power supply. Higher powers lead to higher currents because more ions are generated in the sputtering process and consequently more nano powder can be obtained. So, power of 420 W is used in all the experiments.

4.3 Influence of gas flow

Here the gas flow is from the side of the target towards the cold finger, which is pumped out downstream exactly on the diametrically opposite end (see fig. 3.1). This way the efficiency of the process is also higher so that more particles are collected on the cold finger. Only few experiments were carried out to test the effect of gas flow and it was found that by having a gas flow, the yield of the process was improved considerably almost by 30-50%, especially for NiTiCu alloy target.

4.4 Influence of type of inert gas and He/Ar ratio

It is already well known that sputtering is more efficient with Ar gas compared to He since Ar is heavier than He. When the He/Ar mass flow ratio was changed from 0.2 to 0.5, it was found that the increase in the proportion of He decreased the yield of the process. One

experiment was carried out with only Ar gas. Unlike all the other experiments, this one was performed with no gas flow. No powder was obtained while tens of milligrams of powder was obtained in other experiments when a mixture of Ar and He were used, even when there was no gas flow in 30 minutes of sputtering. The primary reason for such a change in the yield with He/Ar ratio can be explained in the following way. By using only He, the sputtering efficiency is less and so the amount of powder obtained is also very low whereas using only Ar increases the sputtering efficiency as well as the re-deposition of atoms, which reduces the total yield of the process. So, a mixture of Ar and He gases with the ratio of 0.2 has been used to increase the yield of the process for all the subsequent experiments.

4.5 Influence of alloy materials

The yield of the process also depends on the alloy materials used. A good yield of approximately 130 mg in 1 h can be obtained by using pure crystalline Cu while the yield is reduced to ~40 mg in 1 h for Ni₅₀Ti₄₅Cu₅ alloy. For Cu₅₀Zr₅₀ alloy, the yield is roughly 50-60 mg in 1 h while ~100 mg is obtained in 1 h for Pd₈₀Si₂₀ alloy. The yields are approximate values from a series of experiments, which are not done exactly for 1 h but rather interpolated or extrapolated to 1 h. The efficiency of the sputtering process depends on the binding energy of the target material.

The effect of all processing parameters on the yield of powder is summarized in table 4.1. Finally to conclude, although the entire optimization of sputtering parameters is based on increasing the yield of the process, the phases obtained and the composition of the final powder may slightly vary with different alloy materials. Preferential sputtering of one of the elements is observed in few alloy targets. In Ni₅₀Ti₄₅Cu₅, the final composition of the alloy powder was Ni₄₄Ti₃₃Cu₂₃. There is a reduction in Ti content and an increase in Cu content in the final powder. This is also observed in Pd₈₀Si₂₀ alloy system with slightly higher Pd content in the final powder composition (Pd₈₄Si₁₆). A list of materials produced using this method till now is presented in table 4.2. As a word of caution, if one wants to make a glassy composition in IGC by using sputtering, one has to take care that the final composition of the alloy powder is in the glass forming range.

Table 4.1 Effect of the process parameters on the yield of the powder

Parameter (increasing)	Effect on the yield
Gas pressure	decreases
Sputtering power	increases
Gas flow	increases
He/Ar ratio	optimum ratio is required
Alloy materials	depends on the material

Table 4.2 Alloy targets and the final composition of powder

Target (alloys)	Final composition
Ni ₅₀ Ti ₄₅ Cu ₅	Ni ₄₄ Ti ₃₃ Cu ₂₃
Cu ₅₀ Zr ₅₀	Cu ₅₀ Zr ₅₀
Cu ₆₀ Zr ₄₀	Cu ₆₀ Zr ₄₀
Pd ₈₀ Si ₂₀	Pd ₈₄ Si ₁₆
Gd ₇₅ Fe ₂₅	Gd ₇₇ Fe ₂₃ *
Ni ₅₀ Ti ₅₀	Ni ₅₀ Ti ₅₀ *

*not presented in this thesis

5. Atomic structure and properties of Cu-Zr nanoglasses synthesized by IGC

A major portion of this chapter was already published in [124].

In this chapter, structure and mechanical properties of $\text{Cu}_{50}\text{Zr}_{50}$ and $\text{Cu}_{60}\text{Zr}_{40}$ nanoglasses are described in detail. Thermal characterization is performed by DSC on the nanoglass and reference melt-spun ribbon samples. Micro- and nanoindentation techniques are used to test their deformation behaviour. Detailed explanation for the observed thermal properties and deformation behaviour is described in this chapter.

5.1 Experimental details

$\text{Cu}_{50}\text{Zr}_{50}$ and $\text{Cu}_{60}\text{Zr}_{40}$ metallic nanoglasses were prepared by using magnetron sputtering in an IGC system. The composition of the as-prepared nanoglass samples was determined by EDS in SEM. Density measurements of nanoglasses and melt-spun ribbons were carried out by a newly developed method using laser confocal microscope as described in section 3.2.6. Annealing of the nanoglass samples was carried out in ultrahigh vacuum (1×10^{-8} mbar) at 350°C ($\sim 0.9T_g$ of melt-spun ribbon) for 3, 12 and 24 h with small specimens from the initial compacted pellet. Differential scanning calorimetry (DSC) was carried out using a Netzsch DSC under high purity Ar gas flow of 100 sccm. Hardness measurements were carried out after polishing the samples with standard metallographic techniques. The polished surface of the nanoglass specimens and the shiny side of the melt-spun ribbons are used for hardness testing. A constant load of 100 gf was applied on a melt-spun ribbon in order to ensure that the depth of the indentation does not exceed 10% of the sample thickness. 100 and 1000 gf loads were applied on the nanoglass and the annealed samples. Microhardness values presented are an average of 10 indentations. Nanoindentation measurements were performed in the continuous stiffness measurement (CSM) mode at three different indentation strain rates (0.01, 0.05, and 0.1 s^{-1}) to a maximum depth of 500 nm on polished samples. Five indentations were done at each strain rate for both the melt-spun and nanoglass samples. Nine indentations were done on the annealed nanoglass sample. Focused ion beam (FIB) milling of melt-spun ribbon and nanoglass samples were done by FEI Strata 400 STEM using Ga ions to make pillars of micron size. The details of pillar preparation were already mentioned section 3.2.7. Micropillar testing was carried out using Insem (Nanomechanics Inc.) machine with a flat indenter of $5 \mu\text{m}$ in diameter. Correction for the compliance of the substrate is performed by using Sneddon's equation. The elastic modulus of the nanoglass sample is taken from the nanoindentation data to perform the correction.

5.2 Structural characterization of nanoglasses

The amorphous nature of as-prepared and annealed samples is confirmed by X-ray diffraction (see fig. 5.1). No crystalline diffraction peaks are observed in any of the samples. Even after annealing the sample for 24 h at $0.9 T_g$, the amorphous nature of the samples is still retained. Some of the samples are polished before the XRD measurement to remove any oxide layers on top of them. There is a possibility of presence of some nanocrystallinity in the sample, which cannot be detected by XRD. To verify this, TEM is carried out on the as prepared nanoglass and also on the melt-spun ribbons. TEM images confirm the amorphous nature of the $\text{Cu}_{50}\text{Zr}_{50}$ nanoparticles with diameters in the range of 4-10 nm as shown in fig. 5.2(a). It must be pointed out that although most of the powder is amorphous in nature; few oxidized powder particles were observed since the nanoparticles are exposed to air during the transfer to TEM. Crystallization of a few nanoparticles is also observed under the electron beam in the microscope. Such problems of oxidation and crystallization under beam can be avoided in the nanoglass sample since the sample is consolidated under ultra high vacuum conditions. As seen in fig. 5.2(b), the amorphous nature is still retained after high pressure compaction and the selected area electron diffraction (SAED) clearly shows a diffused halo without crystalline spots or rings. The amorphous structure of nanoglasses can also be evidenced using HRTEM (fig. 5.2(c)).

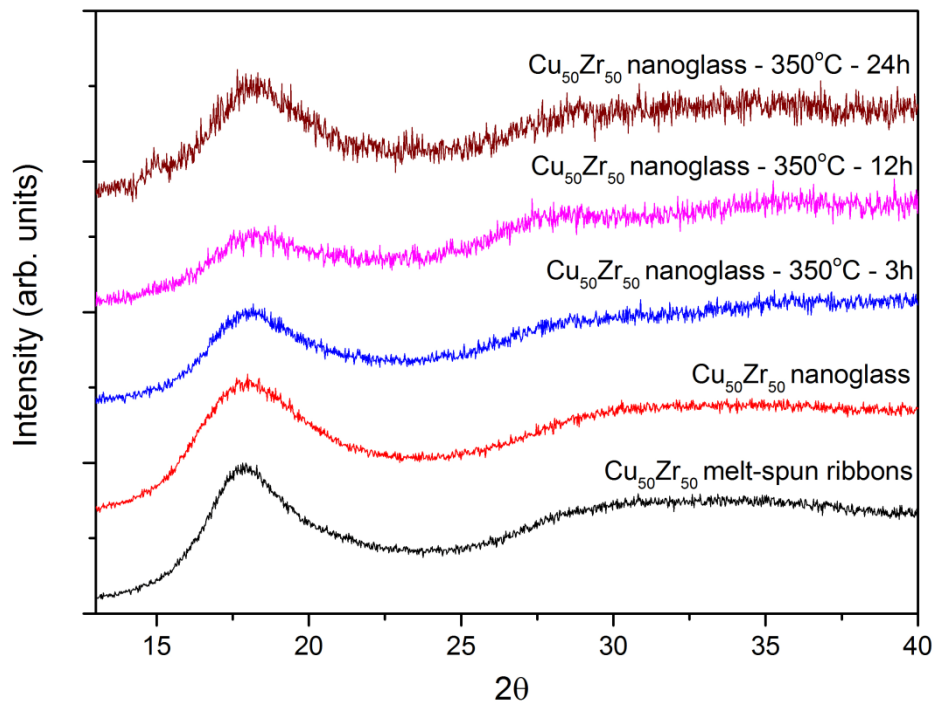


Fig. 5.1 XRD of the $\text{Cu}_{50}\text{Zr}_{50}$ and $\text{Cu}_{60}\text{Zr}_{40}$ melt-spun ribbons and nanoglass samples. XRD patterns of $\text{Cu}_{50}\text{Zr}_{50}$ annealed nanoglass samples are also shown.

EDS analysis in the SEM showed the composition of the nanoglass samples was around $\text{Cu}_{50}\text{Zr}_{50}$ with a variation of $\sim 1\%$ on both sides of the pellet. At least three scans were recorded to determine the compositional homogeneity. A typical secondary electron (SE)

image and the corresponding EDS spectrum of a $\text{Cu}_{50}\text{Zr}_{50}$ nanoglass is shown in fig. 5.3(a) & (b). A small oxygen signal is also observed in the EDS spectrum (see fig. 5.3(b)). Since the nanoparticles are prone to oxidation, it is important to test the oxygen content in the sample. The oxygen content in the as-prepared nanoglass samples was found to be approximately 2 at.% as measured by carrier gas hot extraction method. For comparison, melt-spun ribbons were also tested for their oxygen content by the same method and it was found to be around 1 at.%. In an unpolished nanoglass, residual porosity remains on the top surface of the sample because of incomplete consolidation which is always prone to oxidation.

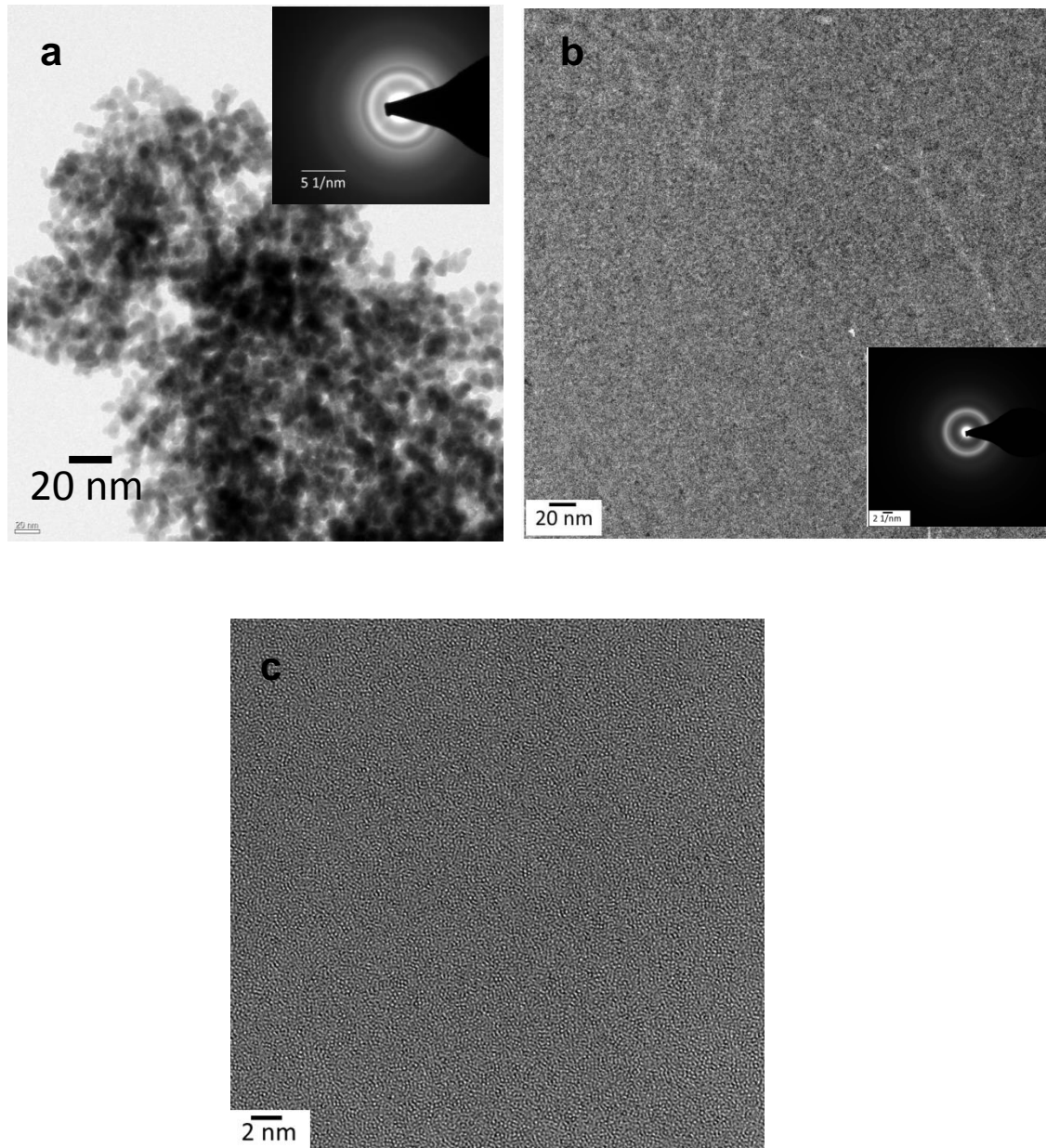


Fig. 5.2 TEM images of (a) $\text{Cu}_{50}\text{Zr}_{50}$ amorphous powder scraped from the cold finger, inset showing the SAED confirming the amorphous nature of the sample (b) bright-field image of nanoglass showing amorphous nature, which was confirmed by the diffraction pattern (inset). (c) HRTEM image of the nanoglass showing the amorphous contrast with no crystalline patterns

A densely compacted sample is essential to perform mechanical tests with good reproducibility in any powder compacted specimens. To this end, all the nanoglass samples were cold compacted at a very high pressure of about 6 GPa. The density of the melt-spun ribbon is measured to be 7.33 g/cm^3 , which is in the range of the theoretical and experimental values reported in the literature for $\text{Cu}_{50}\text{Zr}_{50}$ melt-spun ribbons [4,64]. The relative density of the nanoglass samples is calculated assuming the density of the melt-spun ribbons as the theoretical density and it is found to be around 92% for the as-prepared sample.

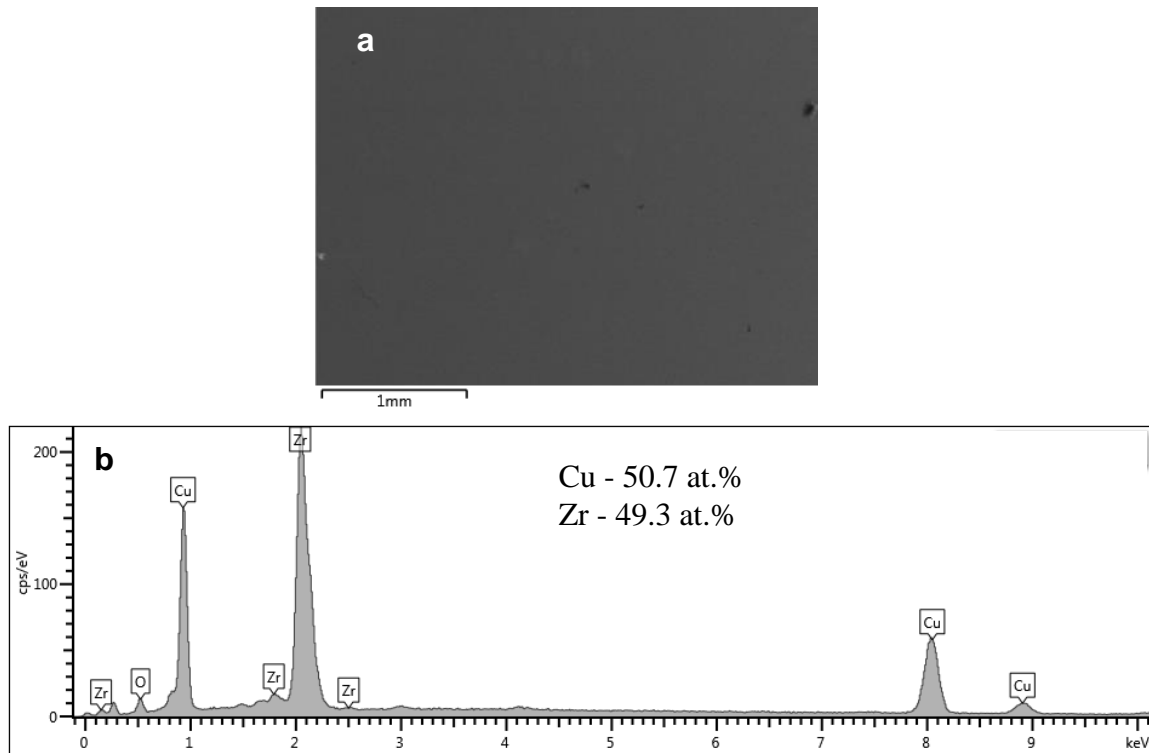


Fig. 5.3 (a) Secondary electron image of a $\text{Cu}_{50}\text{Zr}_{50}$ nanoglass and (b) EDS spectrum taken from the fig. (a). Composition of the sample obtained from the EDS spectrum is also mentioned in the fig. (b)

Another important feature of the nanoglasses is the elemental segregation of individual constituents, which was already reported in Fe-Sc nanoglasses [38,43,86]. To characterize the segregation behaviour, APT is performed on $\text{Cu}_{50}\text{Zr}_{50}$ nanoglass and melt-spun ribbon samples. Fig. 5.4(a) shows the 3D reconstruction of the $\text{Cu}_{50}\text{Zr}_{50}$ nanoglass. The position and the nature of each detected individual atom are represented by color-coded dots (Zr in blue and Cu in red) within the reconstructed volume. Composition maps of a thin slice in fig. 5.4(b) clearly show the segregation to form Cu and Zr rich regions on the length scale of 5-6 nm, which corresponds roughly to the average size of the primary nanoparticles. One should realize that the composition maps are only a 2D projection of a very thin slice of 3DAP. It is not a case of individual particles being completely Zr rich or Cu rich since no such particles were observed in 3D atom probe images.

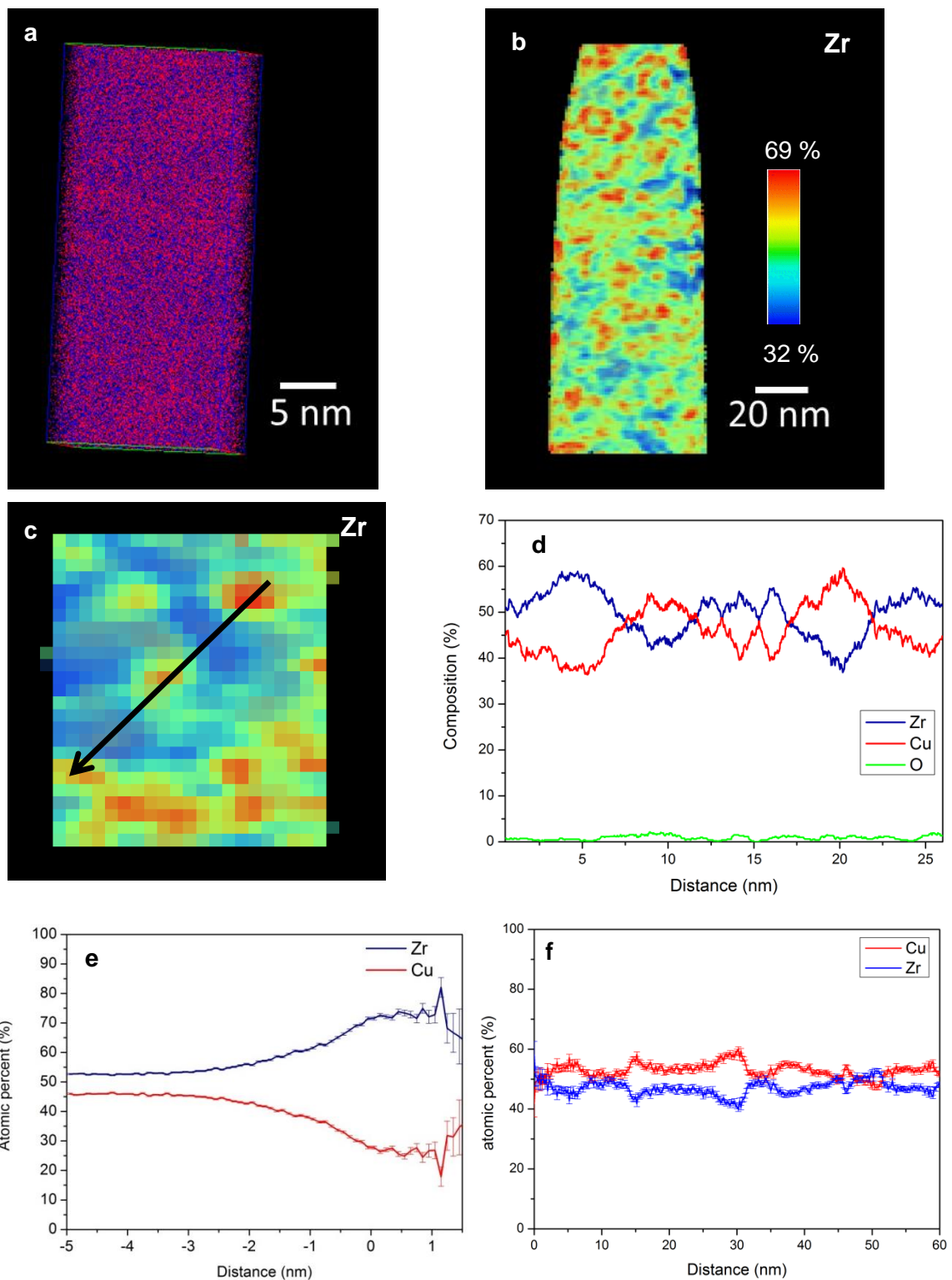


Fig. 5.4 (a) 3DAP tomography image of a tip prepared from a nanoglass sample (Zr atoms in blue and Cu atoms in red) (b) Heat map of Zr showing the segregation of Zr in the range of 5-6 nm (c) Heat map of Zr at a magnified scale (d) Composition map of Cu and Zr along the arrow shown in the (c), (e) Proxigram on a 65 at.% Zr iso-surface showing the compositional variation and (f) composition profile along a cylinder of 3DAP in $\text{Cu}_{50}\text{Zr}_{50}$ melt-spun ribbon

A region of interest is chosen to show the segregation on a magnified scale (see fig. 5.4(c)) from which a concentration profile (fig. 5.4(d)) of Cu and Zr along the cylinder (marked with an arrow in fig. 5.4(c)) is deduced and clearly shows the compositional fluctuations. The average composition of Cu fluctuates between 36 and 60 at.% whereas the composition of Zr fluctuates between 37 and 59 at.%. These values depend on the diameter of the selected cylindrical volume for analysis. Alternatively, one can look at the proxigram through the iso-surface for 65 at.% Zr, which shows that the core of the Zr-rich regions can contain up to 70 at.% Zr (fig. 5.4(e)). An oxygen content of roughly 1-2 at.% is found by atom probe analysis as can be seen from fig. 5.4(d) in agreement with that measured by carrier gas hot extraction method. For comparison, a typical composition profile along a cylinder in a Cu₅₀Zr₅₀ melt-spun ribbon is shown in fig. 5.4(f). As can be seen from the figure, no discernable segregation at nanoscale is found in the melt-spun ribbon samples. The composition of Cu fluctuates between 47 to 58 at.% while Zr fluctuates between 42 to 53 at.% in melt-spun ribbons. Comparing fig. 5.4(d) and (f), one can clearly observe the fluctuation difference in the nanoglass samples while it is not so prominent in melt-spun ribbons.

Table 5.1 Glass transition (T_g), onset of crystallization (T_x) and peak (T_p) temperature, Hardness by Vickers and nanoindentation (strain rate of 0.05 s^{-1}), Young's modulus of as-prepared nanoglass, annealed nanoglass and melt-spun ribbons

	T_g (°C)	T_x (°C)	T_p (°C)	ΔH_x (J/g)	Hardness (by nanoindentation) (GPa)	Young's modulus (by nanoindentation) (GPa)	Hardness (HV 0.1)
Cu ₅₀ Zr ₅₀ nanoglass	-	457	469	31	7.40 ± 0.20	104.8 ± 1.8	390 ± 26
Cu ₅₀ Zr ₅₀ nanoglass - 350°C - 3h	-	462	474	32	7.17 ± 0.54	104.5 ± 4.9	469 ± 30
Cu ₅₀ Zr ₅₀ nanoglass - 350°C - 12h	-	434	471	-	-	-	-
Cu ₅₀ Zr ₅₀ nanoglass - 350°C - 24h	-	436	467	-	-	-	-
Cu ₅₀ Zr ₅₀ melt-spun ribbon	410	449	455	55	6.70 ± 0.13	93.9 ± 1.0	340 ± 19
Cu ₆₀ Zr ₄₀ nanoglass	-	500	521	40	-	-	491 ± 31
Cu ₆₀ Zr ₄₀ melt-spun ribbon	440	475	481	53	-	-	464 ± 18

5.3 Thermal stability

Till date, only $\text{Sc}_{75}\text{Fe}_{25}$ nanoglass samples have been tested in respect of their thermal stability in DSC (see SI in ref. [29]). Due to the problems of oxidation, it is difficult to characterize glass transition (T_g), onset of crystallization (T_x) of the samples. Here, we will discuss in detail the thermal behaviour of $\text{Cu}_{50}\text{Zr}_{50}$ metallic nanoglasses and melt-spun ribbons characterized by using DSC to determine the glass transition and crystallization temperature.

DSC thermograms of $\text{Cu}_{50}\text{Zr}_{50}$ specimens at a heating rate of $20\text{ }^\circ\text{C}/\text{min}$ are shown in fig. 5.5. The glass transition (T_g), onset of crystallization (T_x) and peak (T_p) temperature for all the samples are summarized in table 5.1. The results were confirmed with a second DSC machine (Netzsch HP) on different samples and it was found that a variation in the temperature values is less than $2\text{ }^\circ\text{C}$. In both the measurements, the crystallization peak is smaller and broader in the case of Cu-Zr nanoglass samples compared to melt-spun ribbons. T_g in melt-spun ribbons is clearly evident from the DSC thermograms as indicated by the arrow in fig. 5.5. It is not as pronounced in nanoglasses when compared to melt-spun ribbons. The T_g and T_x in the melt-spun ribbon is close to the reported value in literature [4]. A slight increase of T_x and T_p is observed in $\text{Cu}_{50}\text{Zr}_{50}$ nanoglass compared to the melt-spun ribbons. To know the effect of heat treatment on the segregation behaviour, $\text{Cu}_{50}\text{Zr}_{50}$ nanoglasses were annealed at $0.9 T_g$ for different times. It was observed that T_x and T_p shifted to a slightly higher temperature after annealing the nanoglass for 3 h but they decreased to almost the same temperature as melt-spun ribbon after annealing for 12 and 24 h in $\text{Cu}_{50}\text{Zr}_{50}$ nanoglasses. The enthalpy of crystallization (ΔH_x) for $\text{Cu}_{50}\text{Zr}_{50}$ melt-spun ribbon, nanoglass, annealed nanoglass for 3, 12 and 24 h is 55, 31, 32, 23 and 22 J/g respectively. ΔH_x of nanoglass is less compared to melt-spun ribbon whereas a nanoglass annealed for 3h showed similar enthalpy to an as prepared nanoglass. Prolonged annealing of the nanoglass for long periods shows decrease in enthalpy of crystallization reaction.

As mentioned before, the effect of oxygen on the thermal properties should not be underestimated in such nanoparticulate systems. To find out whether the thermal properties are influenced by oxygen, the nanoglass samples were crystallized partially and completely to study the phase formation during the crystallization reaction. One $\text{Cu}_{50}\text{Zr}_{50}$ nanoglass and melt-spun ribbon sample was completely crystallized in a DSC by heating up to $595\text{ }^\circ\text{C}$. XRD of the completely crystallized sample showed CuZr_2 and $\text{Cu}_{10}\text{Zr}_7$ as shown in fig. 5.6(a), which are the equilibrium phases according to the Cu-Zr phase diagram [125,126]. One nanoglass sample was partially crystallized in a DSC by heating up to $460\text{ }^\circ\text{C}$ (which is roughly midway between the onset of crystallization and peak temperature in DSC) and was then observed in TEM. As shown in fig. 5.6(b), fine crystallites of the order of 5-10 nm were observed. Selected area electron diffraction (fig. 5.6(c)) from the region showed two faint crystalline rings. The rings correspond to the crystalline phase Cu_5Zr . The reason for the precipitation of a Cu-rich phase like Cu_5Zr can be understood in terms of elemental segregation in the sample. Since Cu and Zr rich regions are present in the nanoglasses, it is

plausible that phases like Cu_5Zr precipitate initially, which later transform into equilibrium phases upon further increase in temperature. Although few regions containing oxygen were observed in the partially crystallized sample, no preferential segregation to Cu or Zr is seen.

The precipitation sequence of $\text{Cu}_{50}\text{Zr}_{50}$ metallic glass was already studied in detail by Cullinan *et al.* [125] after an isothermal treatment at 398°C , and it was found that the precipitation sequence involves the initial formation of $\text{Cu}_{10}\text{Zr}_7$, CuZr_2 and CuZr (B2) phases, which finally become equilibrium $\text{Cu}_{10}\text{Zr}_7$ and CuZr_2 over further heating in DSC. Similar results were also obtained by Kalay *et al.* [126] in isochronal heat treatment conditions. However, here in the partially crystallized nanoglass samples, Cu_5Zr phase is observed, which is different from what was observed by Cullinan *et al.* [125] and Kalay *et al.* [126]. Upon complete crystallization of the nanoglass samples, $\text{Cu}_{10}\text{Zr}_7$ and CuZr_2 phases have been obtained which are the final equilibrium phases (see fig. 5.6(a)).

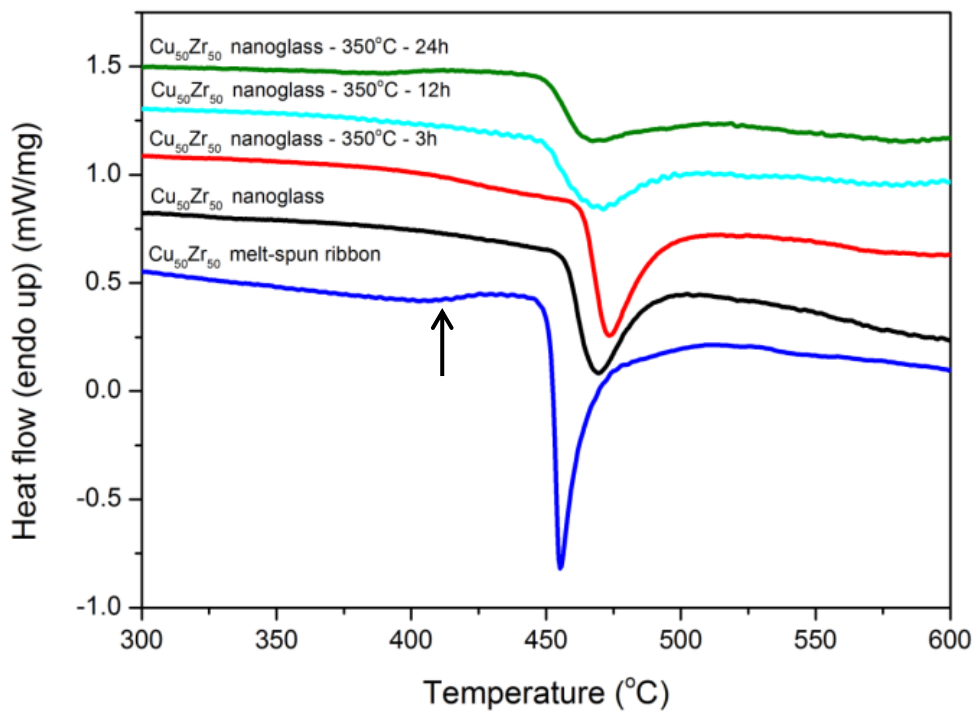


Fig. 5.5 DSC of $\text{Cu}_{50}\text{Zr}_{50}$ melt-spun ribbon, nanoglass and the annealed nanoglass for different times showing the glass transition and crystallization temperature. Crystallization temperature of the nanoglass is higher than that of the melt-spun ribbon. Curves are shifted along the Y-axis (heat flow) for clarity. Arrow indicates T_g of melt-spun ribbons.

Two factors could influence the observed increase in T_g , T_x and the reduction in enthalpy. One is the basic structure of the nanoglass and the other is the oxygen content in the sample. Let us discuss the effect of oxygen on the crystallization behaviour. It was already observed that by the addition of 0.43 wt.% (2 at.%) oxygen into $\text{Cu}_{50}\text{Zr}_{50}$ amorphous system, a shoulder started appearing in the crystallization peak of the DSC curve [127]. The addition of oxygen also shifted the crystallization peak to slightly higher temperature. However, no change in the enthalpy of the crystallization reaction was observed with the addition of

oxygen into $\text{Cu}_{50}\text{Zr}_{50}$ melt-spun ribbons. The final phases observed after complete crystallization with the addition of 0.43 wt.% (2 at.%) oxygen are still equilibrium CuZr_2 and $\text{Cu}_{10}\text{Zr}_7$ phases [127]. However, the sequence of crystallization with the addition of oxygen is not investigated in ref. [127]. In the nanoglass samples, the measured oxygen content is roughly around 2 at.%, which is similar to the amount of oxygen added in ref. [127]. However, no discernable shoulder is observed in the DSC heating trace of the nanoglass sample as shown in fig. 5.5 and also the crystallization peak showed a substantial reduction in enthalpy, which is not observed in ref. [127]. So, we can safely assume that although oxygen can affect the crystallization behaviour, it may not be substantial in $\text{Cu}_{50}\text{Zr}_{50}$ nanoglasses. Hence, we can conclude that the thermal properties observed in DSC are a result of the basic microstructure of the nanoglass, which will be discussed in detail in section 5.5. Due to the complexity of the crystallization reaction because of the nanocrystalline phases and the structural disorder, a detailed study on the evolution of the crystalline phases during the crystallization reaction is out of the scope of current work.

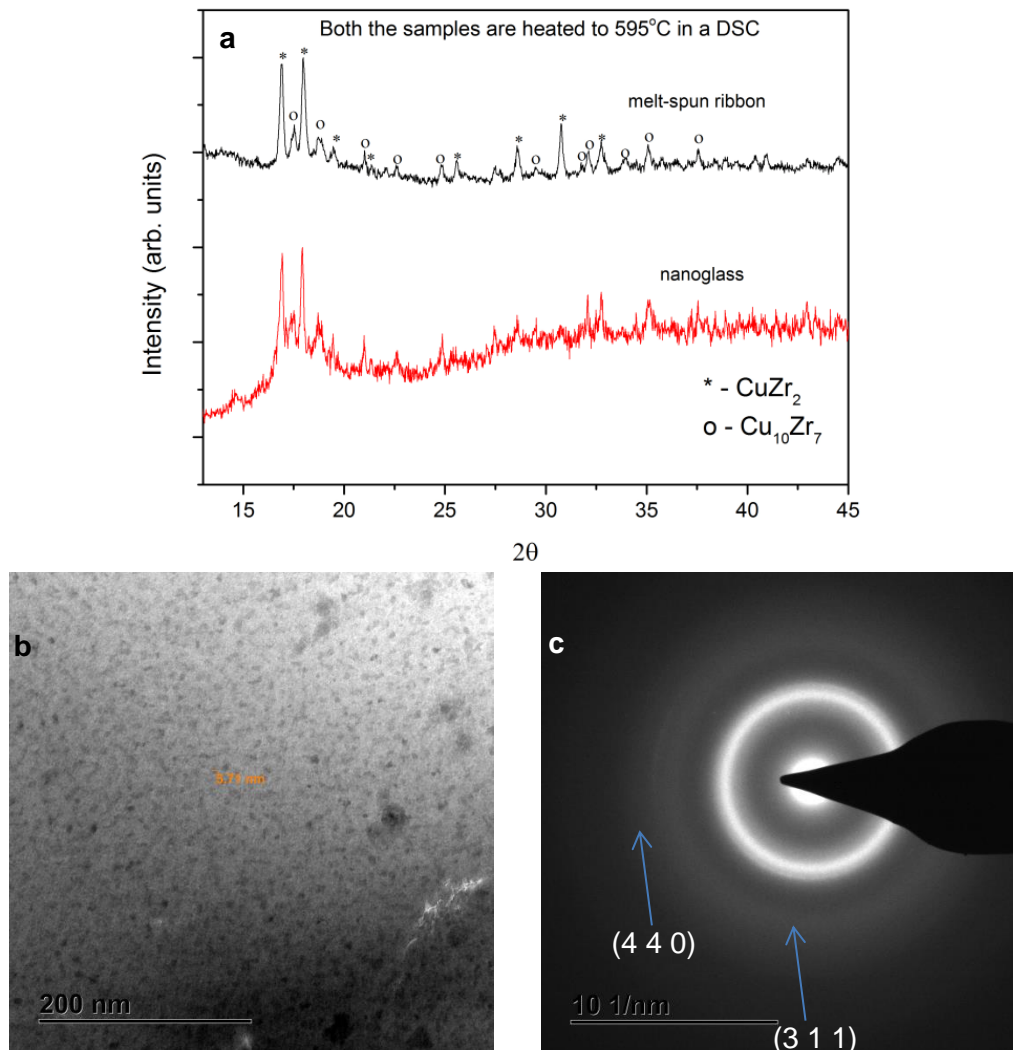


Fig. 5.6 (a) XRD of completely crystallized nanoglass and melt-spun ribbon sample, (b) TEM of nanoglass sample heated upto 460 °C in a DSC. Fine crystals in the size range of 5-10 nm can be seen. (c) SAED pattern of the region showing faint crystalline rings.

To study further on the thermal behaviour, $\text{Cu}_{50}\text{Zr}_{50}$ nanoglass and melt-spun ribbon samples were heated at heating rates of 5, 10, 20 and 40 °C/min in a DSC as shown in fig. 5.7(a) & (b). Since crystallization of the reaction is a rate dependent phenomenon, non-isothermal models like Kissinger analysis can be used to calculate the activation energy involved in the process [128]. With the increase in heating rate, the peak crystallization temperature shifts to higher values, which can be exploited to calculate the activation energy involved in the process. The following is the Kissinger equation used to calculate the activation energy of the crystallization reaction:

$$\ln \frac{\beta}{T_p^2} = -\frac{E_a}{RT_p} + C \quad (5.1)$$

where β is the heating rate, T_p is the peak temperature, R is the gas constant, E_a is the activation energy in kJ/mol and C is a constant.

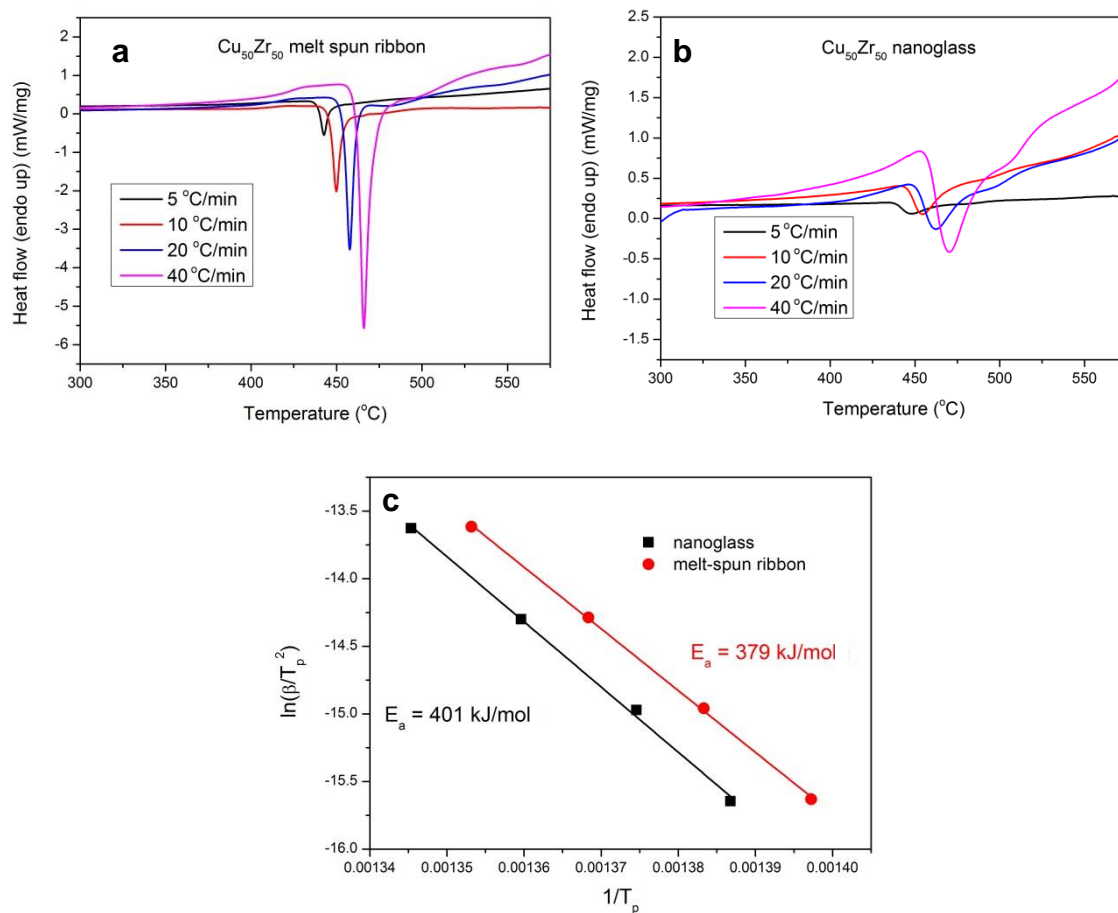


Fig. 5.7 DSC plots showing the crystallization reaction at four heating rates in $\text{Cu}_{50}\text{Zr}_{50}$ (a) melt-spun ribbon, (b) nanoglass and (c) Activation energy plot using Kissinger equation

The activation energy calculated for $\text{Cu}_{50}\text{Zr}_{50}$ nanoglass is 401 ± 12 kJ/mol while for the melt-spun ribbons, it is 379 ± 6 kJ/mol as shown in fig. 5.7(c). The values for the nanoglass samples are slightly higher compared to those for melt-spun ribbons of the same composition.

Pauly *et al.* [129] investigated the activation energy for the crystallization reaction of $\text{Cu}_{50}\text{Zr}_{50}$ melt-spun ribbons and found that the value is 438 ± 13 kJ/mol, which is higher than the value obtained for the melt-spun ribbons in the present work. Murty *et al.* [130] observed that the addition of oxygen upto 0.82 at.% into Cu-Zr metallic glasses did not cause any significant change in the crystallization enthalpy. This is an additional proof that the effect of oxygen is minimal in $\text{Cu}_{50}\text{Zr}_{50}$ nanoglasses. The final crystallization phases in both the nanoglass and melt-spun ribbon samples are the same, i.e. CuZr_2 and $\text{Cu}_{10}\text{Zr}_7$. The activation energy of $\text{Cu}_{10}\text{Zr}_7$ and CuZr_2 phase formation is 406 ± 12 kJ/mol, which is similar to the value reported here for nanoglass and melt-spun ribbon [127]. High activation energy for crystallization means that the diffusion of atoms is difficult, which indicates that the crystallization products cannot be formed easily [3,127]. Such low enthalpy in nanoglass sample also indicates that $\text{Cu}_{50}\text{Zr}_{50}$ nanoglasses are comparatively more stable than the melt-spun ribbons. Segregation of Cu and Zr rich regions is already observed in APT. So, it is possible that more long range diffusion of Cu and Zr atoms is necessary to make the final equilibrium phases of $\text{Cu}_{10}\text{Zr}_7$ and CuZr_2 in nanoglasses compared to melt-spun ribbons where Cu and Zr atoms are more uniformly distributed.

5.4 Micro- and Nanoindentation

One of the primary aims of the present work is to characterize the mechanical properties of the nanoglasses and compare them with respective properties of melt-spun ribbons. For this purpose, Vickers hardness tests are carried out on Cu-Zr metallic nanoglasses and melt-spun ribbons. Indentations on nanoglasses revealed some interesting features. Hardness value at 100 gf load of as prepared and annealed nanoglass (for 3h) is higher compared to that of melt-spun ribbon (Table 5.1). The hardness of as prepared and annealed nanoglass samples at 1000 gf load is 432 ± 8 and 506 ± 11 HV, which is higher than the values obtained at 100 gf. The more interesting feature about the indentation tests is that the areas in the vicinity of the Vickers indents (fig. 5.8(a)-(d)) in both the as prepared and annealed nanoglass clearly do not show any shear bands whereas the melt-spun ribbons show clearly shear bands around the indent. The microstructure of the specimen extracted under the indent (Vickers indent at 1000 gf) of a nanoglass was carefully inspected in order to reveal any transformation mediated ductility. It is clearly seen from fig. 5.8(e) that the region under the indent is completely amorphous with no indication of formation of any crystallites. HRTEM image clearly shows the amorphous nature as observed in fig. 5.8(f).

Nanoindentation tests were performed to understand the deformation behaviour in small regions where the influence of porosity (if any) will be significantly reduced. Representative load versus displacement curves obtained by nanoindentation of as prepared, annealed nanoglass and melt-spun ribbon at an indentation strain rate of 0.05 s^{-1} are shown in fig. 5.9. The curves of both as prepared and annealed nanoglass samples are smooth without any pop-ins (indicating homogeneous deformation), while the load vs displacement curves of the melt-spun ribbon of similar composition show clear pop-ins (serrations), indicating the

generation of shear bands (inhomogeneous deformation). Young's modulus measured at the indentation strain rate of 0.05 s^{-1} is 104.8 ± 1.8 , 104.5 ± 4.9 and 93.9 ± 1.0 GPa, for the nanoglass, annealed nanoglass and melt-spun ribbon (calculated assuming a Poisson's ratio of 0.3 for all the samples), respectively. Young's modulus of the nanoglass is slightly higher than that of the melt-spun ribbons of similar composition. Here, it must be pointed out that the samples are dense enough since the modulus and hardness values both in micro and nanoindentation are higher or almost equivalent to those of melt-spun ribbons. So, we can rule out the effect of porosity as a reason for the observed deformation behavior and conclude that the microstructure of the nanoglass itself as the major reason. Recently, evidence for the densification of a metallic glass is presented for a Zr-based alloy by Wang *et al.*[71]. In the annealed nanoglasses, no shear bands are observed around the indents even after annealing for sufficiently long time (fig. 5.8(b)) indicating that the interfaces are in a stable state. Although as a preliminary approximation, we can say that the densification does not significantly affect the deformation behavior, a more detailed analysis has to be carried out to conclusively determine this observation.

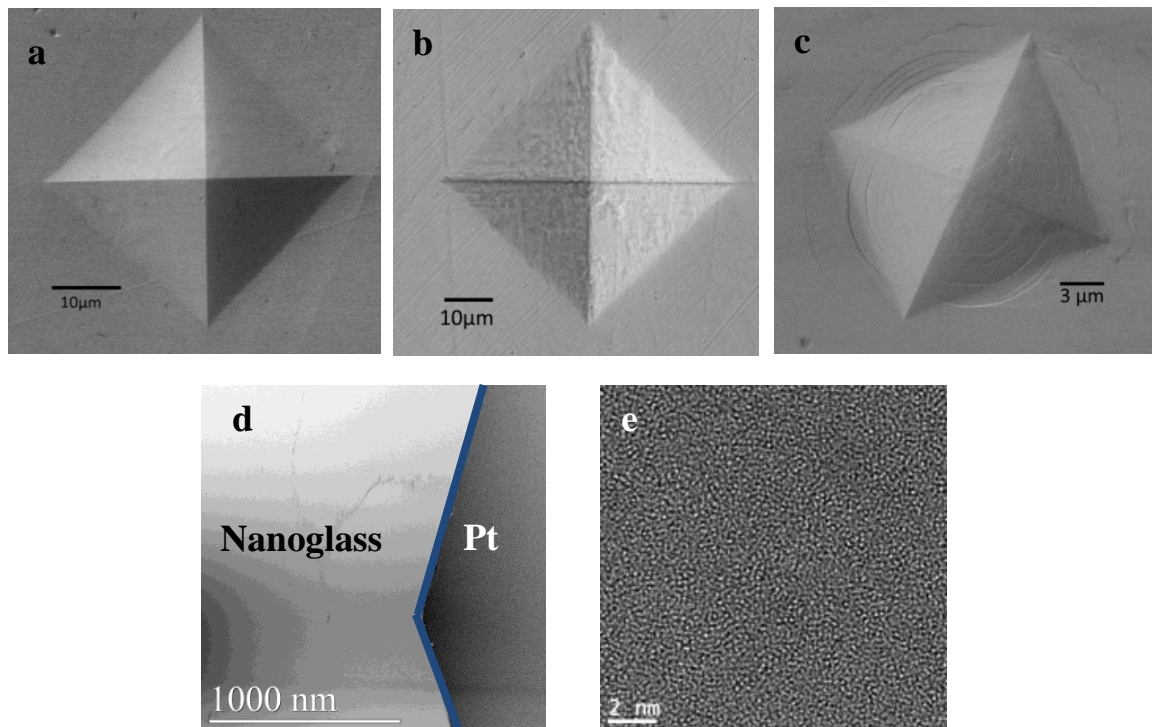


Fig. 5.8 Scanning electron micrographs of indents in (a) $\text{Cu}_{50}\text{Zr}_{50}$ as-prepared nanoglass, (b) $\text{Cu}_{50}\text{Zr}_{50}$ annealed nanoglass, neither of them showing shear bands around the indent (c) $\text{Cu}_{50}\text{Zr}_{50}$ melt-spun ribbon with clear shear bands around the indent (d) STEM image showing no crystallization below the indent. Pt deposited during FIB is the dark region on the right hand side of the image. The line indicates the partition between Pt and the nanoglass and (e) HRTEM of the nanoglass region confirming the amorphous nature.

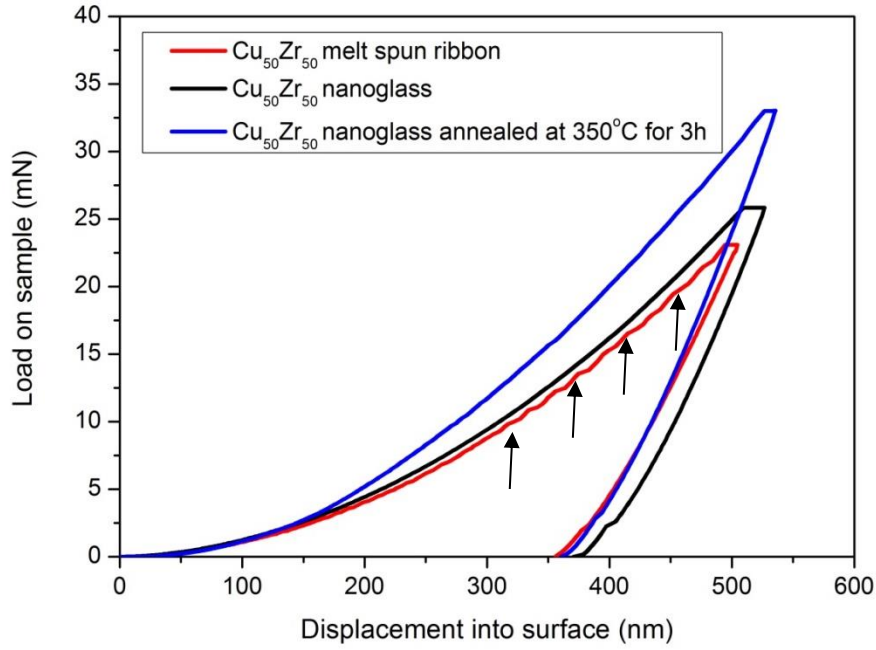


Fig. 5.9 Representative nano indentation curves of melt-spun ribbon, as-prepared nanoglass and annealed nanoglass at an indentation strain rate of 0.05 s^{-1} . No pop-ins were observed in the nanoglass samples while they were observed in melt-spun ribbons (indicated by arrows).

5.5 Volume of STZ

Recently, Pan *et al.* [131] have proposed a model to calculate the STZ volume by using nanoindentation. The model to calculate the volume of the STZ is based on the cooperative shear model proposed by Johnson and Samwer [132]. By calculating the STZ volume, it was observed that the size of the plastic zone or STZ increases with the increase in ductility of the metallic glass. According to this model, the volume of the STZ is calculated from indentation experiments performed at different strain rates using the following equation

$$\Omega = \frac{kT}{C' mH}$$

where Ω is the STZ volume, k is the Boltzmann constant, T is the temperature at which the experiments are performed (in the present case, room temperature), m is the strain rate sensitivity, H is the hardness and $C' = \frac{2R\zeta}{\sqrt{3}} \frac{G_0\gamma_c^2}{\Gamma_c} (1 - \frac{\Gamma_{cT}}{\Gamma_c})$ in which R and ζ are universal constants with values of $R \approx 1/4$, $\zeta \approx 3$, $\Gamma_c/G_0 \approx 0.036$, $\gamma_c = 0.0267$ is the average elastic limit, Γ_c is the threshold shear resistance of an alloy at 0 K and Γ_{cT} is the critical shear resistance at temperature T . The value of Γ_{cT}/Γ_c can be approximately calculated based on the formula $(\Gamma_{cT}/\Gamma_c) = 1 - ((0.016/0.036) (T/T_g)^{2/3})$ [24].

In order to determine the strain rate sensitivity, nanoindentation experiments were performed at three different indentation strain rates, i.e. 0.01 , 0.05 and 0.1 s^{-1} , for the nanoglass and the melt-spun ribbons as shown in fig. 5.10(a) and (b). The strain rate sensitivity of the nanoglass

and melt-spun ribbon can be estimated from the slope of the log-log plot of hardness vs strain rate as mentioned earlier. The average values of hardness of the three different strain rates are 7.37 and 6.71 GPa for the nanoglass and melt-spun ribbons, respectively. From the plots shown in fig. 5.8(c), the values of m for the nanoglass and the ribbons are 0.009 ± 0.002 and 0.036 ± 0.006 , respectively. By substituting these values in eq. (1), the volumes of STZ were found to be 7.41 and 1.93 nm³ for the nanoglass and the melt-spun ribbons, respectively. As mentioned before, Pan *et al.* [131] have experimentally observed by nanoindentation that the higher the ductility of the metallic glass, the larger is the STZ volume. Pd₄₀Ni₄₀P₂₀ is one of the most ductile bulk metallic glasses (BMG) with a STZ volume of 6.56 nm³. The volume of STZ in Cu₅₀Zr₅₀ nanoglasses (7.41 nm³) is comparable to that of Pd₄₀Ni₄₀P₂₀ BMG [131]. By assuming a spherical STZ, its radius would be 1.2 nm for a nanoglass, which is almost the size of interfacial width in nanoglasses [37].

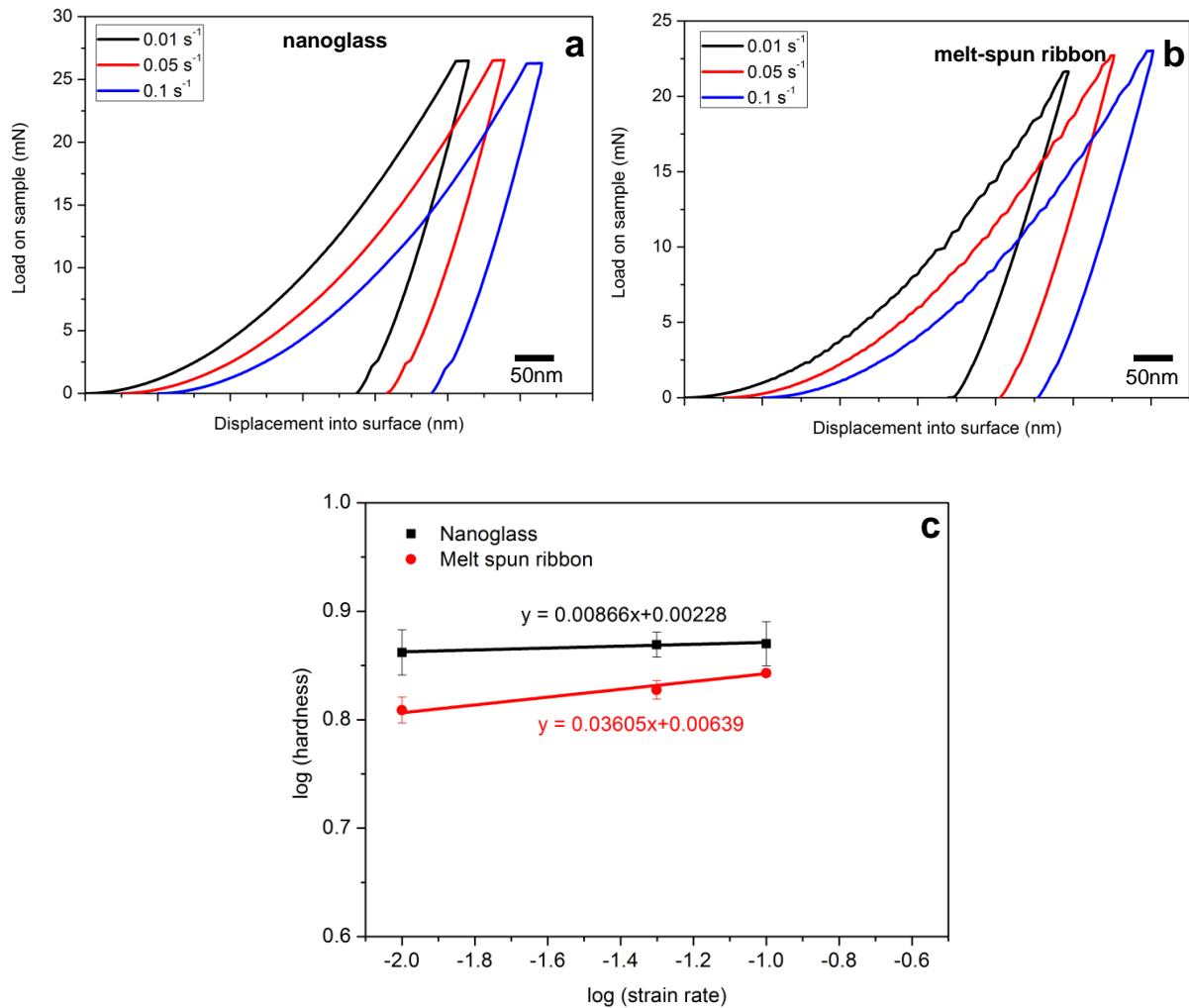


Fig. 5.10 Nanoindentation curves of (a) nanoglass and (b) melt-spun ribbons at three different strain rates. For better clarity, the starting points of the curves were shifted by 50 nm (c) log-log plots of hardness and strain rate for nanoglass and melt-spun ribbons.

5.6 Microcompression testing

Uniaxial microcompression tests were performed on Cu-Zr nanoglass and melt-spun ribbon. Engineering stress-strain curves at a displacement rate of 10 and 20 nm s^{-1} are presented in fig. 5.11(a) & (b). A clear difference in the deformation behavior is observed in the nanoglass compared to the melt-spun ribbon. It is clear from the stress-strain curves that the steps look smooth and continuous in the nanoglass compared to the melt-spun ribbon. This can also be observed from the deformed pillar images (see fig. 5.11(c)-(f)). One can clearly observe that the deformation looks less catastrophic in the nanoglass pillars (fig. 5.11(c) & (e)) compared to the conventionally rapidly quenched alloys (fig. 5.11(d) & (f)). Another important feature to observe from the stress-strain plots is that the yield strength of the nanoglass is considerably higher than the melt-spun ribbons. The yield strength of the nanoglass and melt-spun ribbon is 2020 and 1520 MPa respectively. It is consistent with the high hardness values obtained from the hardness measurements. Yield strength is considered where the first stress plateau is observed in the engineering stress strain curve.

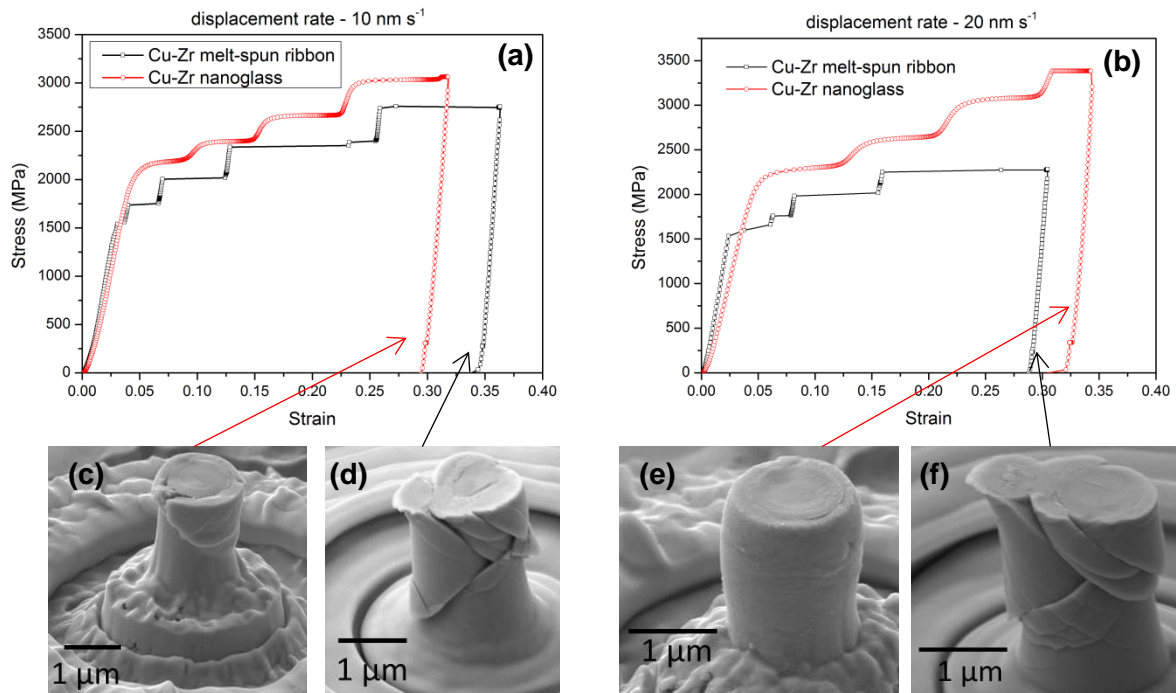


Fig. 5.11 Engineering stress-strain curves of Cu-Zr nanoglass and melt-spun ribbons at a displacement rate of (a) 10 nm s^{-1} , (b) 20 nm s^{-1} , corresponding deformed pillar images of (c) nanoglass at 10 nm s^{-1} , (d) melt-spun ribbon at 10 nm s^{-1} , (e) nanoglass at 20 nm s^{-1} and (f) melt-spun ribbon at 20 nm s^{-1}

5.7 Studies on $\text{Cu}_{60}\text{Zr}_{40}$ nanoglasses

Another glass forming composition $\text{Cu}_{60}\text{Zr}_{40}$ was also synthesized by magnetron sputtering in IGC and studied in the current work. XRD confirms the amorphous nature of the nanoglass

and melt-spun ribbon samples as shown in fig. 5.12 (a). As in $\text{Cu}_{50}\text{Zr}_{50}$ nanoglass, slight peak broadening is observed for $\text{Cu}_{60}\text{Zr}_{40}$ nanoglass samples compared to melt-spun ribbons. No crystallinity is observed in the nanoglass samples as is evident from the XRD patterns. One $\text{Cu}_{60}\text{Zr}_{40}$ nanoglass sample was annealed at $400\text{ }^\circ\text{C}$ for 3 h to test its thermal stability. Even the annealed sample remained amorphous with no crystalline peaks. The composition of the nanoglass was determined by EDS in SEM and it was found to be close to $\text{Cu}_{60}\text{Zr}_{40}$ as shown in fig. 5.12(b) & (c). The composition is within the experimental error of 2 at.%. As in $\text{Cu}_{50}\text{Zr}_{50}$ alloy system, oxygen peak is observed in the EDS spectrum of $\text{Cu}_{60}\text{Zr}_{40}$ nanoglass. It must be pointed out here that $\text{Cu}_{60}\text{Zr}_{40}$ is more prone to oxidation compared to $\text{Cu}_{50}\text{Zr}_{50}$ alloys. $\text{Cu}_{60}\text{Zr}_{40}$ ribbons oxidized much more quickly when left in air when compared to $\text{Cu}_{50}\text{Zr}_{50}$ melt-spun ribbons. Some of the $\text{Cu}_{60}\text{Zr}_{40}$ ribbons even got oxidized in the glove box (after 2 years) when the oxygen content in the glove box is roughly around 2-10 ppm.

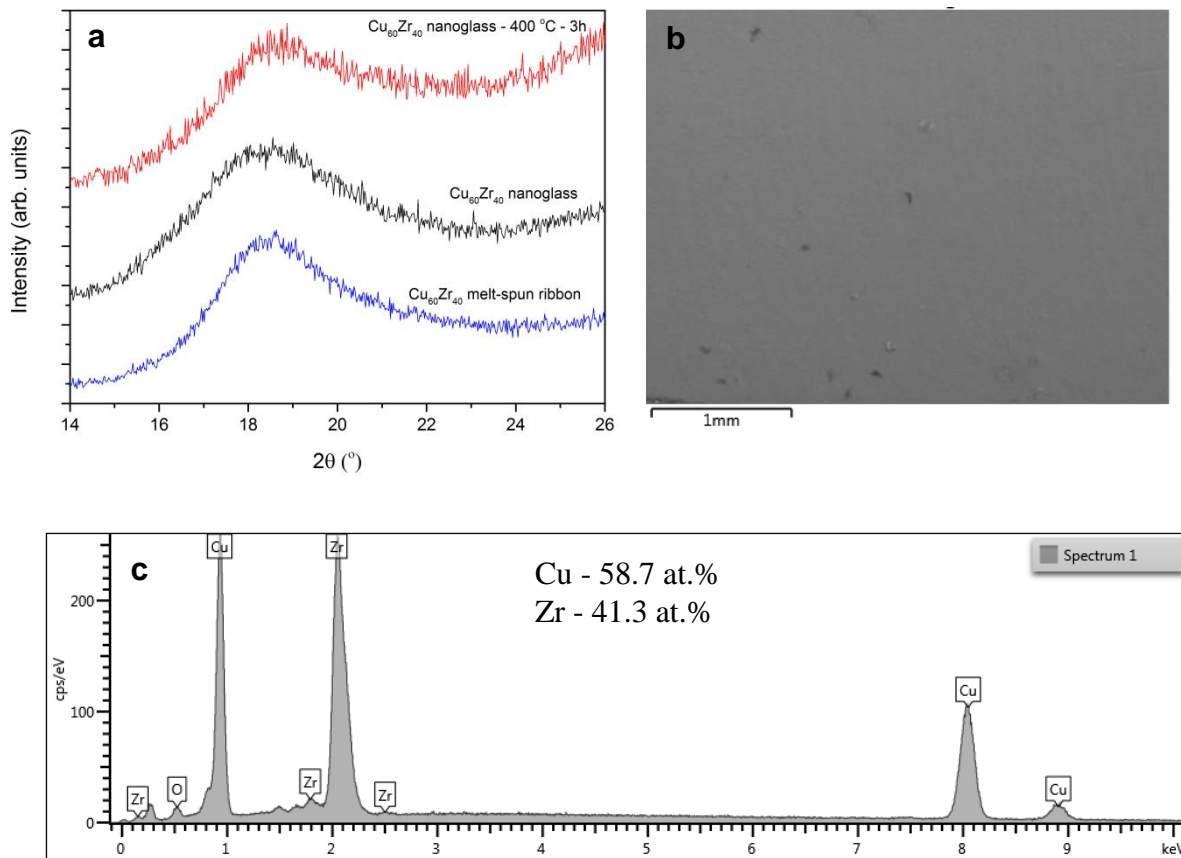


Fig. 5.12 (a) XRD of $\text{Cu}_{60}\text{Zr}_{40}$ melt-spun ribbons, nanoglass and annealed nanoglass, (b) Secondary electron image in SEM, (c) EDS spectrum obtained from the fig. (b). Composition obtained from the spectrum is also given in the figure.

APT of the $\text{Cu}_{60}\text{Zr}_{40}$ nanoglass shown in fig. 5.13(a) & (b) reveals the elemental segregation of Cu and Zr atoms at the nanoscale. In some regions, Cu and Zr fluctuated between 20 to 80 at.%. Also, a comparatively high oxygen content of about 4-5 at.% is also observed in $\text{Cu}_{60}\text{Zr}_{40}$ samples in APT. MD simulations by Adjaoud *et al.* [37] also found segregation in $\text{Cu}_{64}\text{Zr}_{36}$ nanoglasses of about 10 at.%. This segregation behavior in $\text{Cu}_{60}\text{Zr}_{40}$ alloys is similar to $\text{Cu}_{50}\text{Zr}_{50}$ nanoglasses.

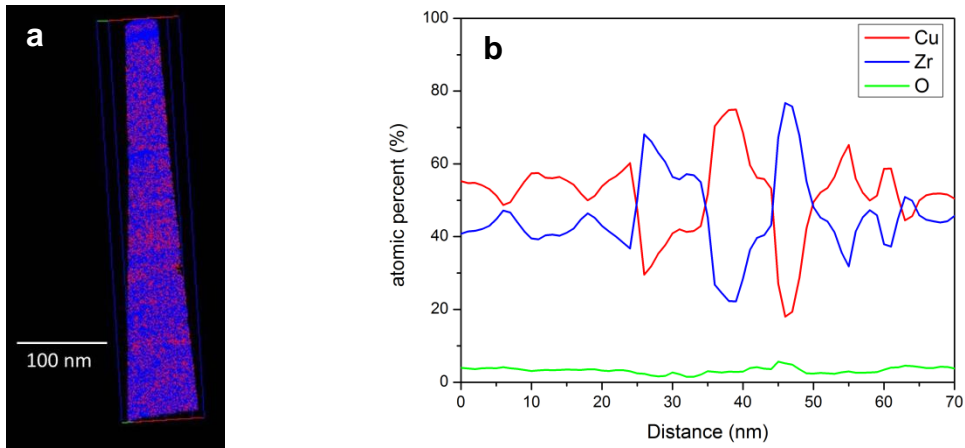


Fig. 5.13 (a) APT profile of $\text{Cu}_{60}\text{Zr}_{40}$ nanoglass and (b) composition profile along a cylinder in APT tomograph showing the composition segregation. Compositional fluctuation is much more in $\text{Cu}_{60}\text{Zr}_{40}$ compared to $\text{Cu}_{50}\text{Zr}_{50}$ nanoglassy alloy.

DSC of $\text{Cu}_{60}\text{Zr}_{40}$ nanoglass samples showed a large increase in glass transition and crystallization temperature as shown in fig. 5.14. All the values are summarized in table 5.1. Enthalpy of crystallization reaction for nanoglass and melt-spun ribbon samples is 40 and 53 J/g. A small shoulder is observed in the DSC curve of $\text{Cu}_{60}\text{Zr}_{40}$ nanoglass samples. The onset of crystallization temperature increased from 475 °C in melt-spun ribbons to 500 °C in nanoglasses. Like in $\text{Cu}_{50}\text{Zr}_{50}$ alloys, $\text{Cu}_{60}\text{Zr}_{40}$ melt-spun ribbons showed a glass transition whereas it is not so significant in the nanoglasses. T_g and T_x increased in $\text{Cu}_{60}\text{Zr}_{40}$ metallic glasses by the addition of oxygen into the alloys. A reduction in enthalpy of the crystallization reaction is also observed by the addition of oxygen to $\text{Cu}_{60}\text{Zr}_{40}$ metallic glasses [133]. It is surprising to observe that inspite of 4-5 at.% oxygen in the samples, the nanoglasses remain amorphous during annealing at 400 °C for a considerable duration of 3 h. Another important feature to be observed from the DSC measurements is the shoulder around 510 °C in the nanoglass, which also signifies that there is a secondary phase formation near that temperature regime.

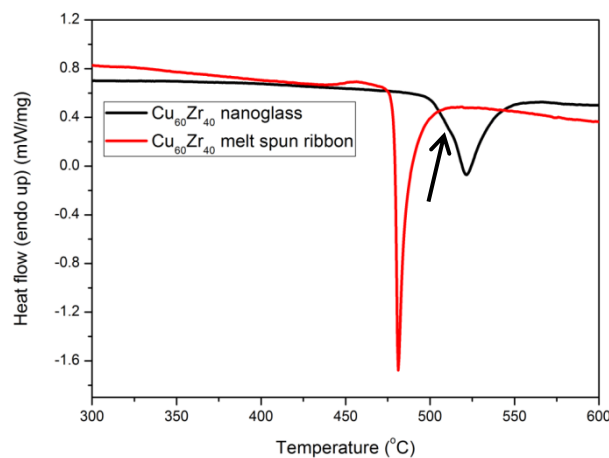


Fig. 5.14 DSC of $\text{Cu}_{60}\text{Zr}_{40}$ melt-spun ribbons and nanoglass samples. A shoulder is observed in the nanoglass sample which is marked by arrow in the figure.

To confirm whether $\text{Cu}_{60}\text{Zr}_{40}$ metallic nanoglasses behave similarly to $\text{Cu}_{50}\text{Zr}_{50}$ alloys, few indentation tests were carried out by using Vickers hardness measurements. It was found that slightly high hardness values were observed for nanoglass samples compared to melt-spun ribbons of the same composition. $\text{Cu}_{60}\text{Zr}_{40}$ melt-spun ribbons have a hardness of $464 \pm 18 \text{ HV}_{0.1}$ and nanoglass samples have a hardness of $491 \pm 31 \text{ HV}_{0.1}$. Similar to $\text{Cu}_{50}\text{Zr}_{50}$ alloys, high hardness values are observed in nanoglasses compared to melt-spun ribbons. Hardness values observed in $\text{Cu}_{60}\text{Zr}_{40}$ alloys are higher than these in $\text{Cu}_{50}\text{Zr}_{50}$ system. Park *et al.* [116] clearly found that the atomic packing density increases with increase in Cu content in Cu-Zr metallic glasses. A direct correlation between the Voronoi polyhedra, $\text{Cu}[0,0,12,0]$ and the atomic packing density is also observed. The increase in the five fold coordinated $\text{Cu}[0,0,12,0]$ clusters results in an increase in the modulus and hardness (strength) values in Cu-Zr metallic glasses [116]. The more interesting feature is the deformation behaviour of $\text{Cu}_{60}\text{Zr}_{40}$ nanoglasses (see fig. 5.15), which is similar to that of $\text{Cu}_{50}\text{Zr}_{50}$ nanoglasses. No shear bands were observed around the $\text{Cu}_{60}\text{Zr}_{40}$ nanoglass indents while shear bands were observed in the melt-spun ribbons of the same composition.

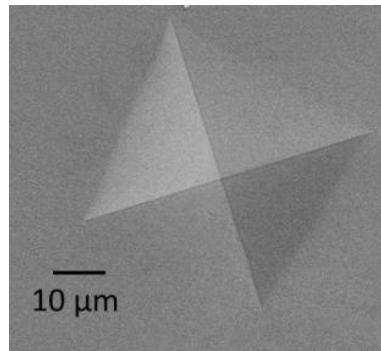


Fig. 5.15 Vickers indent of a $\text{Cu}_{60}\text{Zr}_{40}$ nanoglass under a load of 1000 gf

5.8 Discussion on the structure of nanoglass

There are some points to be noted before discussing on the structure of nanoglass. Although the effect of oxygen in the samples cannot be completely ruled out, it seemed to be less in $\text{Cu}_{50}\text{Zr}_{50}$ compared to $\text{Cu}_{60}\text{Zr}_{40}$ glassy alloys. More importantly, the change in the deformation behaviour from heterogeneous to homogeneous in both the nanoglass alloys is an important feature in Cu-Zr system. The effect of porosity can be ruled out in the deformation behaviour because of the higher hardness and modulus values in nanoglasses as compared with ribbons. So, the deformation behaviour must be an effect of atomic structure of the nanoglass. Segregation is observed in both $\text{Cu}_{50}\text{Zr}_{50}$ and $\text{Cu}_{60}\text{Zr}_{40}$ nanoglasses. Keeping this in mind, considering primarily $\text{Cu}_{50}\text{Zr}_{50}$, we propose a model which can explain the thermal and mechanical properties of the nanoglasses.

To start with, metallic nanoglasses are described as structures containing homogeneous glassy regions joined by interfacial regions of lower atomic density (with higher free volume) [8]. Positron annihilation spectroscopy confirmed the presence of free volume in the interfacial regions of $\text{Sc}_{75}\text{Fe}_{25}$ nanoglasses [10]. However, as mentioned earlier, segregation

of individual constituents is already observed in Fe-Sc nanoglasses [29,38]. MD simulations also suggest that Cu segregates to the surface of amorphous $\text{Cu}_{64}\text{Zr}_{36}$ nanoparticles [37]. The segregation in $\text{Cu}_{64}\text{Zr}_{36}$ amorphous nanoparticles was explained by the reduction of the cohesive energy (potential energy) rather than the surface energy. Thus, atoms with large cohesive energy, i.e., Zr in Cu-Zr, is driven to the core of the amorphous nanoparticle, while Cu segregates to the surface even though Zr has the larger atomic size of the two elements. APT results of $\text{Cu}_{50}\text{Zr}_{50}$ in the present study also confirm that there is segregation of Cu and Zr in Cu-Zr nanoglasses. Although the core-shell structure is not self-evident in the Cu-Zr nanoglass (fig. 3(b)) since the interfacial width of segregation is only ~ 1 nm (from MD simulations) and the particles have a size distribution between 4-10 nm, we can confirm the segregation in Cu-Zr nanoglasses from APT results.

Recently, it was observed that vapor deposition of amorphous films can lead to more relaxed structures, which cannot be formed by conventional liquid quenching techniques [31,54]. High sputtering power (420 W, in the present case) can lead to high plasma temperatures and high energies of the sputtered atoms [134]. Consequently, it is possible that the nanoparticles, which form in the vapor phase, have sufficient energy to rearrange to a relaxed structure. Combining all these observed results, we propose a structural model for the Cu-Zr nanoglass with the relaxed Zr-rich core regions with dense packing and Cu-rich shell regions or interfaces (probably with a composition gradient) as shown in fig. 5.16 (a)-(c). This model can explain the thermal and indentation properties of the Cu-Zr metallic nanoglasses as discussed below. A similar structural model was also recently predicted by Wang *et al.* [86] in $\text{Fe}_{90}\text{Sc}_{10}$ nanoglasses by small angle X-ray scattering measurements.

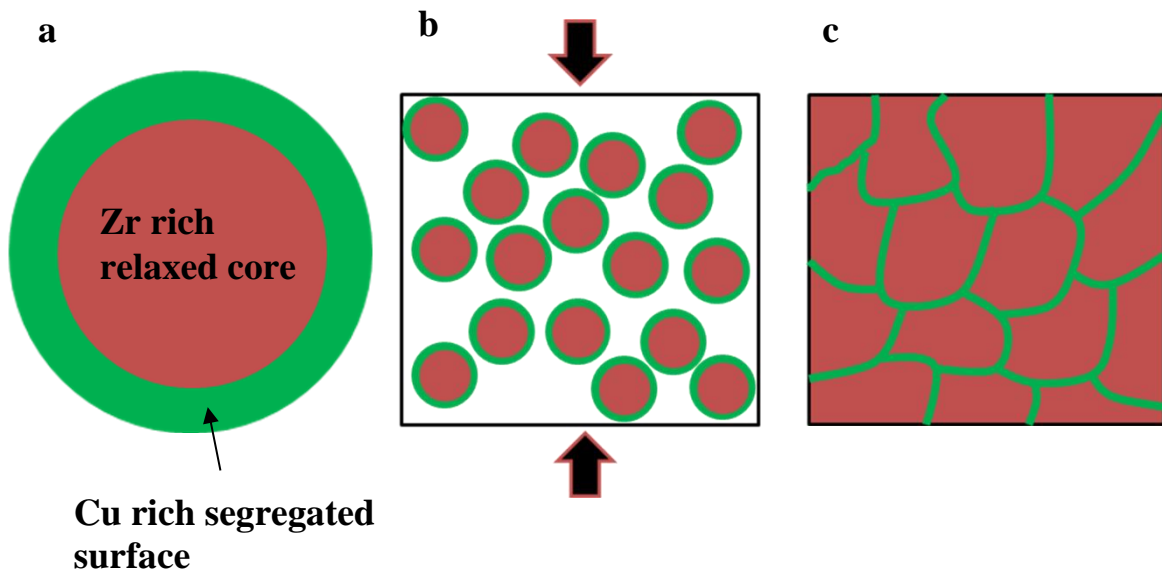


Fig. 5.16 Schematic indicating (a) segregated amorphous nanoparticle; (b) Compaction of amorphous nanoparticles and (c) nanoglass with segregated interfaces.

5.9 Thermal behaviour and its relation to the structure of nanoglass

Two important points (1) and (2), which were observed in the thermal behavior of nanoglasses, will be discussed in terms of the model:

- (1) Increase in T_g and T_x .
- (2) Lower enthalpy of crystallization reaction in a nanoglass.

5.8.1 Increase in T_g and T_x

It is known that the nucleation of crystalline phases can be accelerated in regions with high free volume [135,136]. Therefore, interfaces, which are sources of high free volume, can act as nucleation sites for crystallization reactions. If that was the case, Cu rich interfaces should crystallize first before Zr rich cores. The increase of the Cu content (up to 64 at.% Cu) increases T_g and T_x [4,116] in binary Cu-Zr metallic glasses. So, the increase in T_x of nanoglass compared to the melt-spun ribbon can be attributed to the segregation of Cu to the interfaces. In a segregated $\text{Cu}_{50}\text{Zr}_{50}$ nanoglass, if the Zr rich core had a structure similar to a homogeneous metallic glass, one would expect low T_g and T_x because the Zr rich core should crystallize first before the Cu rich interface. This is due to the fact that, in the Cu-Zr system, Zr rich metallic glasses have lower T_g and T_x as compared with Cu-rich ones [4,116], but the opposite is actually observed (fig. 5.5). Therefore our present model of a relaxed Zr-rich core can explain the increase in crystallization temperatures, because it means that cores are more stable than Cu rich interfaces. Similar conclusions were drawn from the analysis of the MD simulations during the formation of amorphous particles in the $\text{A}_{80}\text{B}_{20}$ Kob-Andersen model system by Danilov *et al.* [88]. We have also observed slightly low T_x values for $\text{Pd}_{84}\text{Si}_{16}$ nanoglasses when compared to melt-spun ribbons, which also confirm the model presented (see fig. 6.3(a) and table 6.1). MD simulations report that segregation of Pd to the surface of the nanoparticle is observed in $\text{Pd}_{80}\text{Si}_{20}$ nanoglass [37]. If interfaces crystallize first as predicted, one should expect low T_x for Pd-Si nanoglasses since it decreases with the increase in Pd content (between 80-85 at.%) in Pd-Si metallic glasses [4]. Thus, our hypothesis that interfaces crystallize first seems reasonable, which is accounted to the structural differences at the interfaces compared to the cores.

5.8.2 Enthalpy of crystallization reaction

The heat of crystallization, ΔH_x for a nanoglass is less compared to a melt-spun ribbon of the same composition. Reduced ΔH_x values are also observed for $\text{Pd}_{84}\text{Si}_{16}$ nanoglasses (see table 6.1) compared to melt-spun ribbon of similar composition. Similar reduced ΔH_x values are observed in Au-based nanoglass thin film [36] and organic glasses [55]. The reduction in enthalpy of the organic glasses is explained by their relaxed nature obtained during deposition [55]. A conservative estimate for the enthalpy of the Cu-Zr nanoglass with segregated regions can be made by assuming that the segregation is uniform in the cores and the interfaces. In a $\text{Cu}_{50}\text{Zr}_{50}$ particle of a diameter of 6 nm with a segregation width of about 0.5 nm, and a core composition of $\text{Cu}_{45}\text{Zr}_{55}$, one obtains the composition on the surface to be

approximately $\text{Cu}_{57}\text{Zr}_{43}$. The enthalpies of $\text{Cu}_{45}\text{Zr}_{55}$ and $\text{Cu}_{57}\text{Zr}_{43}$ are 65.9 and 58.2 J/g, respectively [137]. An interfacial volume fraction of about 30% can be expected for a particle size of ~ 6 nm, which would result in a weighted enthalpy of about 63.6 J/g. One should also take note that the enthalpy change with the composition from $\text{Cu}_{45}\text{Zr}_{55}$ to $\text{Cu}_{57}\text{Zr}_{43}$ is approximately only 10%, which cannot explain the large decrease ($\sim 44\%$) in enthalpy of crystallization reaction. We conclude that the decrease of enthalpy by $\sim 44\%$ in nanoglasses cannot be explained by a segregation effect. Consequently, there seems to be a structural difference between the cores and the interfaces (high free volume) with cores in more relaxed state compared to a homogeneous metallic glass give rise to a decrease in enthalpy. The enthalpy of the nanoglass after annealing for 3h (32 J/g) is still lower than that of the melt-spun ribbon (55 J/g) which indicates that the structure is not destabilized for short annealing times. Longer annealing times seem to relax the structure of the nanoglass, which is evident from the reduced enthalpy of the crystallization reaction.

5.8.3 Young's modulus, plasticity, STZ volume and its relation to the structure

Important observations from the indentation tests are that the hardness and modulus in Cu-Zr nanoglasses are comparable to melt-spun ribbons. If the free volume of the interfaces is high, then one would expect a low elastic modulus for the nanoglass compared to the melt-spun ribbons as in nanocrystalline materials (assuming the core has a structure similar to the homogeneous metallic glass) because of the disorder at the interfaces. The elastic modulus and hardness of nanoglasses are slightly higher than the melt-spun ribbon (see table 5.1), which also signifies that the core is denser (relaxed) compared to a homogeneous metallic glass (fig. 5.16). The regions with high free volume act as nucleating sites for STZ in metallic glasses [5]. Interfacial regions, which are sources of high free volume, can act as nucleation sites for large number of STZ's aiding in homogeneous deformation in metallic nanoglasses [39,93]. Homogeneous deformation is observed in the nanoglasses even after annealing at 350 °C for 3 h indicating that a major fraction of interfaces are still present. This also confirms that the interfaces do not delocalize even after annealing at $0.9 T_g$. This can be understood by the relaxed core region, which does not allow the interfaces to delocalize. Some studies have reported that the high plasticity in $\text{Cu}_{50}\text{Zr}_{50}$ metallic glass is due to the presence of crystallinity in the sample, which is formed during the synthesis or deformation [138,139]. No crystalline phases are present in the nanoglasses before and after indentation (fig. 5.2(b) & 5.8(d) & (e)), which also indicates that the homogeneous deformation in nanoglasses is a result of the basic underlying nanostructure. An alternative explanation to explain the mechanical properties is the possibility of considering the nanoglass as a two phase system, which would mean that the increase in hardness and modulus is an average of the two phases (interfaces and cores) in the system. If the core regions of a nanoglass have an elastic modulus and hardness greater than the metallic glasses (since the core is in a relaxed state), then it is possible that the average values of the two phases (interfaces and cores) is greater than the corresponding melt-spun ribbon.

5.10 Summary

1. $\text{Cu}_{50}\text{Zr}_{50}$ and $\text{Cu}_{60}\text{Zr}_{40}$ metallic nanoglasses were synthesized using a modified IGC method employing magnetron sputtering at elevated gas pressures. The amorphous nature of samples is confirmed by XRD and TEM. Atom probe tomography confirmed elemental segregation of Cu and Zr on the length scale of the primary amorphous nanoparticles. It seems that $\text{Cu}_{60}\text{Zr}_{40}$ alloy system is more prone to oxidation while it is less in $\text{Cu}_{50}\text{Zr}_{50}$ glassy alloys.
2. Based on the results on $\text{Cu}_{50}\text{Zr}_{50}$ nanoglasses, a segregation model is proposed with Zr-rich dense cores and Cu-rich interfaces with increased free volume, which can explain the low enthalpy and high T_g of the nanoglass samples compared to melt-spun ribbons.
3. Nanoglasses show a slight increase of hardness and modulus (10%) compared to the melt-spun ribbons, which can also be explained by the proposed model. Homogeneous deformation was observed in nanoglasses during indentation whereas the melt-spun ribbons deformed by shear bands. The interfaces with high free volume promote the nucleation of many STZ's, which results in homogeneous deformation. Interfaces in a nanoglass seem to be stable even after annealing which can be inferred from the low enthalpy and homogeneous deformation in the annealed nanoglasses.

6. Effect of topological structure on mechanical properties of Pd-Si nanoglasses synthesized by IGC

In this chapter, we discuss the effect of topological structure on mechanical properties of Pd-Si nanoglasses. Here we perform mechanical tests on Pd-Si metallic glasses and nanoglasses by using uniaxial microcompression and compare the results directly with MD simulations of a similar composition. Hence, we will comment on the effect of topological structure at the interfaces on the shear band formation in metallic nanoglasses.

6.1 Experimental details

Pd₈₀Si₂₀ melt-spun ribbons were prepared by using standard melt-spun technique. Nanoglass samples were synthesized by using DC magnetron sputtering in IGC at a working pressure of 0.3 mbar. The initial composition of the target material is Pd₈₀Si₂₀. The in situ (in IGC chamber) consolidated pellet was additionally processed in a high pressure torsion (HPT) machine using tungsten carbide anvils under hydrostatic conditions at a pressure of 6 GPa rotating the sample by 90°. High pressure torsion was employed in the current set of experiments to densify the sample rather than to introduce plastic deformation, which is the reason why only a quarter of revolution is applied during torsion. The amorphous nature of the nanoglass and melt-spun ribbon samples was confirmed by performing XRD measurements using a Philips Xpert Mo K α source. The composition of all the samples was determined by EDS equipped in a Leo 1530 SEM. The density of the nanoglass and HPT-processed nanoglass samples was measured by standard Archimedes principle using dimethyl phthalate as the liquid medium (density of dimethyl phthalate = 1.19 g/cc). APT measurements were carried out using a Cameca-LEAP 4000X HR instrument in laser pulsing mode (wavelength 355 nm, pulse frequency 100 kHz, sample temperature 60 K, pulse energy 60 pJ, evaporation rate 1%). The reconstruction of the APT data was performed with IVAS 3.6.14. Details regarding tip preparation were mentioned in the experimental section 3.2.7. Nanoglass and HPT-processed nanoglass samples were polished by standard metallographic techniques for micro- and nanoindentation. Nanoindentation was done on all the samples using a Hysitron indenter with a Berkovich tip at an indentation strain rate of 0.05 s⁻¹. Imaging of indents was performed using a secondary electron detector in SEM. Focused ion beam (FIB) milling of melt-spun ribbon and nanoglass samples were done by FEI Strata 400 STEM using Ga ions to make pillars of micron size. All the pillars were milled in four steps to ~1 μ m size in diameter and the aspect ratio of the pillars is ~2:1. To minimize the damage caused by Ga ions, very low currents of 260 and 90 pA were used in the final two steps of milling process. The aspect ratio of the pillars is 2:1 for nanoglass and HPT-processed nanoglass, 2.5:1 for melt-spun ribbons. Micropillar testing was carried out using Insem (Nanomechanics Inc.) machine with a flat indenter of 5 μ m in diameter. Correction for the compliance of the substrate is performed by using Sneddon's equation. The elastic modulus of the nanoglass sample is taken from the nanoindentation data to perform the correction.

6.2 Simulation details

To investigate the deformation behavior, the origin of shear band formation in metallic glasses and nanoglasses during uniaxial compression tests, we performed molecular dynamics simulations on Pd-Si metallic glass and nanoglass pillars by using the LAMMPS simulation package [111] with an embedded atom method (EAM) potential for Pd-Si [112]. This potential has been optimized to predict accurately the structure of liquid and amorphous Pd-Si alloys around the eutectic composition $\text{Pd}_{100-x}\text{Si}_x$ ($x=17.5$) and successfully applied to Pd-Si glasses [37,77,113,114,140]. To this end, we obtained the $\text{Pd}_{80}\text{Si}_{20}$ metallic glass by cooling an equilibrated melt, at 2000 K for 2 ns, to 50 K with a cooling rate of 0.01 K/ps. We produced the $\text{Pd}_{80}\text{Si}_{20}$ metallic nanoglass by consolidating several glassy spheres, which were equilibrated first in the liquid phase and then quenched to the glassy state [87]. The diameter of the glassy spheres is ranging from 6 to 8 nm. Simulation details are provided in the experimental section 3.4.

6.3 Structural characterization

All the investigated samples were confirmed to be amorphous by XRD as shown in fig. 6.1(a). Even the HPT-processed nanoglass sample is found to be amorphous as seen from the XRD pattern in fig. 6.1(a). The primary motivation to perform HPT on the nanoglass samples is to reduce the porosity in the sample. TEM analysis confirmed the as prepared nanoglass samples are amorphous without any indication of crystalline phase. The size of the nanoparticles is determined by TEM and the size distribution is found to vary between 6-20 nm as shown in fig. 6.1(b). The composition of nanoglass samples is found to be $\text{Pd}_{84}\text{Si}_{16}$ by SEM-EDS measurements (see fig. 6.1(c) & (d)). The top surface of the sample also showed residual porosity (marked by arrows in fig. 6.1 (c)) because of incomplete consolidation, which can lead to slight oxidation. To verify the total amount of oxygen content in the sample, one sample was tested using carrier gas hot extraction method. Interestingly, the oxygen content in the sample is found to be ~2 at.%, which is similar to Cu-Zr metallic nanoglasses. It must be pointed out here that unlike Cu-Zr nanoparticles, which spontaneously combusted (caught fire) in case of a sudden exposure to air, Pd-Si nanoparticles were more stable. So, this also conveys us that the oxidation of Pd-Si nanoparticles is comparatively less than Cu-Zr glassy alloys. Relative density of the as-prepared and HPT nanoglass sample is 95 and 98%, respectively, assuming that the density of the melt-spun ribbons is 10.33 g/cc (theoretical density of $\text{Pd}_{82}\text{Si}_{18}$ [64]).

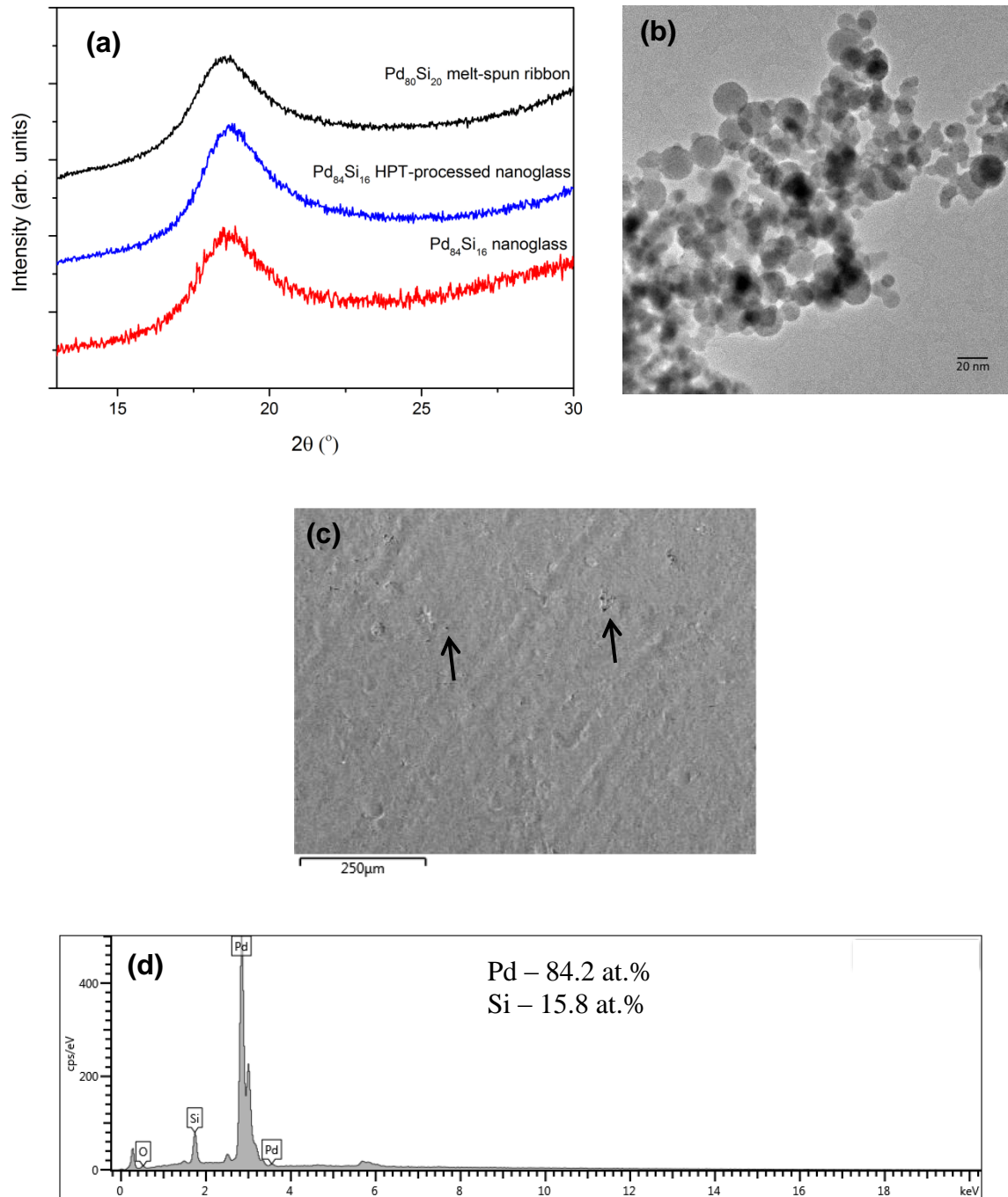


Fig. 6.1 (a) XRD showing the amorphous nature of all the samples, (b) TEM image of Pd-Si particles (c) SE image of Pd-Si nanoglass and (d) EDS spectrum obtained from the red rectangle in (c). The composition of the spectrum is shown in the figure.

To determine the extent of segregation, atom probe tomography is performed on the as prepared nanoglass and melt-spun ribbon samples. The APT reconstruction is shown in fig. 6.2(a). Composition profiles of Pd, Si and O atoms were obtained along a cylinder from the APT as shown in fig. 6.2(b). Although some fluctuations are observed, it did not show considerable segregation of Pd and Si. Some large compositional fluctuations are also observed in a few regions, which is probably because of the oxidized regions as indicated by

arrows in fig. 6.2(b). As mentioned before, regions of open porosity on the top surface of the sample are prone to oxidation. If APT sample is taken from such a region, there will be some oxidized regions as indicated by arrows in fig. 6.2(b). On a whole, the average oxygen concentration is around 1 at.% (see fig. 6.2 (b) & (c)) from the APT data which is similar to the value obtained by carrier gas hot extraction method. To give an average compositional segregation, proxigram is obtained from the Si isoconcentration surface at a concentration of 15 at.% which is shown in fig. 6.2(c). The advantage of the proxigram analysis is that the chemical compositional variations at fixed distances from an isoconcentration surface can be observed, irrespective of the actual shape and particle size. It is clear from the fig. 6.2(c) that the average composition of Pd is ~ 80 at.% and Si is ~20 at.%. For comparison, APT is also performed on Pd-Si melt-spun ribbons. The composition profile obtained from a APT reconstruction showed a uniform composition of Pd at 80 at.% and Si at 20 at.% as shown in fig. 6.2(d). MD simulations [37] already predicted very little elemental segregation of about 3 at.% in Pd-Si glassy nanoparticles. Such small fluctuations in the region of 1-2 nm regime are probably not detectable by using APT.

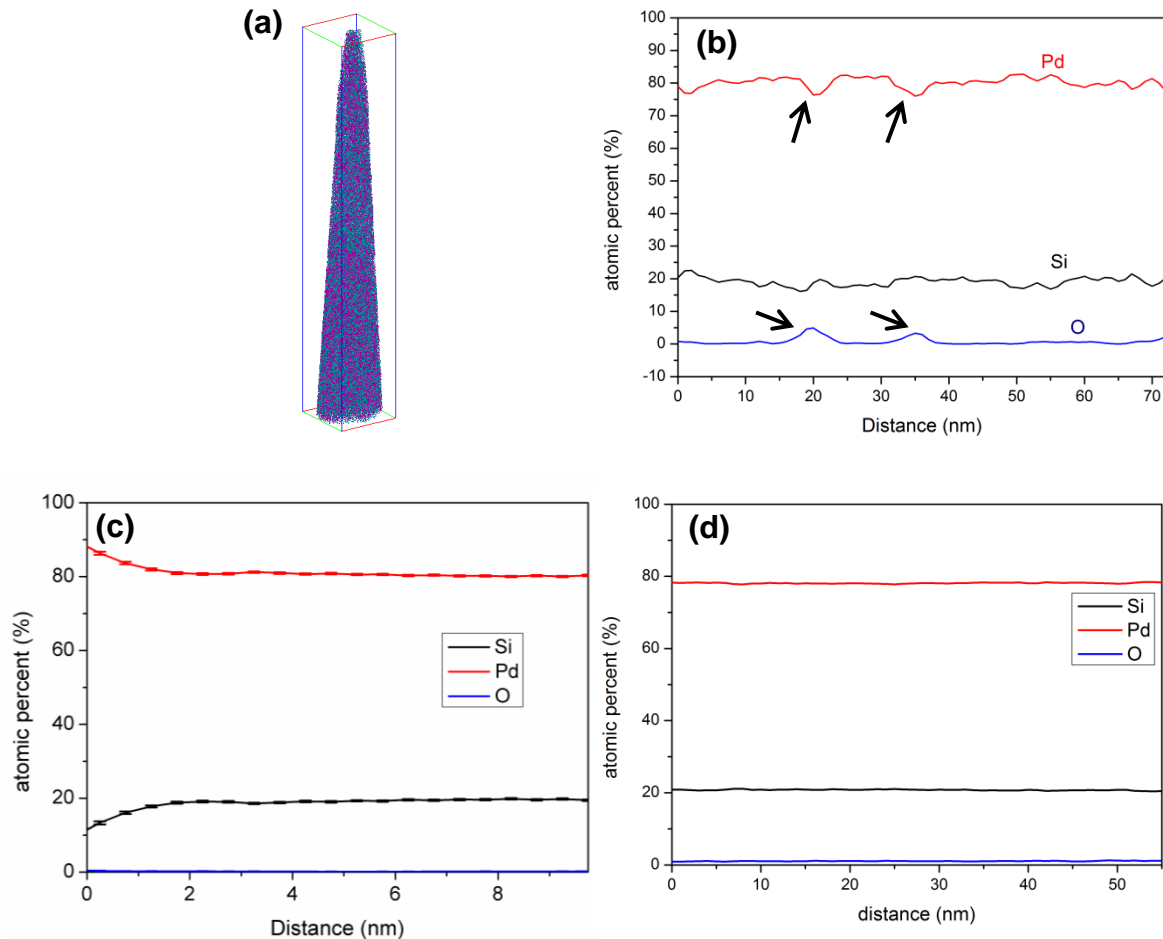


Fig. 6.2 (a) APT tip of the nanoglass showing the Pd and Si atoms (Pd is denoted by purple and Si is denoted by cyan), (b) average composition profile along a cylinder shown in (a), indicating Pd, Si and O atomic percentages, (c) proxigram showing the average composition profile across a 15% Si iso-surface in a nanoglass and (d) average composition map along a cylinder in (a) from Pd-Si melt-spun ribbons

DSC is performed on the nanoglasses as well as the reference melt-spun ribbons to determine T_g and T_x . It is found to be less in nanoglasses compared to melt-spun ribbons as shown in fig. 6.3(a). All the values are summarized in table 6.1. T_g of the nanoglasses and melt-spun ribbons is 321 and 367 °C, respectively. Unlike the Cu-Zr nanoglasses, where the glass transition is not clearly evident, Pd-Si nanoglasses clearly showed a glass transition. Also, the glass transition is not so significant in the nanoglass compared to the melt-spun ribbon as is evident from fig. 6.3(b). For a direct comparison, T_g and T_x values for Pd₈₄Si₁₆ melt-spun ribbon are compared with literature, see table 6.1 [4,141]. These values are considerably higher than the T_g of Pd₈₄Si₁₆ nanoglasses. In spite of the slightly different composition of nanoglasses and melt-spun ribbons, it is clear that such a large decrease in T_g in nanoglasses could not be a change in composition alone. Although the segregation in nanoglasses is not so significant to be detected by APT, assuming the MD simulations are correct, the previous speculated model of Pd rich interfaces and relaxed Si enriched cores can explain the reduction in glass transition temperature. MD simulations also show that Pd-rich interfaces have (111) Pd facets in the nanoglass [37], which can act as nucleating sites for crystallization reducing the glass transition and crystallization temperature. In general, interfaces which are rich in Pd and sources of free volume can crystallize first reducing T_g , since increase in Pd content in Pd-Si metallic glasses reduces the glass transition and crystallization temperature [4].

It is interesting to note that HPT-processed nanoglass showed a small exothermic peak (indicated by red arrow in fig. 6.3(b)) near the glass transition regime, which is not observed in either the as prepared nanoglass or the melt-spun ribbon. We confirmed that the peak is not an artifact since it is also observed at other heating rates of 5 and 10 °C/min. The reason for the peak near T_g is not investigated in the present work. Melt-spun ribbons have undergone crystallization in a single step while nanoglasses undergo crystallization in two stages as shown in fig. 6.3(a). In fact, the second crystallization event around 375 °C almost vanished in the HPT-processed nanoglass. The phases forming at each crystallization step in the nanoglasses are not investigated in the current work. Within the experimental error, the values for the onset of crystallization temperature in the HPT and as prepared nanoglass are almost the same. A reduction in the enthalpy of crystallization reaction is observed in the as prepared and HPT-processed nanoglass compared to melt-spun ribbon, which fits well with the DSC results obtained in Cu-Zr nanoglasses. Indeed, the reduction in enthalpy in the nanoglasses is almost 50% compared to melt-spun ribbons. The reason for such a large decrease in the enthalpy can be explained by the model proposed in section 5.5. The nanoparticles, which form in IGC (vapor deposition technique), can be in a relaxed state giving rise to lower enthalpy compared to melt-spun ribbons.

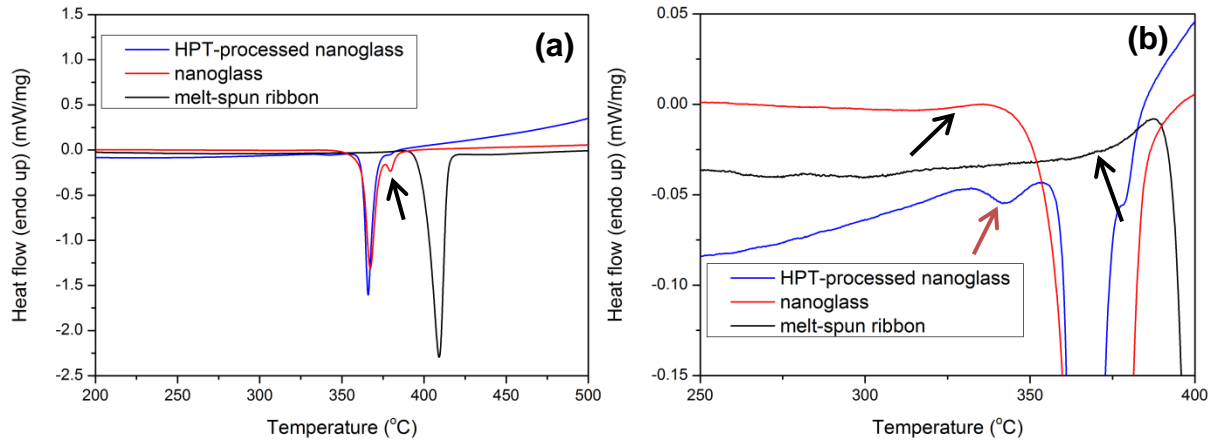


Fig. 6.3 (a) DSC showing the T_g , T_x of the nanoglass, HPT-processed nanoglass and melt-spun ribbons, black arrow in the figure indicates second crystallization step, (b) magnified image of the glass transition regions in all the three samples. Black arrows indicate glass transition while the red arrow indicates the exothermic peaks in HPT-processed nanoglass around glass transition

Table 6. 1 Onset of crystallization, hardness and modulus obtained by nanoindentation of all samples

	T_g (°C)	T_x (°C)	Enthalpy of crystallization (J/g)	Hardness by nanoindentation	Young's modulus by nanoindentation (assuming a poisson's ratio of 0.41)
melt-spun ribbon	374	394	50	5.86 ± 0.04	101 ± 0.75
nanoglass	324	356	28	5.1 ± 0.1	88 ± 1.7
HPT-processed nanoglass	-	361	27	5.6 ± 0.2	92 ± 2.5
Pd ₈₄ Si ₁₆ melt-spun ribbons [4]	362	367	-	-	-
Pd ₈₄ Si ₁₆ melt-spun ribbons [141]	347.7	371.3	-	-	-

To further understand the thermal behavior of metallic nanoglasses and melt-spun ribbons, DSC is performed on both nanoglass and melt-spun ribbons at four different heating rates as shown in fig. 6.4 (a) & (b). By employing the Kissinger equation (eq. 5.1) mentioned in section 5.3, the activation energy of the crystallization reaction is calculated for the nanoglasses and melt-spun ribbons as shown in fig. 6.4(c). Since Kissinger analysis depends on the peak crystallization temperature (T_p) and both the nanoglass samples, i.e. as prepared and HPT-processed, showed similar T_p values, only HPT-processed samples were used for activation energy analysis. Activation energy is calculated only for the primary crystallization peak in the nanoglass samples. The second crystallization event in the HPT-processed sample is very weak at a heating rate of 5 and 10 °C/min. The activation energy of the crystallization reaction of the nanoglass and melt-spun ribbon is 335 ± 22 and 327 ± 8 kJ/mol, respectively. Within the experimental error, both the nanoglass and melt-spun ribbon samples have

comparable activation energy. Wang *et al.* [141] recently found that the activation energy for the onset of crystallization (T_x) reaction of $\text{Pd}_{81}\text{Si}_{19}$ binary metallic glass is 316 kJ/mol, which is very close to the value obtained in the present work.

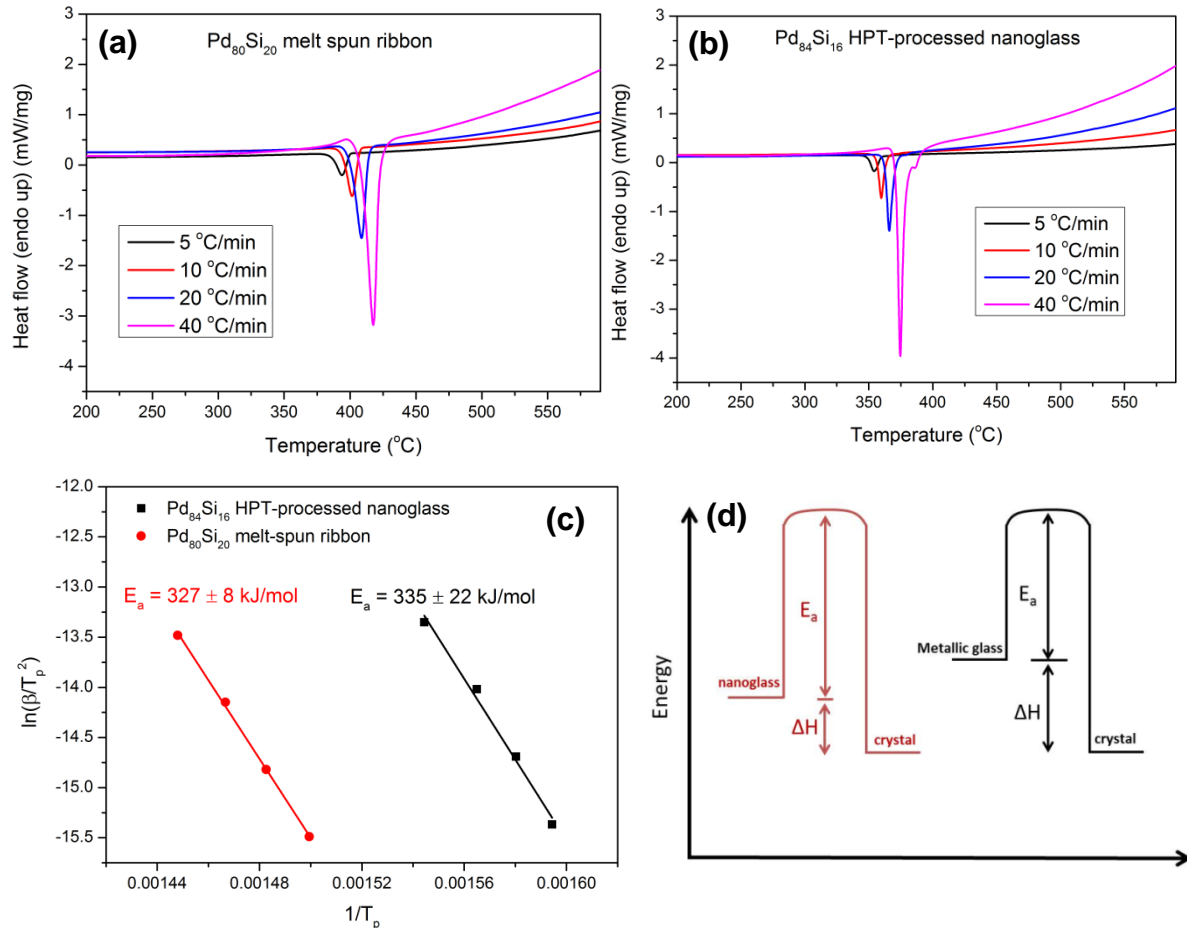


Fig. 6.4 DSC at different heating rates of (a) melt-spun ribbons, (b) HPT-processed nanoglass and (c) activation energy plots based on Kissinger equation of the nanoglass and melt-spun ribbon and (d) Energy diagram for the nanoglass and conventional metallic glass. Predominantly nanoglasses show higher activation energy and lower enthalpy than the conventional melt-spun ribbons.

Based on the calorimetric observations in both Cu-Zr and Pd-Si nanoglasses, some important observations can be made. Enthalpy of crystallization reaction in nanoglasses is lower than conventional rapidly quenched glasses. Activation energy of the crystallization reaction is higher in nanoglasses compared to rapidly quenched alloys. One can speculate an energy diagram (see fig. 6.4(d)) on the structural state of the nanoglasses when compared to conventional metallic glasses. Similar energy schematic is recently proposed by Ivanisenko *et al.* [142]. However, one must clearly understand that several metastable states are possible in metallic glasses depending on the cooling rate, processing conditions and the crystal phases possible after complete crystallization which will influence the proposed energy diagram.

6.4 Indentation tests

Nanoindentation is performed to test the mechanical properties and deformation behaviour of melt-spun ribbon and nanoglass. Load-displacement curves obtained from nanoindentation of all the samples are presented in fig. 6.5. Melt-spun ribbons show pop-ins (indicated by arrows) in the load displacement curves, which are indicative of shear band generation. As-prepared and HPT-processed nanoglass sample also showed pop-ins in the load-displacement curves, but they were less in number when compared to melt-spun ribbons, which is an indication that the deformation is less heterogeneous. Such deformation behavior in Pd-Si nanoglasses is in contrast to $\text{Cu}_{50}\text{Zr}_{50}$ nanoglasses (see fig. 5.6) where a homogeneous deformation is observed [124]. The hardness and modulus values of all the samples investigated are summarized in table 6.1. It is interesting to note that the Young's modulus and hardness of nanoglasses, both in the as prepared and HPT state are less than the melt-spun ribbons. Unlike in Cu-Zr nanoglasses where an increase in hardness and modulus were observed, a decrease in the modulus and hardness values is observed in Pd-Si nanoglasses. The reason for the decrease in modulus and hardness of Pd-Si metallic nanoglasses can be affected by the following factors.

1. Porosity in the sample.
 2. Slightly higher Pd content in nanoglasses compared to ribbon
 3. Microstructure of the nanoglass sample
1. To start with, even the as-prepared nanoglass samples have a density of about 95%, which is sufficiently high for nanoindentation since indentations are performed at a depth of only few hundreds of nanometers and results are averaged over more than 10 individual nanoindents. Note also that the reduction in porosity to almost 2 % in HPT-processed nanoglass had not led to a significant increase in hardness and modulus of nanoglasses. Furthermore, Cu-Zr nanoglasses with a relative density of 92% showed comparable Young's modulus to the melt-spun ribbons. So, we can conclude that porosity is not the major factor affecting the decrease in hardness and modulus of the nanoglass.
 2. Chen *et al.* [143] performed tensile tests to find out the Young's modulus of the Pd-Si melt-spun ribbons. It was observed that Young's modulus did not change much when the Si content is increased from 16 to 20 at.% in binary Pd-Si metallic glasses. In Pd-Si nanoglasses, the reduction in modulus compared to melt-spun ribbons is almost 10 %, which we believe could not be explained solely by the increase in Pd content.
 3. The microstructure of the nanoglass with chemically segregated interfacial regions can be considered to be the most plausible explanation. It is interesting to note that while the modulus and hardness values are comparable in Cu-Zr nanoglasses, it is found to be less in Pd-Si nanoglasses compared to the conventional melt-spun ribbons. Cu-rich interfaces are predicted to form in Cu-Zr nanoglasses (see section

5.5) whereas Pd-rich interfaces form in Pd-Si nanoglasses based on MD simulations. MD simulations also showed that regions with 2-dimensional hexagonal close packed surface (like (111) fcc Pd) units form in Pd-Si glassy nanospheres which are retained in the interfacial regions of Pd-Si nanoglasses [37]. So, the important question to be addressed is: Does chemical segregation alone answer such differences in elastic modulus? Here, one has to also consider the effect of bonding between constituent elements to explain the differences in elastic modulus as it predominantly depends on the strength of the chemical bond. In Cu-Zr alloys, the bonding between Cu and Zr atoms is metallic in nature while it is of covalent nature between Pd and Si atoms. Therefore, the interfacial regions, which contain more Pd-Pd metallic bonds compared to the Pd-Si covalent bonds probably contribute more in the decrease of the elastic modulus in the nanoglass compared to melt-spun ribbon. In Cu-Zr nanoglasses, since the bonding is predominantly metallic in nature, the elastic modulus is comparable to the melt-spun ribbons despite the chemical inhomogeneity in the nanoglasses. So, one has to take into account the chemical, topological as well as the chemical bonding to predict the elastic modulus in nanoglasses.

The slight increase in modulus and hardness of HPT nanoglass sample compared to the as-prepared nanoglass is probably due to the increase in density of the sample. At this point, it is important to mention that severe plastic deformation like HPT can cause a local change in the atomic structure in the nanoglass. Since HPT causes a radial increase in strain during deformation, to reduce such inhomogeneous microstructure, only a quarter of revolution is performed on the sample. To check for any inhomogeneities in the sample, few Vicker's indents at 1000 gf were carried out at the center and at the edge of the sample. Very little change in hardness is observed from the center (383 HV1) to the edge (378 HV1) of the sample. So, it is fair to assume that even though there is a structural change in the HPT-processed nanoglass, the influence on the actual hardness value is minimal.

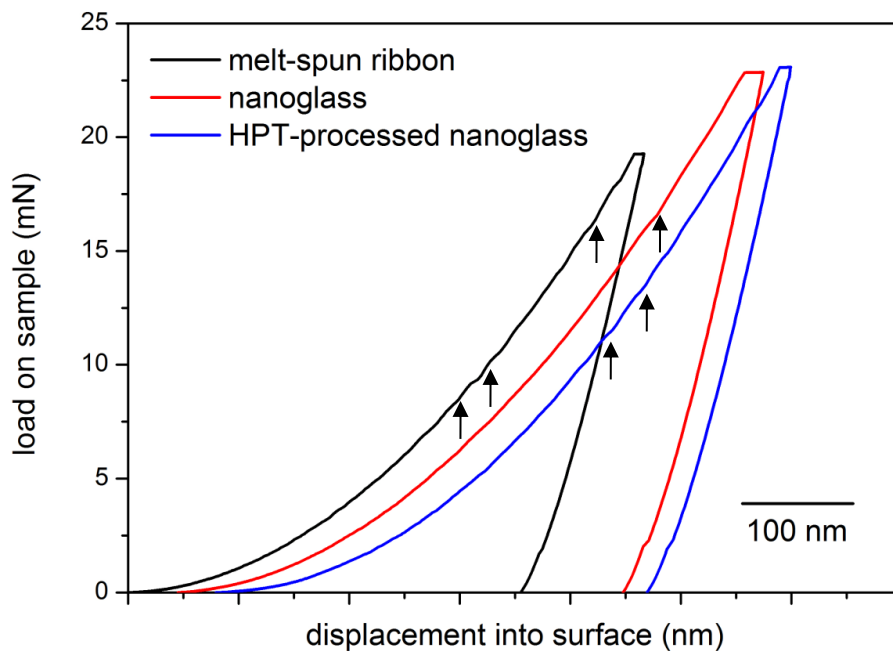


Fig. 6.5 Load-displacement curves of all the samples obtained using nanoindentation

6.5 Microcompression tests

Uniaxial microcompression tests were performed on all the samples to observe the deformation behavior. To avoid size effects, the diameter of the pillars is chosen such that it is $\sim 1 \mu\text{m}$. Volkert *et al.* [144] have already shown that when the pillar diameter is reduced to less than 500 nm, homogeneous deformation is observed in Pd-Si metallic glass. The engineering stress - strain data from the micropillar tests obtained at a cross head displacement rate of 10 nms^{-1} is shown in fig. 6.6. Each step in the stress-strain curve corresponds to the formation of a shear band. All the curves presented in fig. 6.6 were deformed to a displacement of 1000 nm. The low strain values in melt-spun ribbons was observed because of the higher aspect ratio (higher initial length) compared to nanoglass pillars. Shear bands were observed in all the micropillars tested at 10 and 20 nms^{-1} as shown in fig. 6.7(a)-(f). Previous results on $\text{Sc}_{75}\text{Fe}_{25}$ nanoglass [34] micropillars showed homogeneous deformation for pillars with diameter less than 300 nm while shear banding is observed for pillars with a diameter of $2 \mu\text{m}$. The yield strength of nanoglasses (1166 MPa) is comparable to the melt-spun ribbons (1183 MPa). HPT-processed nanoglass showed slightly higher yield strength (1344 MPa) compared to as prepared nanoglass. On a whole, the deformation behaviour in Pd-Si metallic nanoglasses is in complete contrast with Cu-Zr metallic nanoglasses where a relatively homogeneous deformation is observed in nanoglasses compared to melt-spun ribbons.

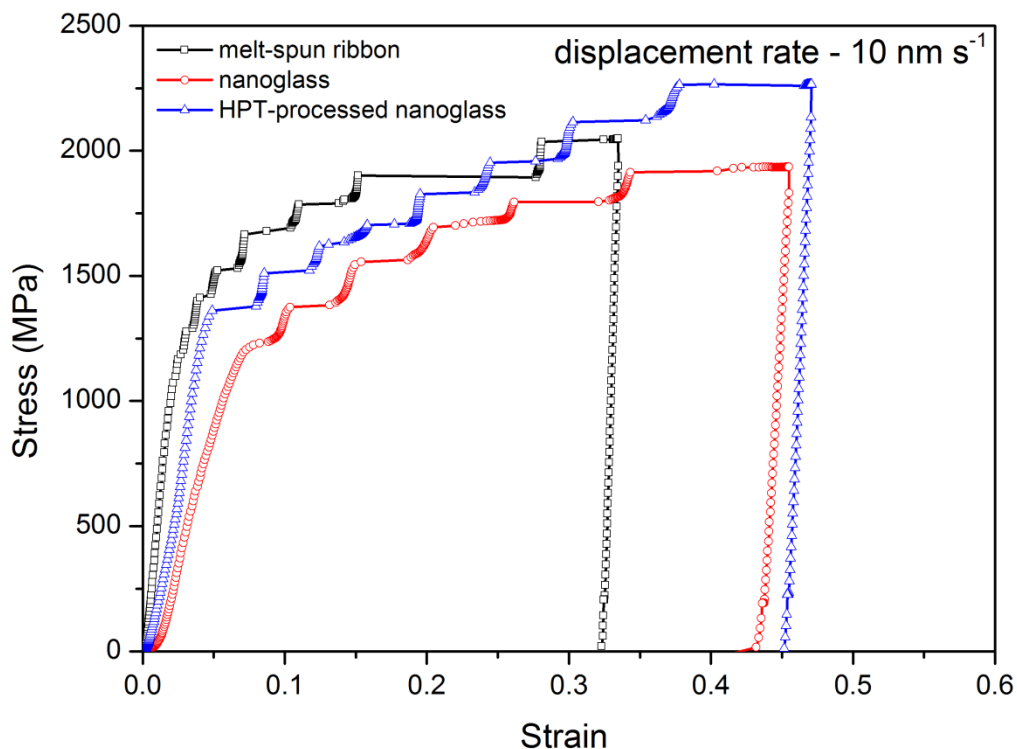


Fig. 6.6 Engineering stress-strain curves obtained from micropillar tests

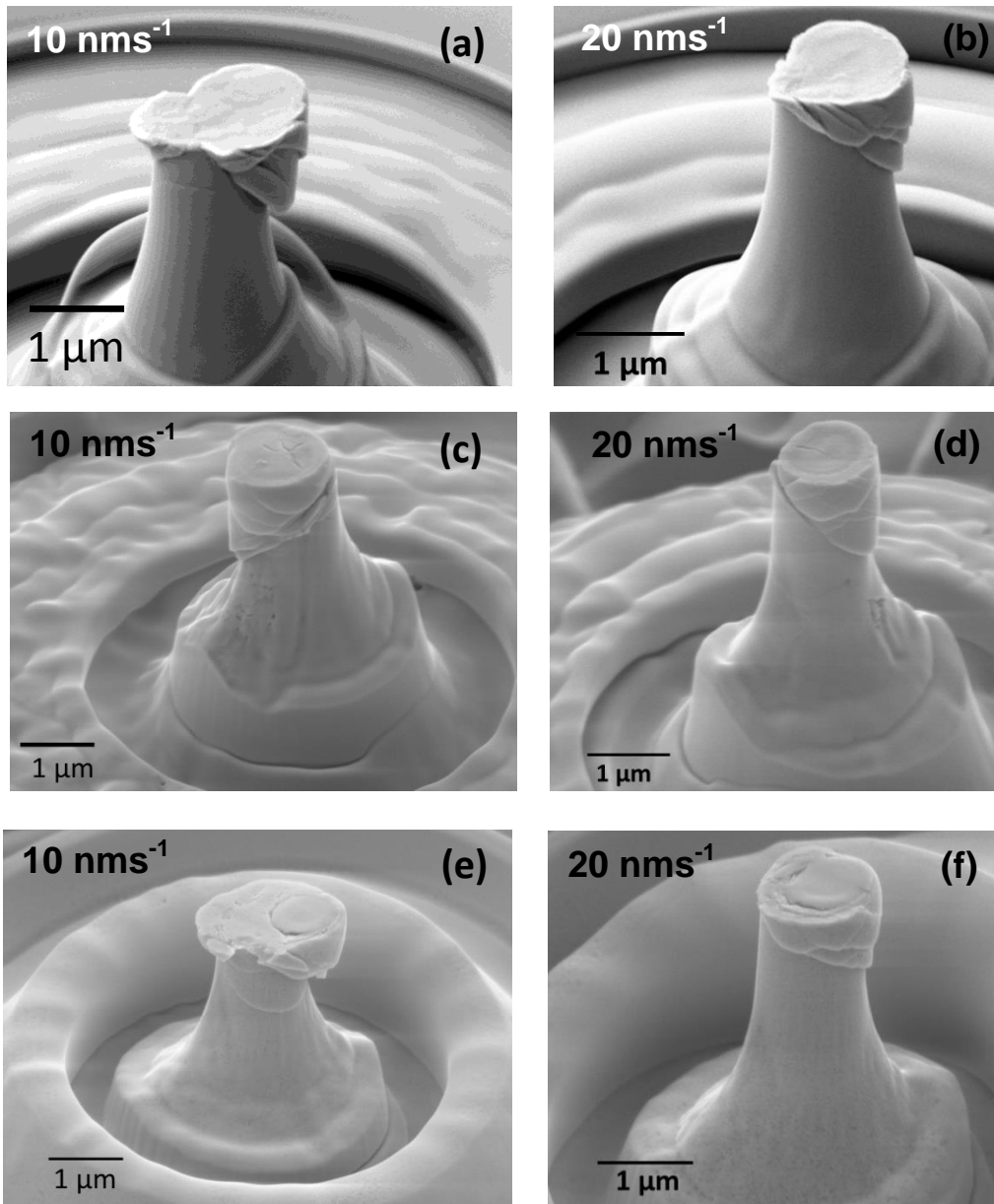


Fig. 6.7 SEM images of tested micropillars at two different displacement rates. $\text{Pd}_{80}\text{Si}_{20}$ melt-spun ribbon at (a) 10 nms^{-1} , (b) 20 nms^{-1} , $\text{Pd}_{84}\text{Si}_{16}$ nanoglass at (c) 10 nms^{-1} , (d) 20 nms^{-1} and $\text{Pd}_{84}\text{Si}_{16}$ HPT-processed nanoglass at (e) 10 nms^{-1} , (f) 20 nms^{-1}

6.6 Comparison with MD simulations

As mentioned earlier in section 2.5 and 2.6, due to the complexity in the structure, it is difficult to gain a comprehensive picture of the deformation behaviour just by experimental methods. In this regard, MD simulations were carried out on Pd-Si nanoglasses to study how the chemical and topological structure influences the deformation behaviour. As a first step, both the metallic glass and nanoglass samples are relaxed by annealing the samples at 600 K

(≈ 0.8 Tg) for 100 ns, due to the high cooling rate and high compaction rate employed during the processing. The variation of the most prominent polyhedra during the annealing of the metallic glass and the nanoglass is monitored and plotted in fig. 6.8(a). Within the first 10 ns of annealing, the fraction of polyhedra in the nanoglass increases significantly and reaches a steady state, while it fluctuates around the same value, which is about 57.5%, in the metallic glass. This rapid increase is attributed to the high compaction rate during preparation of the nanoglass. However, the fraction of polyhedra in the nanoglass is still lower than that of the metallic glass even after annealing for 100 s. This means that the defective short-range order occurred during consolidation cannot fully recover after annealing and consequently the microstructure of the nanoglass is still persisting. In addition, the fraction of polyhedra in the interfaces is the same as that in the glassy regions. This may be due to the high fraction of Pd atoms in $\text{Pd}_{80}\text{Si}_{20}$ nanoglass (80 at.%), which allows the $\text{Si}[0,3,6,0]$ polyhedron to recover [77]. We have focused only on the dominant polyhedra i.e. $\text{Si}[0,3,6,0]$ in the current work since the other low coordination polyhedra are almost the same in number, while $\text{Si}[0,3,6,0]$ decreased by almost 10% in the nanoglass compared to a bulk metallic glass (see fig. S4 in ref. [87]).

To check whether the restructuring of the major polyhedra occurs by atomic diffusion in a long range or simply over a few atomic diameters, we have plotted the variation of the number density as a function of annealing time, which is presented in fig. 6.8(b). Here, number density simply refers to the number of atoms (total number of Pd and Si atoms) per unit volume. It can be seen that the number density of the nanoglass remains below that of the metallic glass. Moreover, it is higher in the glassy regions and lower in the interfaces than that of the metallic glass with the same chemical composition. This change in the number density is due to the difference in the composition between the interfaces and glassy regions, which results from the surface segregation in primary glassy particles [37,38,124]. These results imply that the microstructure of the nanoglass still exists after the annealing.

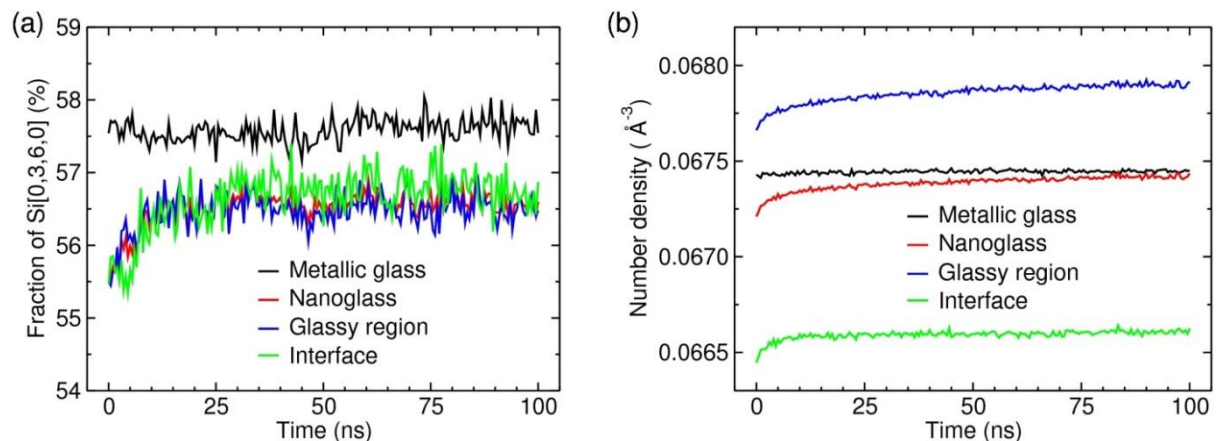


Fig. 6.8 Molecular dynamics results of the annealing of a $\text{Pd}_{80}\text{Si}_{20}$ nanoglass at a temperature of about 600 K ($\approx 0.8\text{Tg}$). (a) Variation of the most prominent Voronoi polyhedra, $\text{Si}[0,3,6,0]$. (b) Number density. Bulk glass with the same chemical composition as the nanoglass is added for comparison.

In the next step, we cut pillars with a diameter of about 36 nm and an aspect ratio (length/diameter) of 2 from as-prepared and samples annealed at 30 and 100 ns (see fig. 3.8). We then tested all the pillars in uniaxial compression at a constant strain rate of $4 \times 10^{-5} \text{ ps}^{-1}$. The atomic scale deformation mechanisms were analyzed in terms of the local atomic von Mises shear strain, η^{Mises} , calculated with the OVITO analysis and visualization software [145]. More simulation details can be found in the experimental section 3.4.

Fig. 6.9(a) shows the engineering stress-strain curves of as-prepared and annealed pillars during uniaxial compressive deformation. In the case of as-prepared samples, it can be clearly seen that the nanoglass pillar exhibits a different behavior than the metallic glass pillar. The metallic glass pillar shows a sudden stress drop at a strain of about 8%, whereas the nanoglass pillar exhibits more uniform deformation behavior. This stress drop eventually results from the formation of a critical shear band [39,78]. In the case of annealed samples, the stress-strain curves for nanoglass and metallic glass pillars look rather similar. All pillars show a sudden stress drop at about the same strain, $\approx 8\%$, suggesting that all pillars fail through shear banding. This is in line with our experimental results where all the samples deformed inhomogeneously by shear band formation. Moreover, it is remarkable that the yield stress of the as prepared nanoglass pillar is significantly lower than that of the metallic glass pillar. The observed reduction in the yield stress in the as prepared nanoglass indicates that deformation behavior is correlated with the fraction of the most prominent Voronoi polyhedra (fig. 6.8(a)).

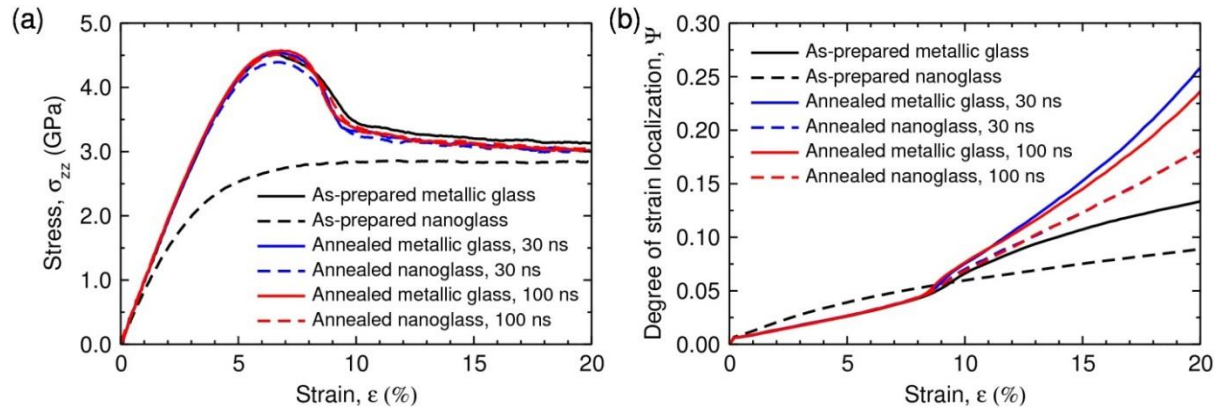


Fig. 6.9 Mechanical response of as-prepared and annealed $\text{Pd}_{80}\text{Si}_{20}$ metallic glass and nanoglass pillars obtained by molecular dynamics simulations. (a) Engineering stress-strain curves and (b) the degree of strain localization parameter, Ψ , during uniaxial compressive deformation

To investigate further the origin of shear bands in Pd-Si nanoglass pillars, we determined the strain localization parameter defined by [80]:

$$\Psi = \sqrt{\frac{1}{N} \sum_{i=1}^N (\eta_i^{\text{Mises}} - \eta_{\text{ave}}^{\text{Mises}})^2}$$

where η_{ave}^{Mises} is the average of von Mises strain of all atoms and N is the total number of atoms. Ψ evaluates the deviation of strain distribution from the homogeneous behavior: a larger Ψ indicates larger fluctuations in the local atomic strain and a more localized deformation mode.

Fig. 6.9(b) presents the variation of the Ψ parameter during uniaxial compressive deformation of the metallic glass and nanoglass pillars. Again, the difference can be clearly seen between the as-prepared nanoglass and metallic glass pillars in the variation of the Ψ parameter during the deformation. However, in the annealed samples, the nanoglass pillars show similar behavior as the metallic glass pillars: the Ψ parameter shows a sudden increase between 8 and 9% total strain.

To get insights into the deformation mechanism of the as-prepared and annealed pillars, we calculated the von Mises shear strain at 20% total strain (Fig. 6.10). In the case of as-prepared samples, shear strain is more homogeneous in the nanoglass pillar as compared to the metallic glass pillar. However, the annealed nanoglass and metallic glass pillars show the same deformation mode: shear strain is localized in a single shear band. This is consistent with the stress drop in the stress-strain curves and a sudden increase in the strain localization parameter (Fig. 6.9(b)). Although annealed nanoglass and metallic glass samples showed shear bands, the von Mises shear strain looks more diffused (delocalized) in the case of nanoglass compared to a metallic glass.

Current simulation results indicate that the plastic deformation in $\text{Pd}_{80}\text{Si}_{20}$ nanoglass pillars is localized in shear bands which was also observed in $\text{Sc}_{75}\text{Fe}_{25}$ nanoglass pillars for large pillar diameters [33,34]. Unlike in Cu-Zr nanoglasses, deformation is more localized in the form of shear bands in Pd-Si nanoglasses. Recent MD simulations on the microstructure formation of $\text{Pd}_{80}\text{Si}_{20}$ and $\text{Cu}_{64}\text{Zr}_{36}$ nanoglasses reveal that the fraction of the most prominent polyhedra is reduced only by about 17% in $\text{Pd}_{80}\text{Si}_{20}$ nanoglass (i.e. $\text{Si}[0,3,6,0]$) while in the $\text{Cu}_{64}\text{Zr}_{36}$ nanoglass (i.e. $\text{Cu}[0,0,12,0]$) is about 40% lower than that of the metallic glass with identical chemical composition [87]. This suggests that the short range order in the $\text{Pd}_{80}\text{Si}_{20}$ nanoglass has the ability to recover faster during annealing than the $\text{Cu}_{64}\text{Zr}_{36}$ nanoglass. This is the reason why we observe shear banding in annealed Pd-Si nanoglasses only after 30 ns. The experimental results from micropillar and nanoindentation tests also indicate that shear band deformation seems to be the most prominent mode in Pd-Si alloys. However, in Cu-Zr alloys, the situation is slightly different. It was already shown by Sopy *et al.* [39] by MD simulations that annealing the nanoglass reduces its plasticity slightly but the stress drop is not significant as the conventional metallic glass. This confirms that the structure of the nanoglass is still retained to a larger extent in Cu-Zr alloys than Pd-Si nanoglasses. It can be explained by the reduction of major polyhedra i.e. $\text{Cu}[0,0,12,0]$, in a significant fraction of about 40% in $\text{Cu}_{64}\text{Zr}_{36}$ nanoglass. It is possible that recovery of the major polyhedra cannot happen to full extent which is the reason for a more homogeneous like deformation during the deformation of $\text{Cu}_{50}\text{Zr}_{50}$ nanoglass. Recent MD simulations and bending results of Cu-Zr and Pd-Si metallic glasses by An *et al.* [77] showed that the cavitation events, which are the reason for

failure in a metallic glass during deformation, are reduced when there is chemical inhomogeneity in the glassy alloy. This also could explain the change in the deformation behavior between Cu-Zr and Pd-Si nanoglasses. Due to the high chemical inhomogeneity in Cu-Zr nanoglasses compared to melt-spun ribbons, it is possible that the Cu-Zr nanoglasses show relatively less catastrophic deformation, while not an obvious change is observed in the deformation behavior of Pd-Si nanoglasses because of less chemical heterogeneity in them. However, this speculation has to be verified by a direct comparison of MD simulations and micropillar tests of $\text{Cu}_{50}\text{Zr}_{50}$ nanoglasses, which will be undertaken in the near future.

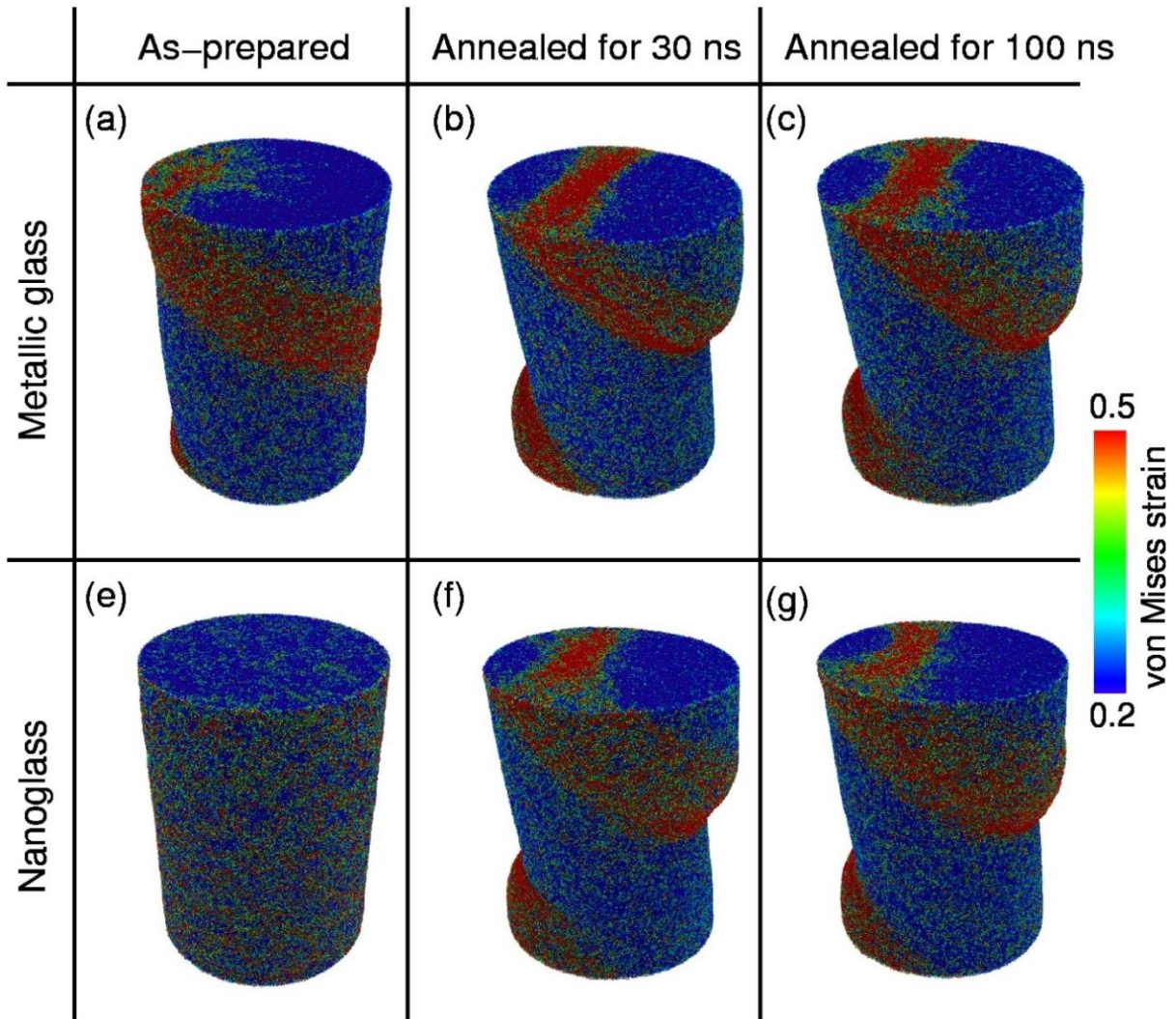


Fig. 6.10 Local atomic von Mises shear strain at 20% total compression strain for the as-prepared and annealed $\text{Pd}_{80}\text{Si}_{20}$ metallic glass and nanoglass pillars for different times (a) & (e) as-prepared, (b) & (f) annealed for 30 ns, (c) & (g).

6.7 Summary

In conclusion, Pd-Si nanoglasses were successfully synthesized by IGC. The samples were found to be completely amorphous, which is evident from the XRD and DSC. Chemical inhomogeneity is found to be less in Pd-Si system compared to Cu-Zr nanoglasses which is also observed in MD simulations. T_g and T_x shifted to lower temperature in nanoglass compared to melt-spun ribbons. The reason for such a decrease is speculated to be the Si rich core and Pd-rich interfaces in nanoglasses. DSC results also showed less enthalpy for crystallization reaction in nanoglasses compared to melt-spun ribbons, which is consistent with the results obtained in Cu-Zr nanoglasses. The activation energy for the crystallization reaction showed similar values for both nanoglass and melt-spun ribbons. Nanoindentation tests showed serrations (pop-ins) in the melt-spun ribbon as well as nanoglasses. Low Young's modulus values are found in the nanoglass samples compared to melt-spun ribbon which is predicted to be because of the increase in Pd-Pd metallic bonds due to the chemically inhomogeneous nanostructure. Uniaxial compression tests of micropillars showed deformation by shear band formation in both metallic glasses and nanoglasses. MD simulations clearly showed that the major Si centered polyhedra Si[0,3,6,0] is found to be the determining factor in shear band formation in both metallic glasses and nanoglasses. The increase in the fraction of major polyhedra in the nanoglass to almost the level of conventional rapid quenched metallic glass increased the propensity of shear band formation.

7. Mechanical properties and crystallization of Pd-Si nanoglass films synthesized by magnetron sputtering

In this chapter sputtered films, which have a nanograined columnar structure, referred to as nanoglasses in literature are synthesized by using magnetron sputtering. The crystallization behaviour and the mechanical properties of the thin films are studied and described in detail. The reasons for the structure and properties as well as some unanswered questions in this study will be addressed in this chapter.

7.1 Structural characterization of thin films

Thin films with a composition of Pd₈₀Si₂₀ are synthesized by co-sputtering elementally pure Pd and Si targets. The details of the synthesis are already discussed in section 3.1.2. Preliminary sputtering experiments were optimized to make an amorphous structure without any crystalline phase. To determine the composition by SEM-EDS, the first few samples were sputtered on kapton substrates to avoid the Si signal from substrate. Initial sputtering experiments produced a crystalline film of Pd₉₀Si₁₀ composition (see fig. 7.1(a)). By changing the sputtering power, a completely amorphous structure was obtained. The composition of the film was found to be Pd₈₀Si₂₀ by SEM-EDS. For one sample, RBS measurement confirmed the composition determined by SEM-EDS. The microstructure of the top surface of the film was observed in SEM and it showed granular morphology with a grain size of approximately 30-50 nm as seen in fig. 7.1(b). Similar grain sizes were also observed by Chen *et al.* [31] in a Au-based films while lower grain sizes were observed in Ni₅₀Ti₄₅Cu₅ (~ 8 nm) nanoglassy thin films [32]. The cross section of the film showed that the grains grew as columns on the substrate as seen in fig. 7.1(c). The reason for such columnar growth is the oblique angle deposition which results in a shadowing effect during the deposition [32,89]. Initially, nucleation of small clusters in the form of islands happens on the substrate upon which further growth proceeds on them. Due to the oblique angle deposition and low diffusivity of atoms, the islands, which form initially, can grow further shadowing at the same time the neighbouring regions. Eventually, upon further growth, the columns come into contact with each other but the structure is still retained. Such columnar morphology was commonly observed in both crystalline and amorphous thin films [89,146]. Several intricate structures like zig zag, dendritic, spiral columns etc., are possible during oblique angle deposition in sputtering [146]. The interfacial regions in these structures are characterized by extensive porosity and low density compared to the interior of the column [89]. Bright and dark contrast regions were observed in TEM because of the density differences between the centre and the interfacial region of the Au-based nanoglass thin films [31,147]. Indeed a relative density of 94 % was measured by standard Archimedes principle and it was speculated that 6 % contributes to the free volume in the sample.

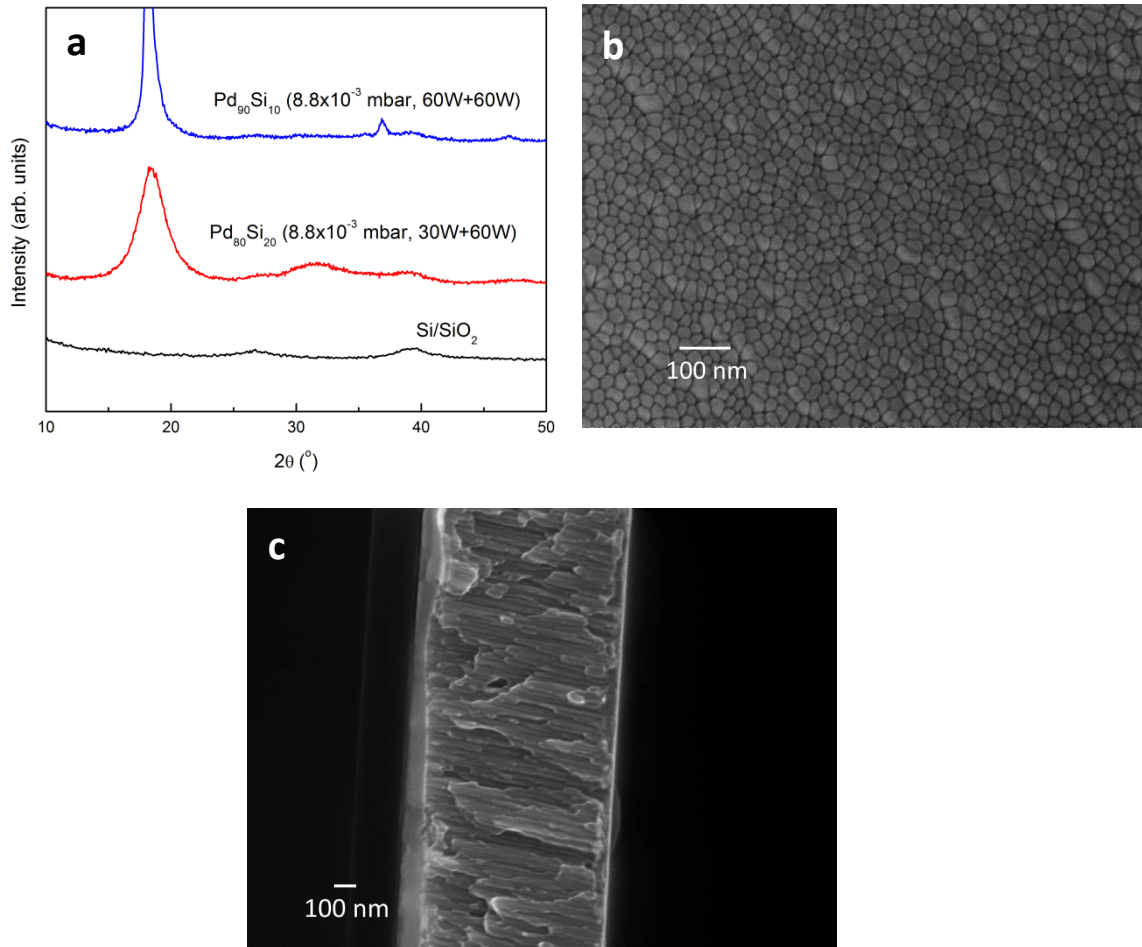


Fig. 7.1 (a) XRD of (top) 60 W Pd + 60 W Si sputtered thin film (middle) 30 W Pd + 60 W Si sputtered thin film and (bottom) Si substrate, (b) SEM image of the top surface of the thin film and (c) cross-section of the thin film showing columnar morphology

TEM is performed on the thin films by directly depositing on the carbon coated copper grid. The samples were transferred directly in air with no capping layer protection. In spite of that, a rather small amount of oxygen, less than 2 at.% was observed in the samples. The amorphous nature of the films was evident from fig. 7.2(a) & (b). HRTEM images of the films confirmed the amorphous nature at nanoscale as shown in fig. 7.2(b). White regions observed in fig. 7.2(a) are the gaps between the islands with no material deposition. This is because of the low deposition thickness, i.e. ~ 20-30 nm, necessary for TEM observation. No compositional heterogeneity was observed as shown in fig. 7.2(c)-(e). It is clear from fig. 7.2(c)-(e) that Pd and Si are uniformly distributed in the sample with no preferential segregation at the interfaces, which is also consistent with the nanoglasses synthesized by IGC (see fig. 6.2) and the results by MD simulations. In contrast, Sniadecki *et al.* [32] recently observed segregation of Ti to the boundary regions in $\text{Ni}_{50}\text{Ti}_{45}\text{Cu}_5$ nanoglass thin films and Na *et al.* [31] reported no segregation in Au based alloys. As mentioned in section 6.3, elemental segregation is only of the order of ~3% in Pd-Si amorphous nanoparticles by MD simulations [37]. It is possible that such small changes in composition in nanometric regime are not easily distinguishable in the elemental map of a TEM.

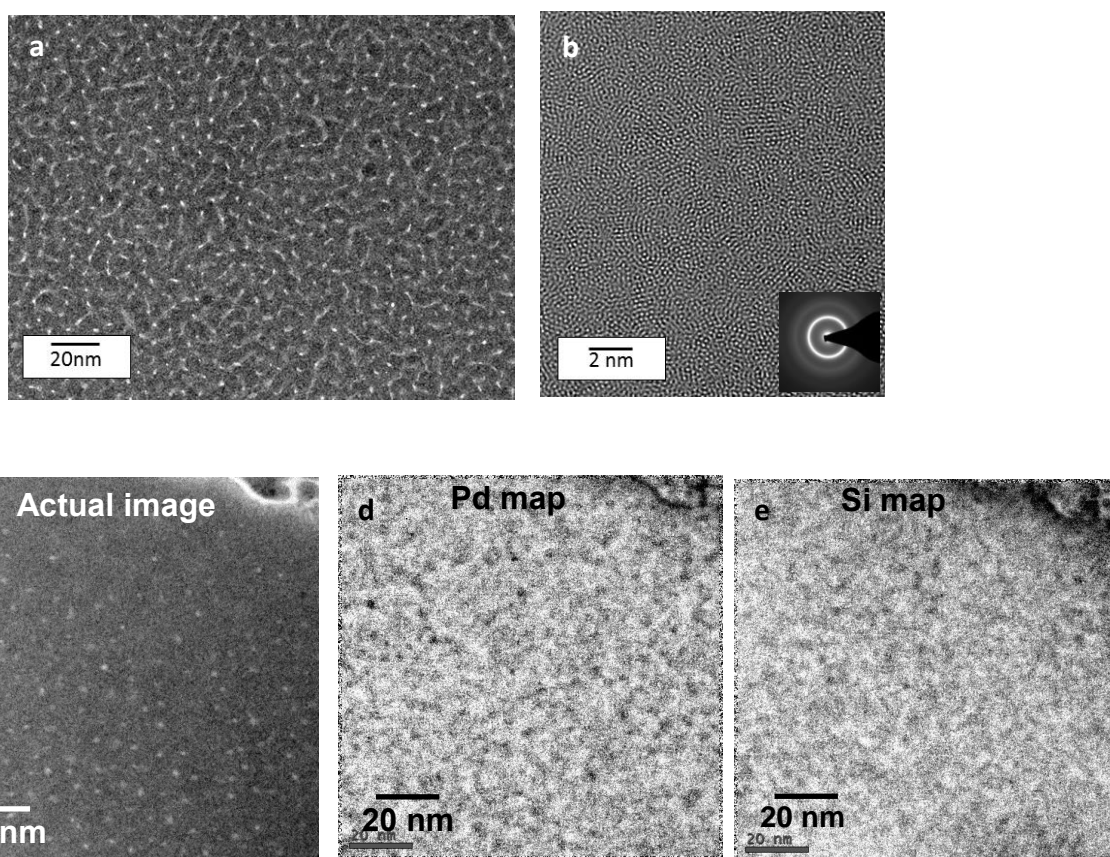


Fig. 7.2 (a) TEM image of thin film white regions are gaps between the island regions (b) HRTEM image confirming the amorphous nature and inset showing the diffraction pattern, (c) TEM image where the elemental maps were obtained, (d) Pd map and (e) Si map showing uniform distribution with no obvious elemental segregation.

7.2 Thermal stability of thin film nanoglasses

To test the thermal stability of thin films, the samples were heated in a tubular furnace under Ar atmosphere at different temperatures for various times. It was found that the thin film samples crystallized at a temperature of 400 °C when the annealing time is 2 h while it crystallized at a temperature of 250 °C for long annealing times of 24 h as shown in fig. 7.3(a). It must be pointed out that the Ar gas flow is decreased for long duration annealing. In every experiment, the tube is pre-flown with Ar gas for 30 mins to remove any gaseous impurities, most of all, oxygen. The crystallized phases were found to be Pd and Pd₃Si which are the equilibrium phases in Pd-Si phase diagram for short anneals while only Pd peaks were observed for longer anneals. Faint traces of Pd₂Si were also observed for shorter anneal samples. It was already observed that Pd₈₀Si₂₀ melt-spun ribbons crystallize at around 390 °C in a DSC (see fig. 6.1). Crystallization of the melt-spun ribbons also started at 250 °C during longer anneals as shown in fig. 7.3 (b). As can be clearly seen, only Pd peaks were observed in the long anneals of melt-spun ribbons. However, there seems to be a significant amount of amorphous content still left in the melt-spun ribbon sample after 24 h of annealing while thin

film samples seemed to be completely crystallized. This indicates that the thin film nanoglasses are thermally less stable when compared to the conventional metallic glasses. Similar results were also observed in the nanoglasses synthesized by IGC, i.e. nanoglasses show less T_g compared to melt-spun ribbons (see table 6.1), which seems to indicate that vapour deposition leads to similar structural features. To convincingly prove this point, one has to employ DSC measurements on the thin film samples. The more interesting observation is that the size of nanograins did not change during annealing of the films as shown in fig. 7.4. Even annealing for longer duration of times like 24 h at 300 °C and crystallization of the film at 400 °C did not change the morphology of the films. Unlike Pd-Si nanoglasses, enhanced thermal stability is reported for the Au based nanoglass thin films compared to the BMG of a similar composition. Similar to the results presented here, it was also found that the interface did not delocalize during the annealing process. By using HRTEM, it was also observed that the crystallization started from the centre of the nanograins. It was concluded that deposited Au based nanograined thin films seemed to attain their ultrastable character because of the stability of the interfaces [36]. However, one would expect that the regions with a reduced density (regions of high free volume) in an amorphous structure rearrange to a dense structure during annealing, which would result in grain growth of the thin films, but no such coarsening of grains can be observed. The effect of chemical segregation on the stability of the interface is not considered while discussing Au based nanoglass thin films. This crystallization behavior is not completely understood and requires further research to clarify the thermal behavior of nanoglass thin films.

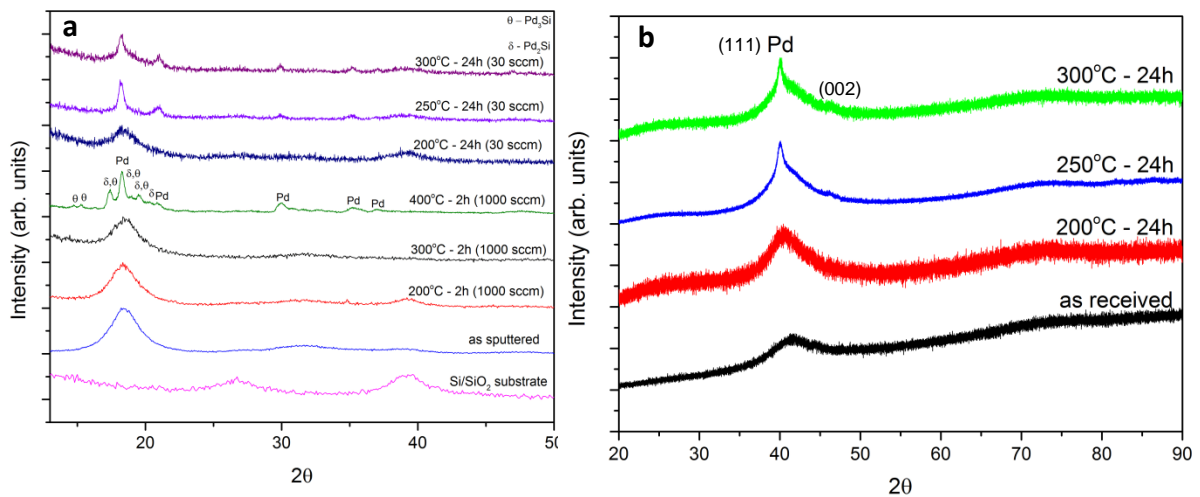


Fig. 7.3 (a) XRD of as-sputtered film and the annealed samples at 200, 300 and 400 °C at 2 and 24 h and (b) XRD of melt-spun ribbons annealed at different temperatures

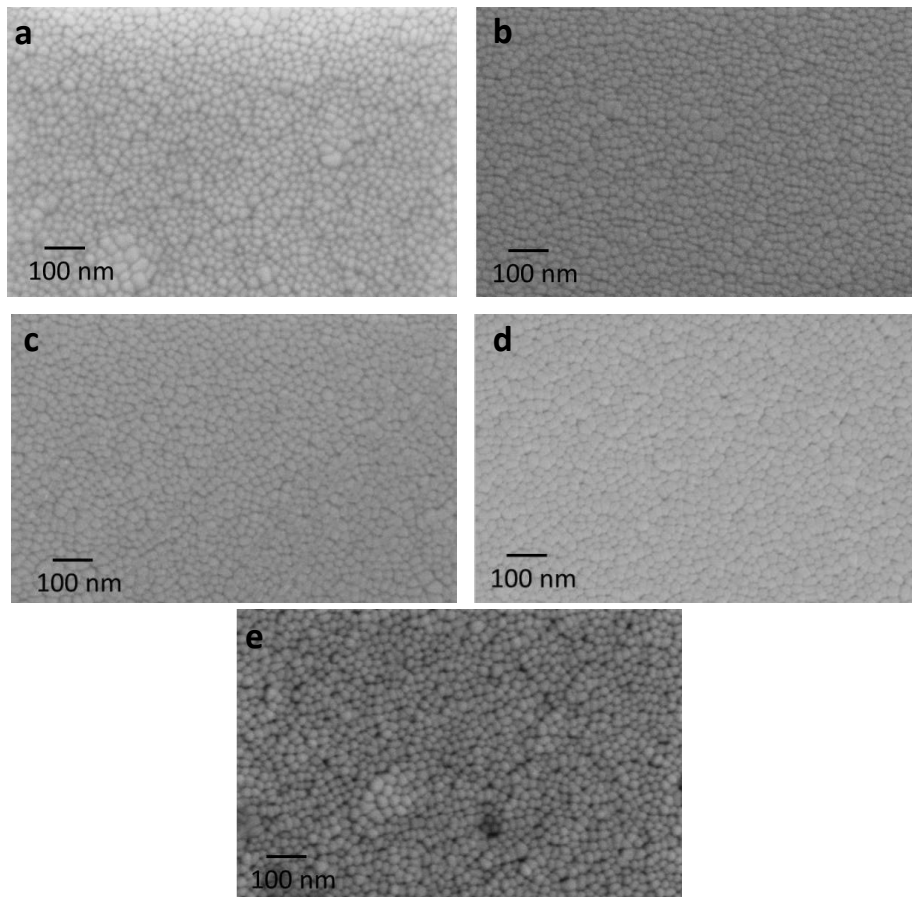


Fig. 7.4 SEM images of (a) as sputtered thin film, annealed thin film at (b) 200 °C for 2 h, (c) 300 °C for 2 h, (d) 400 °C for 2 h and (e) 300 °C for 24 h

7.3 Mechanical behaviour of sputtered nanoglasses

Testing the mechanical behaviour of such nanograined thin films is one of the primary objectives of this study. To do this, nanoindentation was performed at different indentation depths and strain rates to understand the deformation behaviour. A representative load – displacement curve at four different strain rates up to a depth of 50 nm is shown in fig. 7.5(a). It is evident that there are no distinctive serrations or pop-ins like in melt-spun ribbons. The small kinks in the load-displacement curve at high strain rates are the artifacts from the measurement. Even the SEM images did not show any shear bands around the indent (see fig. 7.5(b)). But when the indentation depth is increased to 500 nm, shear bands were observed around the indent as shown in fig. 7.5(c). Such a change in mode of deformation is because of the size dependent deformation in Pd-Si metallic glasses [144,148]. It was already shown by means of microcompression tests that homogeneous deformation was observed if the diameter of the pillar is less than 500 nm. With increase in indentation strain rate, slight increase in modulus and hardness were observed. Hardness of the thin film nanoglasses is 6.4 ± 0.2 GPa and Young's modulus is found to be 112.1 ± 2.5 GPa (assuming a Poisson's ratio of 0.41) at a strain rate of 0.05 s^{-1} . The above values were estimated at 100 nm indentation

depth so that the tested volume does not exceed 10% of the film thickness. The hardness and modulus values obtained in the nanoglass thin films are considerably higher than the values for melt-spun ribbons. Similarly, high values of hardness and modulus were also observed for Au-based nanoglass thin films by nanoindentation [31]. However, the effect of the substrate tends to overestimate the modulus and hardness values in thin films during nanoindentation tests. The increase in modulus and hardness values in the present Pd-Si nanoglass thin films can simply be an effect of the substrate.

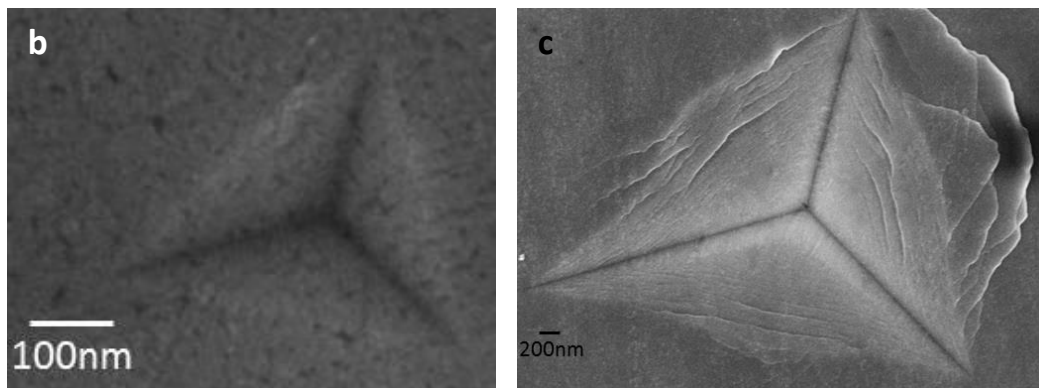
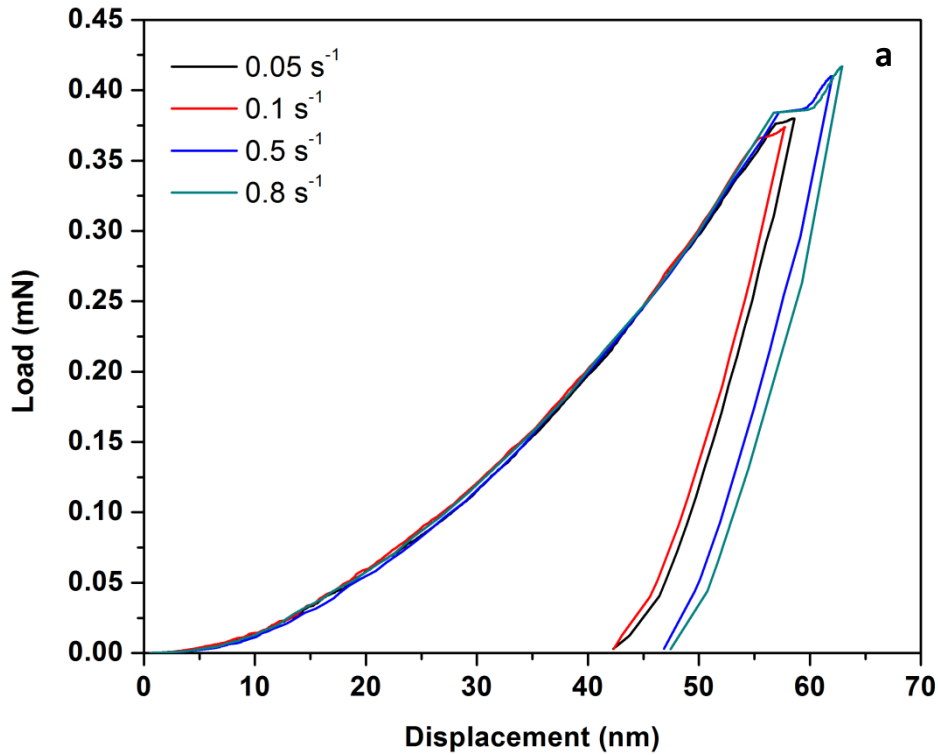


Fig. 7.5 (a) Nanoindentation load-displacement curves at different indentation strain rates for a depth of 50 nm, SEM images of nanoindent at an (b) indentation strain rate of 0.05 s^{-1} for a depth of 50 nm and (c) indentation strain rate of 0.05 s^{-1} for a depth of 800 nm

To confirm the deformation behaviour, micropillar tests were carried out on Pd-Si thin film samples with $\sim 1 \mu\text{m}$ in diameter. The diameter was chosen to avoid the size dependent deformation behaviour [148]. A representative load displacement curve is shown in fig. 7.6(a) and it is clear from the figure that the deformation progresses by shear band formation. Each step in the curve represents a new operating shear band. A representative curve of melt-spun ribbons of the same composition is also shown in fig 7.6(a) for comparison. SEM images of the tested micropillars showed shear band as shown in fig. 7.6(b). Such localized deformation seems to conclude that thin film metallic nanoglasses behave similar to conventional metallic glasses. One should also consider that the grains observed in the present microstructure are columnar, which would mean that there are less interfacial regions in a micron size sample whereas the grains in the nanoglasses synthesized by IGC are spherical, i.e., more grains for the same thickness. So, spherical grains of the size of the IGC particles would probably be more influential in the mechanical properties of such thin films.

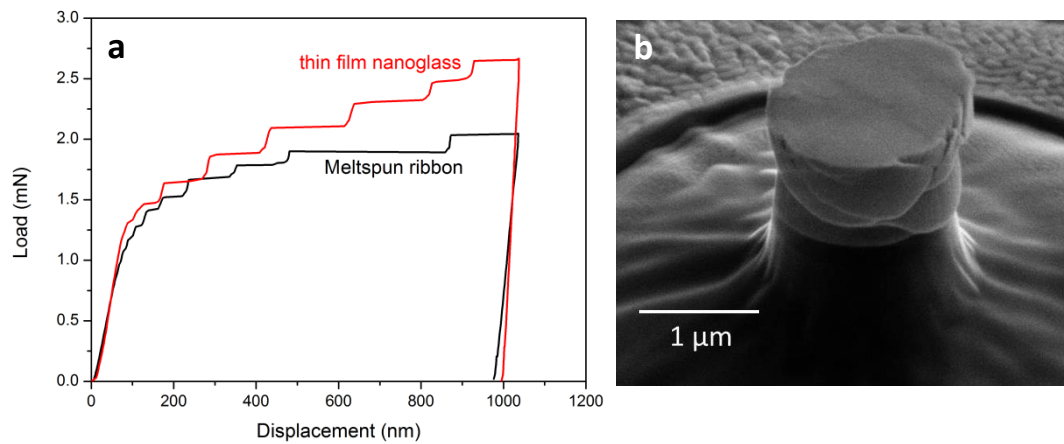


Fig. 7.6 (a) Load-displacement curve of Pd-Si sputtered nanoglass and melt-spun ribbon and (b) SEM image of a compressed micropillar showing shear bands

7.4 Summary

As a conclusion, the structural characterization of the thin film nanoglasses showed that the samples are amorphous with columnar grains. No significant segregation of elements was observed by TEM, which is consistent with Pd-Si nanoglasses synthesized by IGC. Annealing of thin films clearly showed no change in the nanostructure of the sample even after crystallization. Mechanical characterization of the thin film samples showed shear band deformation like in conventional metallic glasses. The results obtained by annealing and mechanical tests seemed to be very similar to samples synthesized by IGC. As already shown in section 5.4, deformation behavior is strongly influenced by the chemical inhomogeneity in Cu-Zr sample. An alloy like NiTiCu [32], which showed strong segregation behaviour would probably show completely different mechanical behaviour compared to the present Pd-Si alloys. Further tests on glassy thin films with different chemical composition would give a more conclusive picture.



8. Conclusions and Outlook

8.1 Conclusions

Nanoglasses synthesized by IGC: Nanoglasses of several compositions such as $\text{Cu}_{50}\text{Zr}_{50}$, $\text{Cu}_{60}\text{Zr}_{40}$, $\text{Pd}_{84}\text{Si}_{16}$ are successfully synthesized by using magnetron sputtering in IGC. Structural characterization confirmed that all the samples are amorphous in nature. Elemental segregation is observed in Cu-Zr alloys while it is found to be less in Pd-Si nanoglasses. This segregation behaviour is consistent with MD simulation results [37]. DSC showed contrasting results in Cu-Zr and Pd-Si nanoglasses compared to the respective melt-spun ribbons. Glass transition is observed in Pd-Si nanoglasses while it is not so prominent in Cu-Zr nanoglasses. The crystallization temperature is higher in Cu-Zr alloys while it is lower in Pd-Si nanoglasses compared to the corresponding melt-spun ribbons. Both Cu-Zr and Pd-Si nanoglasses showed a reduction in the enthalpy of crystallization reaction, which is predicted to arise from the relaxed nature of the nanoglasses compared to the rapidly quenched glasses. The activation energy for crystallization reaction is higher in Cu-Zr nanoglasses while it is almost comparable in Pd-Si nanoglasses compared to melt-spun ribbons of a similar composition. By combining experiments and MD simulations, a segregation model with a relaxed Zr or Si-rich core and Cu or Pd-rich interfaces is proposed explaining the observed DSC results.

Indentation properties of Cu-Zr nanoglasses showed slightly higher modulus and hardness values, while these values decreased in Pd-Si nanoglasses compared to the respective melt-spun ribbons. Such a change in values is found to arise both from the elemental segregation as well as the bonding of the elemental constituents. The presence of Pd-rich interfaces in the nanoglasses probably decreased the elastic modulus in the nanoglass compared to the melt-spun ribbons. The deformation behavior is found to be significantly affected by the chemical inhomogeneity in the sample. This was verified by nanoindentation as well as micropillar tests. Deformation is found to be less catastrophic in Cu-Zr nanoglasses while the corresponding melt-spun ribbons deformed by catastrophic shear band formation. However, shear band formation is observed in both Pd-Si nanoglasses and melt-spun ribbons. This can be attributed to the higher chemical inhomogeneity of Cu-Zr alloys compared to Pd-Si nanoglasses. The reason for the similar deformation behavior in Pd-Si metallic glasses and nanoglasses is explored by MD simulations. It clearly showed that the volume fraction of Si major polyhedra i.e. $\text{Si}[0,3,6,0]$ in nanoglasses increased to almost the level of conventional metallic glasses within the first 10 ns of relaxation. This increase in the fraction of the major Si polyhedra increased the propensity of shear band formation in Pd-Si nanoglasses.

Nanoglass films synthesized by magnetron sputtering: The major observations made using the sputtered Pd-Si nanoglass thin films are the following: Samples are found to be completely amorphous as evidenced by XRD and TEM. Columnar microstructure is observed in the cross-section of the film. No significant elemental segregation is observed in the thin films similar to nanoglasses synthesized by IGC. Thermal behavior of the films is studied by annealing them in Ar atmosphere and it is found that the nanoglasses are less stable compared to melt-spun ribbons which is also consistent with nanoglasses synthesized by IGC. Elastic modulus and hardness of thin films were found to be higher than the melt-spun ribbon which is probably due to the small thickness of the material tested and the influence of the substrate. Shear band formation is observed in sputtered films similar to melt-spun ribbons and nanoglasses synthesized by IGC.

As a final point, chemical inhomogeneity seems to play an important role in determining the physical properties of nanoglasses. Along with the free volume at the interfacial regions, such chemical inhomogeneities could significantly influence the mechanical properties like elastic modulus, plasticity and deformation mode in nanoglasses. Recently, it was observed that Ni-rich regions in the interfaces of Ni-Ti nanoglass (amorphous nanostructure) made it ferromagnetic, while a homogeneous film prepared by magnetron sputtering is paramagnetic in nature [149]. By tailoring the chemistry of the interfaces, it is possible to change the properties of nanoglasses.

8.2 Outlook

Although the present thesis provided an analysis on the structural and physical properties of nanoglasses, there are still un-answered questions, which are not dealt in the current work.

1. Improving the ductility in metallic glasses has been a long standing problem. The important question to be addressed is: Can plasticity be improved in every nanoglass system? If so, how much will be the enhancement in ductility compared to a conventional rapidly quenched alloy? Pd-Si is an alloy with high Poisson's ratio of about 0.4, which is naturally more ductile than many other glass forming systems. As pointed out in this thesis, ductility improvement is not so significant in Pd-Si nanoglasses compared to conventional metallic glasses. Since there is more chemical inhomogeneity in Cu-Zr nanoglasses at nanoscale compared to melt-spun ribbons, plasticity is enhanced in Cu-Zr nanoglasses. In this regard, it would be better to test the mechanical properties of a few more glass forming systems like $\text{Fe}_{80}\text{B}_{20}$, $\text{Ni}_{60}\text{Nb}_{40}$ etc. to understand the deformation behavior in nanoglasses.
2. Another possible advantage with the current synthesis method by IGC is that several metastable structures, which are difficult to prepare by conventional means can be made possible because of the high cooling rates. One such possibility is already demonstrated recently by mixing elements with positive enthalpies of mixing (like Fe

and Cu) into a glassy composition [150]. This could lead to some interesting properties. For argument's sake, if we assume that one of the elements gets segregated preferentially to the interface because of the positive enthalpy of mixing, then during the compaction it is possible to have a complete phase separated nanostructure or crystalline precipitates at the interfacial regions, which could improve the plasticity in metallic glasses. It is already well known that by having crystalline phases at a certain separation distance in glassy matrix, one can improve even the tensile plasticity in a metallic glass. So, it is possible to synthesize such composite nanostructures with some new and interesting properties.

3. Similarly, one can also make amorphous/crystalline composites (like a-Cu-Zr and Cu) or multi-component amorphous composites (like a-Cu-Zr and a-Pd-Si) by co-sputtering to make composite nanoglasses. It is possible that such composite nanostructures can have better plastic deformability compared to the single component nanoglass.
4. As observed in the current work, the presence of elemental segregation in such nanostructured materials can define their physical properties. If so, is there a preferential size limit for segregation in the nanoparticle? To test this, one can synthesize amorphous nanopowders of a larger size, say 100 nm by synthesis routes like mechanical alloying and then characterize their structure and physical properties.
5. To understand the importance of chemical segregation on the deformation ability of Cu-Zr nanoglasses, homogeneous and heterogeneous glassy spheres will be used to synthesize nanoglasses in MD simulations. Later, compression tests will be performed on the processed homogeneous and heterogeneous nanoglasses. Hence, one can comment on the importance of chemical and topological order in the interfacial regions on the mechanical properties of nanoglasses.



References

- [1] W. Klement, R.H. Willens, P. Duwez, Non-crystalline Structure in Solidified Gold–Silicon Alloys, *Nature*. 187 (1960) 869–870. doi:10.1038/187869b0.
- [2] A. Inoue, High Strength Bulk Amorphous Alloys with Low Critical Cooling Rates, *Mater. Trans. JIM*. 36 (1995) 866–875. doi:10.2320/matertrans1989.36.866.
- [3] A. Inoue, Stabilization of metallic supercooled liquid and bulk amorphous alloys, *Acta Mater*. 48 (2000) 279–306. doi:10.1016/S1359-6454(99)00300-6.
- [4] D.B. Miracle, D. V Louzguine-Luzgin, L. V Louzguina-Luzgina, A. Inoue, An assessment of binary metallic glasses: correlations between structure, glass forming ability and stability, *Int. Mater. Rev.* 55 (2010) 218–256. doi:10.1179/095066010X12646898728200.
- [5] E. Ma, Tuning order in disorder, *Nat. Mater.* 14 (2015) 547–552. doi:10.1038/nmat4300.
- [6] W.H. Wang, J.J. Lewandowski, A.L. Greer, Understanding the Glass-forming Ability of $\text{Cu}_{50}\text{Zr}_{50}$ Alloys in Terms of a Metastable Eutectic, *J. Mater. Res.* 20 (2005) 2307–2313. doi:10.1557/jmr.2005.0302.
- [7] Greer A.L., *Metallic Glasses*, *Science* (80-.). 267 (1995) 1947–1953. doi:10.1126/science.267.5206.1947.
- [8] A. Inoue, B. Shen, H. Koshiba, H. Kato, A.R. Yavari, Cobalt-based bulk glassy alloy with ultrahigh strength and soft magnetic properties, *Nat. Mater.* 2 (2003) 661–663. doi:10.1038/nmat982.
- [9] J.J. Lewandowski, A.L. Greer, Temperature rise at shear bands in metallic glasses, *Nat. Mater.* 5 (2006) 15–18. doi:10.1038/nmat1536.
- [10] Y. Zhang, W.H. Wang, A.L. Greer, Making metallic glasses plastic by control of residual stress, *Nat. Mater.* 5 (2006) 857–860. doi:10.1038/nmat1758.
- [11] B.S. Murty, M. Mohan Rao, S. Ranganathan, Milling maps and amorphization during mechanical alloying, *Acta Metall. Mater.* 43 (1995) 2443–2450. doi:10.1016/0956-7151(94)00402-1.
- [12] M.M. Trexler, N.N. Thadhani, Mechanical properties of bulk metallic glasses, *Prog. Mater. Sci.* 55 (2010) 759–839. doi:10.1016/j.pmatsci.2010.04.002.
- [13] C.A. Schuh, T.C. Hufnagel, U. Ramamurty, Mechanical behavior of amorphous alloys, *Acta Mater.* 55 (2007) 4067–4109. doi:10.1016/j.actamat.2007.01.052.
- [14] W.H. Wang, C. Dong, C.H. Shek, Bulk metallic glasses, *Mater. Sci. Eng. R Reports*. 44 (2004) 45–90. doi:10.1016/j.mser.2004.03.001.
- [15] N. Chen, K.F. Yao, F. Ruan, Microstructural features of phase transformation in a binary Pd-Si metallic glass, *Philos. Mag. Lett.* 87 (2007) 677–686. doi:10.1080/09500830701441905.
- [16] Y.T. Shen, L.Q. Xing, K.F. Kelton, Formation and crystallization of ZrCuTi metallic glasses, *Philos. Mag.* 85 (2005) 3673–3682. doi:10.1080/14786430500156724.
- [17] L. Xia, S.T. Shan, D. Ding, Y.D. Dong, Binary bulk metallic glass $\text{Ni}_{62}\text{Nb}_{38}$ with high compressive strength of 3100 MPa, *Intermetallics*. 15 (2007) 1046–1049.

- doi:10.1016/j.intermet.2006.12.008.
- [18] Y. Xu, J. Fang, H. Gleiter, H. Hahn, J. Li, Quantitative determination of free volume in Pd₄₀Ni₄₀P₂₀ bulk metallic glass, *Scr. Mater.* 62 (2010) 674–677. doi:10.1016/j.scriptamat.2010.01.025.
- [19] M.F. Ashby, A.L. Greer, Metallic glasses as structural materials, *Scr. Mater.* 54 (2006) 321–326. doi:10.1016/j.scriptamat.2005.09.051.
- [20] W. Zhang, A. Inoue, X.M. Wang, Developments and Applications of Bulk Metallic Glasses, *Rev. Adv. Mater. Sci.* 18 (2008) 1–9.
- [21] D.C. Hofmann, J.-Y. Suh, A. Wiest, G. Duan, M.-L. Lind, M.D. Demetriou, W.L. Johnson, Designing metallic glass matrix composites with high toughness and tensile ductility, *Nature*. 451 (2008) 1085–1089. doi:10.1038/nature06598.
- [22] V.Y. Slesarenko, D. a Gunderov, P.G. Ulyanov, R.Z. Valiev, Formation of amorphous states in Ti 50 Ni 25 Cu 25 alloy subjected to severe plastic deformation: Nanoglass issue, *IOP Conf. Ser. Mater. Sci. Eng.* 63 (2014) 12166. doi:10.1088/1757-899X/63/1/012166.
- [23] Y.B. Wang, D.D. Qu, X.H. Wang, Y. Cao, X.Z. Liao, M. Kawasaki, S.P. Ringer, Z.W. Shan, T.G. Langdon, J. Shen, Introducing a strain-hardening capability to improve the ductility of bulk metallic glasses via severe plastic deformation, *Acta Mater.* 60 (2012) 253–260. doi:10.1016/j.actamat.2011.09.026.
- [24] Y.H. Liu, G. Wang, R.J. Wang, D.Q. Zhao, M.X. Pan, W.H. Wang, Super Plastic Bulk Metallic Glasses at Room Temperature, *Science* (80-.). 315 (2007) 1385–1388. doi:10.1126/science.1136726.
- [25] J. He, I. Kaban, N. Mattern, K. Song, B. Sun, J. Zhao, D.H. Kim, J. Eckert, A.L. Greer, Local microstructure evolution at shear bands in metallic glasses with nanoscale phase separation, *Sci. Rep.* 6 (2016) 1–8. doi:10.1038/srep25832.
- [26] H. Gleiter, Nanoglasses: A New Kind of Noncrystalline Material and the Way to an Age of New Technologies?, *Small*. 12 (2016) 2225–2233. doi:10.1002/sml.201500899.
- [27] H. Gleiter, Are there ways to synthesize materials beyond the limits of today?, *Metall. Mater. Trans. A Phys. Metall. Mater. Sci.* 40 (2009) 1499–1509. doi:10.1007/s11661-009-9848-7.
- [28] J. Jing, A. Kramer, R. Birringer, H. Gleiter, U. Gonser, Modified atomic structure in a Pd-Fe-Si nanoglass, *J. Non. Cryst. Solids*. 113 (1989) 167–170.
- [29] J.X. Fang, U. Vainio, W. Puff, R. Würschum, X.L. Wang, D. Wang, M. Ghafari, F. Jiang, J. Sun, H. Hahn, H. Gleiter, Atomic Structure and Structural Stability of Sc 75 Fe 25 Nanoglasses, *Nano Lett.* 12 (2012) 458–463. doi:10.1021/nl2038216.
- [30] R. Witte, T. Feng, J.X. Fang, A. Fischer, M. Ghafari, R. Kruk, R.A. Brand, D. Wang, H. Hahn, H. Gleiter, Evidence for enhanced ferromagnetism in an iron-based nanoglass, *Appl. Phys. Lett.* 103 (2013). doi:10.1063/1.4818493.
- [31] N. Chen, R. Frank, N. Asao, D. V. Louzguine-Luzgin, P. Sharma, J.Q. Wang, G.Q. Xie, Y. Ishikawa, N. Hatakeyama, Y.C. Lin, M. Esashi, Y. Yamamoto, A. Inoue, Formation and properties of Au-based nanograin metallic glasses, *Acta Mater.* 59 (2011) 6433–6440. doi:10.1016/j.actamat.2011.07.007.
- [32] Z. Sniadecki, D. Wang, Y. Ivanisenko, V.S.K. Chakravadhanula, C. Kübel, H. Hahn,

-
- H. Gleiter, Nanoscale morphology of Ni₅₀Ti₄₅Cu₅ nanoglass, *Mater. Charact.* 113 (2016) 26–33. doi:10.1016/j.matchar.2015.12.025.
- [33] X.L. Wang, F. Jiang, H. Hahn, J. Li, H. Gleiter, J. Sun, J.X. Fang, Plasticity of a scandium-based nanoglass, *Scr. Mater.* 98 (2015) 40–43. doi:10.1016/j.scriptamat.2014.11.010.
- [34] X. Wang, F. Jiang, H. Hahn, J. Li, H. Gleiter, J. Sun, J. Fang, Sample size effects on strength and deformation mechanism of Sc₇₅Fe₂₅ nanoglass and metallic glass, *Scr. Mater.* 116 (2016) 95–99. doi:10.1016/j.scriptamat.2016.01.036.
- [35] O. Franke, D. Leisen, H. Gleiter, H. Hahn, Thermal and plastic behavior of nanoglasses, *J. Mater. Res.* 29 (2014) 1210–1216. doi:10.1557/jmr.2014.101.
- [36] J.Q. Wang, N. Chen, P. Liu, Z. Wang, D. V. Louzguine-Luzgin, M.W. Chen, J.H. Perepezko, The ultrastable kinetic behavior of an Au-based nanoglass, *Acta Mater.* 79 (2014) 30–36. doi:10.1016/j.actamat.2014.07.015.
- [37] O. Adjaoud, K. Albe, Interfaces and interphases in nanoglasses: Surface segregation effects and their implications on structural properties, *Acta Mater.* 113 (2016) 284–292. doi:10.1016/j.actamat.2016.05.002.
- [38] C. Wang, D. Wang, X. Mu, S. Goel, T. Feng, Y. Ivanisenko, H. Hahn, H. Gleiter, Surface segregation of primary glassy nanoparticles of Fe₉₀Sc₁₀ nanoglass, *Mater. Lett.* 181 (2016) 248–252. doi:10.1016/j.matlet.2016.05.189.
- [39] D. Şopu, Y. Ritter, H. Gleiter, K. Albe, Deformation behavior of bulk and nanostructured metallic glasses studied via molecular dynamics simulations, *Phys. Rev. B - Condens. Matter Mater. Phys.* 83 (2011) 1–4. doi:10.1103/PhysRevB.83.100202.
- [40] D. Şopu, J. Kotakoski, K. Albe, Finite-size effects in the phonon density of states of nanostructured germanium: A comparative study of nanoparticles, nanocrystals, nanoglasses, and bulk phases, *Phys. Rev. B - Condens. Matter Mater. Phys.* 83 (2011) 1–8. doi:10.1103/PhysRevB.83.245416.
- [41] K. Albe, Y. Ritter, D. Şopu, Enhancing the plasticity of metallic glasses: Shear band formation, nanocomposites and nanoglasses investigated by molecular dynamics simulations, *Mech. Mater.* 67 (2013) 94–103. doi:10.1016/j.mechmat.2013.06.004.
- [42] Y. Ritter, D. Opu, H. Gleiter, K. Albe, Structure, stability and mechanical properties of internal interfaces in Cu₆₄Zr₃₆ nanoglasses studied by MD simulations, *Acta Mater.* 59 (2011) 6588–6593. doi:10.1016/j.actamat.2011.07.013.
- [43] J.X. Fang, U. Vainio, W. Puff, R. Würschum, X.L. Wang, D. Wang, M. Ghafari, F. Jiang, J. Sun, H. Hahn, H. Gleiter, Atomic Structure and Structural Stability of Sc₇₅Fe₂₅ Nanoglasses, *Nano Lett.* 12 (2012) 458–463. doi:10.1021/nl2038216.
- [44] J. H. H. Liebermann and C. D. Graham, Production of amorphous alloy ribbons and effects of apparatus parameters on ribbon dimensions, *IEEE Trans. Magn.* 12 (1976) 921–923.
- [45] Y. Ma, Q.P. Cao, S.X. Qu, D.X. Zhang, X.D. Wang, J.Z. Jiang, Stress-state-dependent deformation behavior in Ni-Nb metallic glassy film, *Acta Mater.* 60 (2012) 4136–4143. doi:10.1016/j.actamat.2012.04.028.
- [46] M. Chen, A brief overview of bulk metallic glasses, *NPG Asia Mater.* 3 (2011) 82–90. doi:10.1038/asiamat.2011.30.
-

-
- [47] A.J. Drehman, A.L. Greer, D. Turnbull, Bulk formation of a metallic glass: Pd₄₀Ni₄₀P₂₀, *Appl. Phys. Lett.* 41 (1982) 716. doi:10.1063/1.93645.
- [48] H.S. Chen, Thermodynamic Considerations on the Formation and Stability of Metallic Glasses, *Acta Metall.* 22 (1974) 1505–1511.
- [49] A. Peker, W.L. Johnson, A highly processable metallic glass: Zr_{41.2}Ti_{13.8}Cu_{12.5}Ni_{10.0}Be_{22.5}, *Appl. Phys. Lett.* 63 (1993) 2342–2344. doi:10.1063/1.110520.
- [50] Preparation and thermal stability of bulk amorphous Pd₄₀Cu₃₀Ni₁₀P₂₀ alloy cylinder of 72 mm in diameter, *Mater. Trans. JIM.* 38 (1997) 179–183.
- [51] T. Fukushige, S. Hata, A. Shimokohbe, A MEMS conical spring actuator array, *J. Microelectromechanical Syst.* 14 (2005) 243–253. doi:10.1109/JMEMS.2004.839345.
- [52] N. Nishiyama, K. Amiya, A. Inoue, Recent progress of bulk metallic glasses for strain-sensing devices, *Mater. Sci. Eng. A.* 448–451 (2007) 79–83. doi:10.1016/j.msea.2006.02.384.
- [53] W. Kauzmann, The Nature Of The Glassy State And The Behaviour Of Liquids At Low Temperatures, *Chem. Rev.* 43 (1948) 219–256.
- [54] H. Bin Yu, Y. Luo, K. Samwer, Ultrastable metallic glass, *Adv. Mater.* 25 (2013) 5904–5908. doi:10.1002/adma.201302700.
- [55] S.F. Swallen, K.L. Kearns, M.K. Mapes, Y.S. Kim, R.J. McMahon, M.D. Ediger, T. Wu, L. Yu, S. Satija, Thermodynamic and Kinetic Stability, *Science* (80-.). 315 (2007) 353–357.
- [56] K.L. Kearns, S.F. Swallen, M.D. Ediger, T. Wu, L. Yu, Influence of substrate temperature on the stability of glasses prepared by vapor deposition, *J. Chem. Phys.* 127 (2007). doi:10.1063/1.2789438.
- [57] D. Turnbull, Under what conditions can a glass be formed?, *Contemp. Phys.* 10 (1969) 473–488. doi:10.1080/00107516908204405.
- [58] C.A. Angell, Formation of Glasses from Liquids and Biopolymers, *Science* (80-.). 267 (1995) 1924–1935. doi:10.1126/science.267.5206.1924.
- [59] R. Busch, Y.J. Kim, W.L. Johnson, W.M.K. Luboratory, Thermodynamics and kinetics of the undercooled alloy, 77 (1995) 4039–4043.
- [60] Y.Q. Cheng, E. Ma, Atomic-level structure and structure-property relationship in metallic glasses, *Prog. Mater. Sci.* 56 (2011) 379–473. doi:10.1016/j.pmatsci.2010.12.002.
- [61] J.D. Bernal, Geometry of the structure of monoatomic liquids, *Nature.* 185 (1960) 68–70.
- [62] P.H. Gaskell, A new structural model for transition metal–metalloid glasses, *Nature.* 276 (1978) 484–485. doi:10.1038/276484a0.
- [63] D.B. Miracle, A structural model for metallic glasses, *Nat. Mater.* 3 (2004) 697–702. doi:10.1038/nmat1219.
- [64] D.B. Miracle, The density and packing fraction of binary metallic glasses, *Acta Mater.* 61 (2013) 3157–3171. doi:10.1016/j.actamat.2013.02.005.
- [65] H.W. Sheng, W.K. Luo, F.M. Alamgir, J.M. Bai, E. Ma, Atomic packing and short-to-medium-range order in metallic glasses, *Nature.* 439 (2006) 419–425.

- doi:10.1038/nature04421.
- [66] A. Hirata, P. Guan, T. Fujita, Y. Hirotsu, A. Inoue, A.R. Yavari, T. Sakurai, M. Chen, Direct observation of local atomic order in a metallic glass, *Nat. Mater.* 10 (2011) 28–33. doi:10.1038/nmat2897.
- [67] A. Hirata, L.J. Kang, T. Fujita, B. Klumov, K. Matsue, M. Kotani, A.R. Yavari, M.W. Chen, Geometric Frustration of Icosahedron in Metallic Glasses, *Science* (80-.). 341 (2013) 376–379. doi:10.1126/science.1232450.
- [68] A.S. Argon, H.Y. Kuo, Plastic flow in a disordered bubble raft (an analog of a metallic glass), *Mater. Sci. Eng.* 39 (1979) 101–109. doi:10.1016/0025-5416(79)90174-5.
- [69] T.C. Hufnagel, C.A. Schuh, M.L. Falk, Deformation of metallic glasses: Recent developments in theory, simulations, and experiments, *Acta Mater.* 109 (2016) 375–393. doi:10.1016/j.actamat.2016.01.049.
- [70] A.L. Greer, Y.Q. Cheng, E. Ma, Shear bands in metallic glasses, *Mater. Sci. Eng. R Reports.* 74 (2013) 71–132. doi:10.1016/j.mser.2013.04.001.
- [71] Z.T. Wang, J. Pan, Y. Li, C.A. Schuh, Densification and strain hardening of a metallic glass under tension at room temperature, *Phys. Rev. Lett.* 111 (2013). doi:10.1103/PhysRevLett.111.135504.
- [72] G. Knuyt, L. Deschepper, L.M. Stals, Calculation of Elastic-Constants for An Amorphous Metal and the Influence of Relaxation, *J. Phys. F-Metal Phys.* 16 (1986) 1989–2006. doi:10.1088/0305-4608/16/12/011.
- [73] Y. Kawamura, T. Nakamura, A. Inoue, Superplasticity in Pd₄₀Ni₄₀P₂₀ metallic glass, *Scr. Mater.* 39 (1998) 301–306. doi:10.1016/S1359-6462.
- [74] H. Zheng, Y. Li, Cooperative shear and catastrophic fracture of bulk metallic glasses from a shear-band instability perspective, *J. Mater. Res.* 24 (2009) 3620–3627. doi:10.1557/jmr.2009.0442.
- [75] D. Şopu, A. Stukowski, M. Stoica, S. Scudino, Atomic-Level Processes of Shear Band Nucleation in Metallic Glasses, *Phys. Rev. Lett.* 119 (2017) 1–5. doi:10.1103/PhysRevLett.119.195503.
- [76] F. Spaepen, A microscopic mechanism for steady state inhomogeneous flow in metallic glasses, *Acta Metall.* 25 (1977) 407–415. doi:https://doi.org/10.1016/0001-6160(77)90232-2.
- [77] Q. An, K. Samwer, M.D. Demetriou, M.C. Floyd, D.O. Duggins, W.L. Johnson, W.A. Goddard, How the toughness in metallic glasses depends on topological and chemical heterogeneity, *Proc. Natl. Acad. Sci.* 113 (2016) 7053–7058. doi:10.1073/pnas.1607506113.
- [78] Y. Ritter, K. Albe, Chemical and topological order in shear bands of Cu₆₄Zr₃₆ and Cu₃₆Zr₆₄ glasses, *J. Appl. Phys.* 111 (2012) 103527. doi:10.1063/1.4717748.
- [79] C.C. Hays, C.P. Kim, W.L. Johnson, Microstructure controlled shear band pattern formation and enhanced plasticity of bulk metallic glasses containing in situ formed ductile phase dendrite dispersions, *Phys. Rev. Lett.* 84 (2000) 2901–2904. doi:10.1103/PhysRevLett.84.2901.
- [80] Y.Q. Cheng, A.J. Cao, E. Ma, Correlation between the elastic modulus and the intrinsic plastic behavior of metallic glasses: The roles of atomic configuration and alloy composition, *Acta Mater.* 57 (2009) 3253–3267.

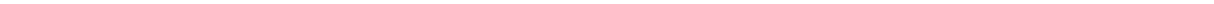
- doi:10.1016/j.actamat.2009.03.027.
- [81] J.J. Lewandowski, W.H. Wang, A.L. Greer, Intrinsic plasticity or brittleness of metallic glasses, *Philos. Mag. Lett.* 85 (2005) 77–87. doi:10.1080/09500830500080474.
- [82] H. Guo, P.F. Yan, Y.B. Wang, J. Tan, Z.F. Zhang, M.L. Sui, E. Ma, Tensile ductility and necking of metallic glass, *Nat. Mater.* 6 (2007) 735–739. doi:10.1038/nmat1984.
- [83] H. Gleiter, Nanoglasses: A Way to Solid Materials with Tunable Atomic Structures and Properties, *Mater. Sci. Forum.* 584–586 (2008) 41–48. doi:10.4028/www.scientific.net/MSF.584-586.41.
- [84] H. Gleiter, Our thoughts are ours, their ends none of our own: Are there ways to synthesize materials beyond the limitations of today?, *Acta Mater.* 56 (2008) 5875–5893. doi:10.1016/j.actamat.2008.08.028.
- [85] J. Weissmüller, R. Birringer, H. Gleiter, Nanostructured Crystalline and Amorphous Solids, *Key Eng. Mater.* 77–78 (1992) 161–170. doi:10.4028/www.scientific.net/KEM.77-78.161.
- [86] C. Wang, X. Guo, Y. Ivanisenko, S. Goel, H. Nirschl, H. Gleiter, H. Hahn, Atomic structure of Fe₉₀Sc₁₀ glassy nanoparticles and nanoglasses, *Scr. Mater.* 139 (2017) 9–12. doi:10.1016/j.scriptamat.2017.06.007.
- [87] O. Adjaoud, K. Albe, Microstructure formation of metallic nanoglasses: Insights from molecular dynamics simulations, *Acta Mater.* 145 (2017) 322–330. doi:10.1016/j.actamat.2017.12.014.
- [88] D. Danilov, H. Hahn, H. Gleiter, W. Wenzel, Mechanisms of Nanoglass Ultrastability, *ACS Nano.* 10 (2016) 3241–3247. doi:10.1021/acs.nano.5b05897.
- [89] A.G. Dirks, H.J. Leamy, Columnar microstructure in vapor-deposited thin films, *Thin Solid Films.* 47 (1977) 219–233. doi:10.1016/0040-6090(77)90037-2.
- [90] N. Chen, X. Shi, R. Witte, K.S. Nakayama, K. Ohmura, H. Wu, A. Takeuchi, H. Hahn, M. Esashi, H. Gleiter, A. Inoue, D. V. Louzguine, A novel Ti-based nanoglass composite with submicron–nanometer-sized hierarchical structures to modulate osteoblast behaviors, *J. Mater. Chem. B.* 1 (2013) 2568. doi:10.1039/c3tb20153h.
- [91] D. Şopu, K. Albe, Y. Ritter, H. Gleiter, From nanoglasses to bulk massive glasses, *Appl. Phys. Lett.* 94 (2009) 2009–2011. doi:10.1063/1.3130209.
- [92] S. Adibi, P.S. Branicio, Y.-W. Zhang, S.P. Joshi, Composition and grain size effects on the structural and mechanical properties of CuZr nanoglasses, *J. Appl. Phys.* 116 (2014) 43522. doi:10.1063/1.4891450.
- [93] S. Adibi, Z.D. Sha, P.S. Branicio, S.P. Joshi, Z.S. Liu, Y.W. Zhang, A transition from localized shear banding to homogeneous superplastic flow in nanoglass, *Appl. Phys. Lett.* 103 (2013) 1–6. doi:10.1063/1.4833018.
- [94] S. Adibi, P.S. Branicio, S.P. Joshi, Suppression of Shear Banding and Transition to Necking and Homogeneous Flow in Nanoglass Nanopillars., *Sci. Rep.* 5 (2015) 15611. doi:10.1038/srep15611.
- [95] C. Suryanarayana, B. Prabhu, Synthesis of Nanostructured Materials by Inert-Gas Condensation Methods, Chapter 2, in: Koch, Carl C. *Nanostructured Mater. Process. Prop. Appl.* 2nd Ed., 2007: pp. 47–90. doi:http://dx.doi.org/10.1016/B978-081551534-0.50004-X.

-
- [96] H. Hahn, R.S. Averback, The production of nanocrystalline powders by magnetron sputtering, *J. Appl. Phys.* 67 (1990) 1113–1115. doi:10.1063/1.345798.
- [97] P.J.J. Kelly, R.D. Arnell, Magnetron sputtering: a review of recent developments and applications, *Vacuum*. 56 (2000) 159–172. doi:10.1016/S0042-207X(99)00189-X.
- [98] T.F. Kelly, M.K. Miller, Atom probe tomography, *Rev. Sci. Instrum.* 78 (2007). doi:10.1063/1.2709758.
- [99] D.J. Larson, T.J. Prosa, R.M. Ulfig, B.P. Geiser, T.F. Kelly, *Local electrode atom probe tomography*, 1st ed., Springer, New York, NY, 2013. doi:https://doi.org/10.1007/978-1-4614-8721-0.
- [100] K. Thompson, D. Lawrence, D.J. Larson, J.D. Olson, T.F. Kelly, B. Gorman, In situ site-specific specimen preparation for atom probe tomography, *Ultramicroscopy*. 107 (2007) 131–139. doi:10.1016/j.ultramic.2006.06.008.
- [101] A. Kilmametov, R. Gröger, H. Hahn, T. Schimmel, S. Walheim, Bulk Density Measurements of Small Solid Objects Using Laser Confocal Microscopy, *Adv. Mater. Technol.* (2016) 1600115. doi:10.1002/admt.201600115.
- [102] L.A. Giannuzzi, F.A. Stevie, A review of focused ion beam milling techniques for TEM specimen preparation, *Micron*. 30 (1999) 197–204. doi:10.1016/S0968-4328(99)00005-0.
- [103] W. Gruner, Determination of oxygen in oxides by carrier gas hot extraction analysis with simultaneous CO_x detection, *Fresenius. J. Anal. Chem.* 365 (1999) 597–603. doi:10.1007/s002160051529.
- [104] G.E. Dieter, *Mechanical metallurgy*, 2nd ed., McGraw Hill Book Company, Inc, New York, USA, 1961.
- [105] W.C. Oliver, G.M. Pharr, An improved technique for determining hardness and elastic modulus using load and displacement sensing indentation experiments, *J. Mater. Res.* 7 (1992) 1564–1583. doi:https://doi.org/10.1557/JMR.1992.1564.
- [106] W.C. Oliver, G.M. Pharr, Measurement of hardness and elastic modulus by instrumented indentation: Advances in understanding and refinements to methodology, *J. Mater. Res.* 19 (2004) 3–20. doi:10.1557/jmr.2004.19.1.3.
- [107] B.N. Lucas, W.C. Oliver, Indentation power-law creep of high-purity indium, *Metall. Mater. Trans. A*. 30 (1999) 601–610. doi:10.1007/s11661-999-0051-7.
- [108] I.N. Sneddon, The relation between load and penetration in the axisymmetric boussinesq problem for a punch of arbitrary profile, *Int. J. Eng. Sci.* 3 (1965) 47–57. doi:10.1016/0020-7225(65)90019-4.
- [109] C.A. Volkert, E.T. Lilleodden, Size effects in the deformation of sub-micron Au columns, *Philos. Mag.* 86 (2006) 5567–5579. doi:10.1080/14786430600567739.
- [110] J.R. Greer, J.T.M. De Hosson, Plasticity in small-sized metallic systems: Intrinsic versus extrinsic size effect, *Prog. Mater. Sci.* 56 (2011) 654–724. doi:10.1016/j.pmatsci.2011.01.005.
- [111] S. Plimpton, Fast parallel algorithms for short-range molecular dynamics, *J. Comput. Phys.* 117 (1995) 1–19. doi:10.1006/jcph.1995.1039.
- [112] J. Ding, Y.Q. Cheng, H. Sheng, E. Ma, Short-range structural signature of excess specific heat and fragility of metallic-glass-forming supercooled liquids, *Phys. Rev. B - Condens. Matter Mater. Phys.* 85 (2012) 1–5. doi:10.1103/PhysRevB.85.060201.

-
- [113] Y.Q. Cheng, J. Ding, E. Ma, Local Topology vs. atomic-level stresses as a measure of disorder: Correlating structural indicators for metallic glasses, *Mater. Res. Lett.* 1 (2013) 3–12. doi:10.1080/21663831.2012.722759.
- [114] Y.C. Hu, F.X. Li, M.Z. Li, H.Y. Bai, W.H. Wang, Five-fold symmetry as indicator of dynamic arrest in metallic glass-forming liquids, *Nat. Commun.* 6 (2015) 6–13. doi:10.1038/ncomms9310.
- [115] D. Wang, Y. Li, B.B. Sun, M.L. Sui, K. Lu, E. Ma, Bulk metallic glass formation in the binary Cu-Zr system, *Appl. Phys. Lett.* 84 (2004) 4029–4031. doi:10.1063/1.1751219.
- [116] K.W. Park, J. il Jang, M. Wakeda, Y. Shibutani, J.C. Lee, Atomic packing density and its influence on the properties of Cu-Zr amorphous alloys, *Scr. Mater.* 57 (2007) 805–808. doi:10.1016/j.scriptamat.2007.07.019.
- [117] M.B. Tang, D.Q. Zhao, M.X. Pan, W.H. Wang, Binary Cu–Zr Bulk Metallic Glasses, *Chin. Phys. Lett.* 21 (2004) 901–903. doi:https://doi.org/10.1088/0256-307X/21/5/039.
- [118] D. Xu, B. Lohwongwatana, G. Duan, W.L. Johnson, C. Garland, Bulk metallic glass formation in binary Cu-rich alloy series - Cu_{100-x}Zr_x (x=34 , 36, 38.2, 40 at.%) and mechanical properties of bulk Cu₆₄Zr₃₆ glass, *Acta Mater.* 52 (2004) 2621–2624. doi:10.1016/j.actamat.2004.02.009.
- [119] K.F. Yao, N. Chen, Pd-Si binary bulk metallic glass, *Sci. China, Ser. G Physics, Mech. Astron.* 51 (2008) 414–420. doi:10.1007/s11433-008-0051-4.
- [120] Y. Ke-fu, R. Fang, Pd-Si binary bulk metallic glass prepared at low cooling rate, *Chin. Phys. Lett.* 22 (2005) 1481.
- [121] K.F. Yao, F. Ruan, Y.Q. Yang, N. Chen, Superductile bulk metallic glass, *Appl. Phys. Lett.* 88 (2006) 4–7. doi:10.1063/1.2187516.
- [122] N. Mattern, A. Schöps, U. Kühn, J. Acker, O. Khvostikova, J. Eckert, Structural behavior of Cu_xZr_{100-x} metallic glass (x = 35-70), *J. Non. Cryst. Solids.* 354 (2008) 1054–1060. doi:10.1016/j.jnoncrysol.2007.08.035.
- [123] H.S. Chen, D. Turnbull, Structure of Pd-Si based alloy glasses, *Acta Metall.* 17 (1969) 1021–1031.
- [124] S.H. Nandam, Y. Ivanisenko, R. Schwaiger, Z. Śniadecki, X. Mu, D. Wang, R. Chellali, T. Boll, A. Kilmametov, T. Bergfeldt, H. Gleiter, H. Hahn, Cu-Zr nanoglasses: Atomic structure, thermal stability and indentation properties, *Acta Mater.* 136 (2017) 181–189. doi:10.1016/j.actamat.2017.07.001.
- [125] T. Cullinan, I. Kalay, Y.E. Kalay, M. Kramer, R. Napolitano, Kinetics and Mechanisms of Isothermal Devitrification in Amorphous Cu₅₀Zr₅₀, *Metall. Mater. Trans. A Phys. Metall. Mater. Sci.* 46 (2015) 600–613. doi:10.1007/s11661-014-2661-y.
- [126] I. Kalay, M.J. Kramer, R.E. Napolitano, High-accuracy X-ray diffraction analysis of phase evolution sequence during devitrification of Cu₅₀Zr₅₀ metallic glass, *Metall. Mater. Trans. A Phys. Metall. Mater. Sci.* 42 (2011) 1144–1153. doi:10.1007/s11661-010-0531-9.
- [127] S. Pauly, Phase formation and mechanical properties of metastable Cu-Zr-based alloys, TU Dresden, 2010. [http://www.qucosa.de/recherche/frontdoor/cache.off?tx_slubopus4frontend\[id\]=3954](http://www.qucosa.de/recherche/frontdoor/cache.off?tx_slubopus4frontend[id]=3954).
-

-
- [128] H.E. Kissinger, Reaction Kinetics in Differential Thermal Analysis, *Anal. Chem.* 29 (1957) 1702–1706. doi:10.1021/ac60131a045.
- [129] S. Pauly, J. Das, N. Mattern, D.H. Kim, J. Eckert, Phase formation and thermal stability in Cu-Zr-Ti(Al) metallic glasses, *Intermetallics*. 17 (2009) 453–462. doi:10.1016/j.intermet.2008.12.003.
- [130] B.S. Murty, D.H. Ping, K. Hono, A. Inoue, Influence of oxygen on the crystallization behavior of $Zr_{65}Cu_{27.5}Al_{7.5}$ and $Zr_{66.7}Cu_{33.3}$ metallic glasses, *Acta Mater.* 48 (2000) 3985–3996. doi:http://dx.doi.org/10.1016/S1359-6454(00)00190-7.
- [131] D. Pan, A. Inoue, T. Sakurai, M.W. Chen, Experimental characterization of shear transformation zones for plastic flow of bulk metallic glasses, *Proc. Natl. Acad. Sci. U. S. A.* 105 (2008) 14769–14772. doi:10.1073/pnas.0806051105.
- [132] W.L. Johnson, K. Samwer, A universal criterion for plastic yielding of metallic glasses with a $(T/T_g)^{2/3}$ temperature dependence, *Phys. Rev. Lett.* 95 (2005) 2–5. doi:10.1103/PhysRevLett.95.195501.
- [133] J.P. Chevalier, Y. Calvayrac, A. Quivy, M. Harmelin, J. Bigot, Crystallization in oxygen doped amorphous $Cu_{50}Zr_{50}$: A metallic glass-ceramic?, *Acta Metall.* 31 (1982) 465–471.
- [134] J. Zhao, E. Baibuz, J. Vernieres, P. Grammatikopoulos, V. Jansson, M. Nagel, S. Steinhauer, M. Sowwan, A. Kuronen, K. Nordlund, F. Djurabekova, Formation Mechanism of Fe Nanocubes by Magnetron Sputtering Inert Gas Condensation, *ACS Nano*. 10 (2016) 4684–4694. doi:10.1021/acsnano.6b01024.
- [135] F.O. Mear, B. Doisneau, A.R. Yavari, A.L. Greer, Structural effects of shot-peening in bulk metallic glasses, *J. Alloys Compd.* 483 (2009) 256–259. doi:10.1016/j.jallcom.2007.12.105.
- [136] G. Wilde, H. Rösner, Nanocrystallization in a shear band: An in situ investigation, *Appl. Phys. Lett.* 98 (2011) 9–12. doi:10.1063/1.3602315.
- [137] O.J. Kwon, Y.C. Kim, K.B. Kim, Y.K. Lee, E. Fleury, Formation of amorphous phase in the binary Cu–Zr alloy system, *Met. Mater. Int.* 12 (2006) 207–212. doi:10.1007/BF03027532.
- [138] M. Chen, A. Inoue, W. Zhang, T. Sakurai, Extraordinary plasticity of ductile bulk metallic glasses, *Phys. Rev. Lett.* 96 (2006) 1–4. doi:10.1103/PhysRevLett.96.245502.
- [139] A. Inoue, W. Zhang, T. Tsurui, A.R. Yavari, A.L. Greer, Unusual room-temperature compressive plasticity in nanocrystal-toughened bulk copper-zirconium glass, *Philos. Mag. Lett.* 85 (2005) 221–229. doi:10.1080/09500830500197724.
- [140] D.Z. Chen, Q. An, W.A. Goddard, J.R. Greer, Ordering and dimensional crossovers in metallic glasses and liquids, *Phys. Rev. B.* 95 (2017) 1–8. doi:10.1103/PhysRevB.95.024103.
- [141] X. Wang, M. Zeng, N. Nollmann, G. Wilde, Z. Tian, C. Tang, Effect of copper addition on the glass forming ability in Pd-Si binary amorphous alloying system, *AIP Adv.* 7 (2017) 1–7. doi:10.1063/1.4986532.
- [142] Y. Ivanisenko, C. Kubel, S.H. Nandam, C. Wang, X. Mu, O. Adjaoud, K. Albe, H. Hahn, Structure and properties of nanoglasses, *Adv. Eng. Mater.* (n.d.).
- [143] H.S. Chen, T.T. Wang, Mechanical Properties of Metallic Glasses of Pd-Si Based Alloys, *J. Appl. Phys.* 41 (1970) 5338. doi:10.1063/1.1658675.
-

-
- [144] C.A. Volkert, A. Donohue, F. Spaepen, Effect of sample size on deformation in amorphous metals, *J. Appl. Phys.* 103 (2008) 1–6. doi:10.1063/1.2884584.
- [145] A. Stukowski, Visualization and analysis of atomistic simulation data with OVITO-the Open Visualization Tool, *Model. Simul. Mater. Sci. Eng.* 18 (2010). doi:10.1088/0965-0393/18/1/015012.
- [146] A. Barranco, A. Borrás, A.R. González-Elipé, A. Palmero, Perspectives on oblique angle deposition of thin films: From fundamentals to devices, *Prog. Mater. Sci.* 76 (2016) 59–153. doi:10.1016/j.pmatsci.2015.06.003.
- [147] N. Chen, D. V. Louzguine-Luzgin, G.Q. Xie, P. Sharma, J.H. Perepezko, M. Esashi, A.R. Yavari, A. Inoue, Structural investigation and mechanical properties of a representative of a new class of materials: Nanograined metallic glasses, *Nanotechnology*. 24 (2013) 45610. doi:10.1088/0957-4484/24/4/045610.
- [148] D. Tönnies, R. Maaß, C.A. Volkert, Room temperature homogeneous ductility of micrometer-sized metallic glass, *Adv. Mater.* 26 (2014) 5715–5721. doi:10.1002/adma.201401123.
- [149] M.R. Chellali, S.H. Nandam, S. Li, M.H. Fawey, E. Moreno-Pineda, L. Velasco, T. Boll, L. Pastewka, R. Kruk, P. Gumbsch, H. Hahn, Draft_NiTi_Chellali, (n.d.).
- [150] N. Chen, D. Wang, T. Feng, R. Kruk, K.-F. Yao, D. V. Louzguine-Luzgin, H. Hahn, H. Gleiter, A nanoglass alloying immiscible Fe and Cu at the nanoscale, *Nanoscale*. 7 (2015) 6607–6611. doi:10.1039/C5NR01406A.



Curriculum Vitae

Name: Sree Harsha Nandam
Date of Birth: 11.01.1987
Place of Birth: Hyderabad, India
Nationality: Indian

Education:

May 2013 – present Doctoral studies in Material science
Joint Research Laboratory for Nanomaterials,
Technische Universität Darmstadt and Karlsruhe
Institute of Technology, Germany

March 2010 – June 2012 Master of Science (by Research)
Department of Metallurgical and Materials Engineering,
Indian Institute of Technology Madras, Chennai, India

August 2005 – May 2009 Bachelor of Technology
Department of Metallurgical and Materials Engineering,
Indian Institute of Technology Madras, Chennai, India

Professional Experience:

August 2009 – February 2010
July 2012 – March 2013 Project Associate
in the group of Prof. Sankaran and Prof. B.S. Murty
Department of Metallurgical and Materials Engineering,
Indian Institute of Technology Madras, Chennai, India

List of Publications

Publications relevant to the thesis:

1. Cu-Zr nanoglasses: Atomic structure, thermal stability and indentation properties
S.H. Nandam, Y. Ivanisenko, R. Schwaiger, Z. Sniadecki, X. Mu, D. Wang, R. Chellali, T. Boll, A. Kilmametov, T. Bergfeldt, H. Gleiter and H. Hahn, *Acta Materialia*, 136 (2017) 181-189.
2. Influence of topological structure on the mechanical properties of Pd-Si nanoglasses
S.H. Nandam, O. Adjaoud, R. Schwaiger, Y. Ivanisenko, R. Chellali, D. Wang, K. Albe and H. Hahn (to be submitted)
3. High strength and plastic Cu-Zr nanoglasses: An experimental and atomistic study
S.H. Nandam, R. Schwaiger, Y. Ivanisenko, O. Adjaoud, K. Albe and H. Hahn (under preparation)

Other publications

4. Amorphous Ni nanophases inducing ferromagnetism in Ni₅₀Ti₅₀ nanoglass
M.R. Chellali, **S.H. Nandam**, S.Li, M.H. Fawey, E. Moreno-Pineda, L. Velasco, T. Boll, L. Pastewka, R. Kruk, P. Gumbsch and H. Hahn, *Acta Materialia*, 161 (2018) 47-53.
5. Y. Ivanisenko, C. Kubel, **S.H. Nandam**, C. Wang, X. Mu, O. Adjaoud, K. Albe, H. Hahn, Structure and properties of nanoglasses, *Advanced Engineering Materials* (in print).
6. Z. Zhang, E. Odor, D. Farkas, B. Joni, G. Ribarik, G. Tichy, **S.H. Nandam**, Y. Ivanisenko, M. Preuss and T. Ungar, Lattice dislocations in grain boundaries – the origin of heterogeneous strains in nanocrystalline materials, submitted to *Acta Materialia* (under review)
7. M.R.Chellali, A.Sarkar, **S.H. Nandam**, B. Breitung, L. Velasco and H. Hahn, On the homogeneity of high entropy oxides: An investigation at the atomic scale, (to be submitted)
8. Deformation behaviour of in-situ TiB₂ reinforced A357 aluminum alloy composite foams under compressive and impact loading
U.A. Atturan, **S.H. Nandam**, B.S. Murty and S. Sankaran, *Materials Science and Engineering A*, 684 (2017) 178-185.
9. Processing and characterization of in-situ stabilized closed cell aluminum alloy composite foams
U.A. Atturan, **S.H. Nandam**, B.S. Murty and S. Sankaran, *Materials and Design*, 101 (2016) 245-253.

10. Influence of TiB_2 addition on the precipitation kinetics in Al-7Si-0.3Mg in-situ TiB_2 composites

S.H. Nandam, B.S. Murty and S. Sankaran, Metallurgical and Materials Transactions A, 46 (2015) 2844-2849.

11. Microstructural and Mechanical characterization of two aluminum based in-situ composite foams

S.H. Nandam, N. Charbhai, B.S. Murty and S. Sankaran, Transactions of the Indian Institute of Metals, 65 (2012) 595-600.

12. Precipitation kinetics in Al-Si-Mg/ TiB_2 in-situ composites

S.H. Nandam, S. Sankaran and B.S. Murty, Transactions of the Indian Institute of Metals, 64 (2011) 123-126.

Acknowledgements

I would like to thank many people who have contributed to the successful completion of my doctoral thesis.

First of all, I am grateful to Prof. Hahn for his constant support and guidance throughout the project, which helped me to understand many things about IGC and other related problems. It was his idea to install the sputtering unit in IGC, which was a significant step in my dissertation.

I thank Dr. Julia Ivanisenko for all the help she offered me in these five years, especially all the discussions on the work, correction of the manuscripts and all the tedious jobs like ordering chemicals.

I am also indebted to Dr. Thomas Reisinger for all the help he offered me during the installation of the sputtering unit. Almost all the knowledge I gained on UHV systems has been from him, which is invaluable to me now and later on in my career. Most importantly, I am glad that he is such a wonderful office mate all these years.

A great deal of help has also come from Dr. Chaomin Wang who taught me the IGC machine initially and also for the discussions about nanoglasses in the initial stages of my dissertation.

I am also thankful to Martin Limbach, our technician who has spent a considerable amount of time repairing the machine at various stages in these five years.

I should thank Dr. Shiv Prakash Singh for his company in the IGC lab and also for providing his help during experiments in the past couple of years.

I am grateful to my collaborators in Darmstadt: Prof. Karsten Albe and Dr. Omar Adjaoud for all the stimulating discussions and for performing the MD simulations. I am also indebted to Prof. Herbert Gleiter for all the insightful discussions over these years.

I am thankful to all my other collaborators: Dr. Ruth Schwaiger for all the micro mechanical tests, Dr. Reda Chellali and Dr. Torben Boll for the APT measurements, Dr. Zbigniew Sniadecki for giving access to the DSC equipment, Dr. Di Wang and Dr. Xiaoke Mu for their support with TEM.

I also express my gratitude to the entire Hahn group, past and present, who helped me directly and indirectly for the successful completion of my dissertation.

I am grateful for all the support and encouragement given by my friends during all these years.

I acknowledge the financial assistance provided by DFG/SPP 1594 program under the grant HA 1344/30-1.

Finally, I acknowledge my sister, Sravanthi, for all the phone calls (and all the stupid jokes) which definitely helped me during some of the difficult periods of my stay. I must also thank my sister's family for their support in all these years. Ultimately, I am grateful to my parents, Jayasree and Hanumantha Rao, for putting up with me through all the good and bad moments.